WARMING UP

Innovatief Duurzaam Warmtecollectief

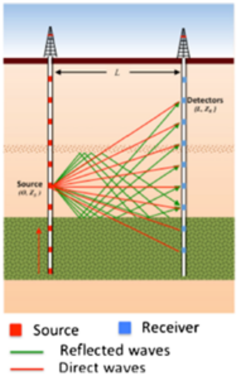

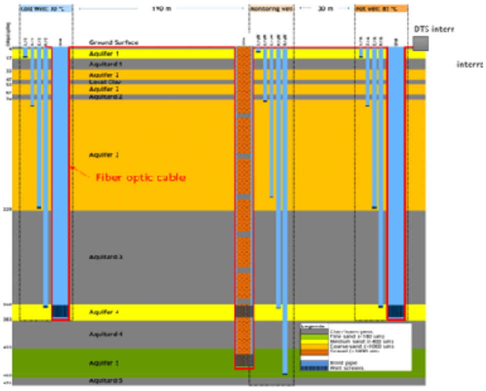

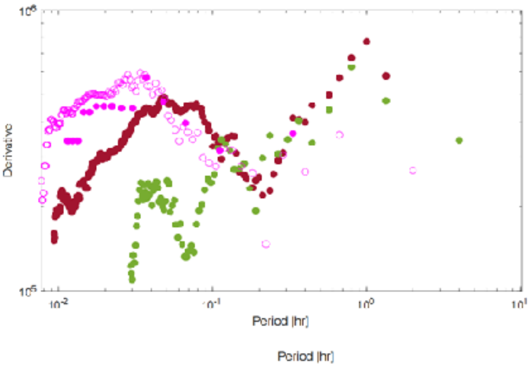

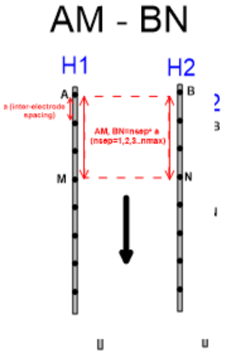

Monitoring techniques

For High Temperature storage

door

Marios Karaoulis, Edwin Obando Hernandez, Johan Valstar, Stefan Carpentier, Boris Boullenger, Dorien Dinkelman en Mariëlle Koenen

9 augustus 2023

Monitoring techniques

Marios Karaoulis, Edwin Obando Hernandez, Johan Valstar, Stefan Carpentier, Boris Boullenger, Dorien Dinkelman en Mariëlle Koenen
9 augustus 2023

Dit project is uitgevoerd als onderdeel van het Innovatieplan WarmingUP. Dit is mede mogelijk gemaakt door subsidie van de Rijksdienst voor Ondernemend Nederland (RVO) in het kader van de subsidieregeling Meerjarige Missiegedreven Innovatie Programma's (MMIP), bij RVO bekend onder projectnummer TEUE819001.
WarmingUP geeft invulling aan MMIP-4 – Duurzame warmte en koude in gebouwde omgeving en levert daarmee een bijdrage aan Missie B – Een CO_2-vrije gebouwde omgeving in 2050.

Projectnummer
11205160

Keywords
Monitoring
HT-ATES
Hoge temperatuur opslag

Jaar van publicatie
2023

Meer informatie
Johan Valstar
T 06 46914608
E Johan.valstar@deltares.nl

Inhoudsopgave

1 Introduction

High Temperature Aquifer Thermal Energy Storage

The WarmingUP research program investigates the possibilities for High Temperature Aquifer Thermal Energy Storage (HT-ATES) in the Netherlands.

Heat will be stored in the subsurface when the heat supply is larger than the heat demand. Water from a warm well is abstracted and heated within a heat exchanger and injected in a hot well. When the heat demand is larger than the heat supply, additional heat is taken back from the subsurface: the hot water is abstracted from the hot well and part of its heat is exchanged to the heat network in the heat exchanger. The cooler, but still warm, water is injected in the subsurface in the warm well.

The efficiency of the subsurface storage depends on the return temperature of the abstracted hot water, which depends on the thermal evolution in the subsurface over time. The thermal evolution in the subsurface is affected by various processes, such as the abstraction and injection in the wells, heat convection, the uplifting of hot water due to difference in density (buoyancy) and heat loss to the overburden. The thermal evolution can be predicted by model calculations, but the prediction will deviate from reality due to incomplete knowledge about subsurface parameters and heterogeneity in the subsurface.

Monitoring of the thermal evolution in the subsurface is therefore necessary in order to improve our knowledge on the behavior and/or optimization of HT-ATES systems. The monitoring of the subsurface thermal evolution is the subject of this report. As it is expensive to drill additional wells for extensive monitoring, techniques are investigated that use a single test drilling and/or the production wells only.

Goal of monitoring

The monitoring of subsurface thermal evolution in an HT-ATES system can be applied for three different types of goals:

1. Model validation/ general research

For this goal, the monitoring is used to validate if the thermal evolution is comparable to its modelled prediction. If not, it can be analyzed which parameters should be different. For instance, if the uplifting of hot water due to density difference is underestimated, it is an indication that the vertical hydraulic conductivity of the storage aquifer in the model was too low. For future projects in the same aquifer this knowledge can be used for improving the model prediction and adapting the system design.

2. Operational management

For this goal, the monitoring data is used to adapt the operational strategy. For instance, if the thermal evolution in the subsurface combined with model prediction predict that the abstraction

temperature will become too low at the end of the winter season it may be a reason to start using different heat sources when they are available at favorable financial conditions.
Another example is the option to abstract more water at the upper part of the well screen of the hot well if the subsurface thermal evolution shows that the buoyancy effect would cause a strong temperature reduction at the bottom part of the well screen in the remaining part of the winter season.

3. Environmental impact assessment

Monitoring the heat loss from the reservoir upwards into the overburden and from the hot well laterally into overlying sediments identifies the extent of heating over time. This is important for drinking water protection and for defining the extent of chemical and microbial risks related to subsurface heating.

Set up of the document

In this report, chapter 2 – 5 give short descriptions of the individual monitoring technique as well as information about the spatial extension, resolution, accuracy, costs, limitation of the technique and potential future research. Chapter 2 describes the Electrical Resistivity Tomography (ERT); chapter 3 handles the Acoustic Tomography; chapter 4 gives an overview of the DTS monitoring combined with thermal model calibration and pulse testing is described in chapter 5. In Chapter 6, a comparison between the different monitoring techniques is described. Finally, conclusions and recommendations are given in chapter 7.
In the appendices, a more detailed description of the research is given for each of the monitoring techniques.

2 Electrical Resistivity Tomography

This chapter gives a short description of the technique and the modelling and laboratory results. In Appendix A an extensive description is given.

Short description of technique

The electrical resistivity tomography measures the electrical resistivity in the subsurface and is extensively used worldwide due to its relative ease for data collection and interpretation. Originally it was used from the land surface, but it is also applied in cross-well boreholes.
A typical acquisition system for DC (Direct Current) resistivity measurements comprises of a resistivity meter, an electric source (battery), cables with electrodes, a switching box and control and storage unit (computer). For each measurement, two current electrodes are used: one to inject the current into the subsurface and the other to retrieve the same amount of current from it. By convention, these electrodes are named A and B, respectively. The electric field is measured (at least) with two other electrodes (M and N) called the potential electrodes, see Figure 1 and Figure 2).

By varying the location of the electrodes, the properties of different parts of the subsurface are observed. Using switch boxes connected to a large number of electrodes allows for a large number of measurements to be taken in a short time, resulting in the capability for repeating measurements over longer time periods (time-lapse data).
To increase vertical resolution, electrodes can also be placed within boreholes, allowing higher resolution imaging between the boreholes. Boreholes can be placed in a 2D plane or distributed in 3D to get 3D tomographic images. Collecting data over time (time-lapse ERT), we can image the resistivity property in 4D dimensions. The electrical resistivity of the subsurface is dependent on the temperature. During heat injection and production the electrical resistivity changes and by monitoring these changes, the thermal evolution can be derived.

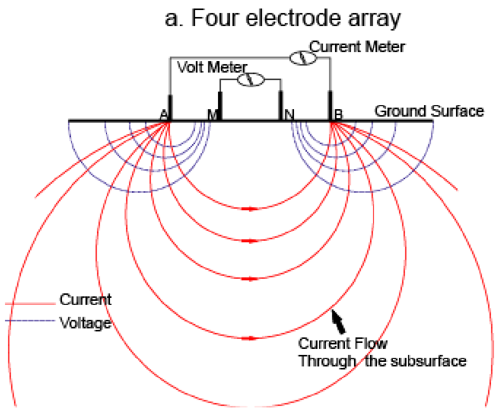

Figure 1: The principle of an ERT measurement from the land surface, showing the currents in a cross-section.

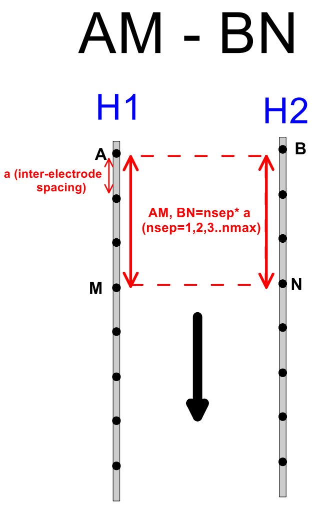

Figure 2 Example of a cross well ERT set up

The technique was tested in a synthetic model and a laboratory experiment. For the synthetic model a heat transport model was used to simulate a thermal evolution during heat injection with 90 °C in a slightly heterogeneous aquifer. At two different times, ERT measurements were simulated and used as the only data source to recover the thermal evolution. The real synthetic as well as the recovered resistivity distribution at one time step is shown in Figure 3.

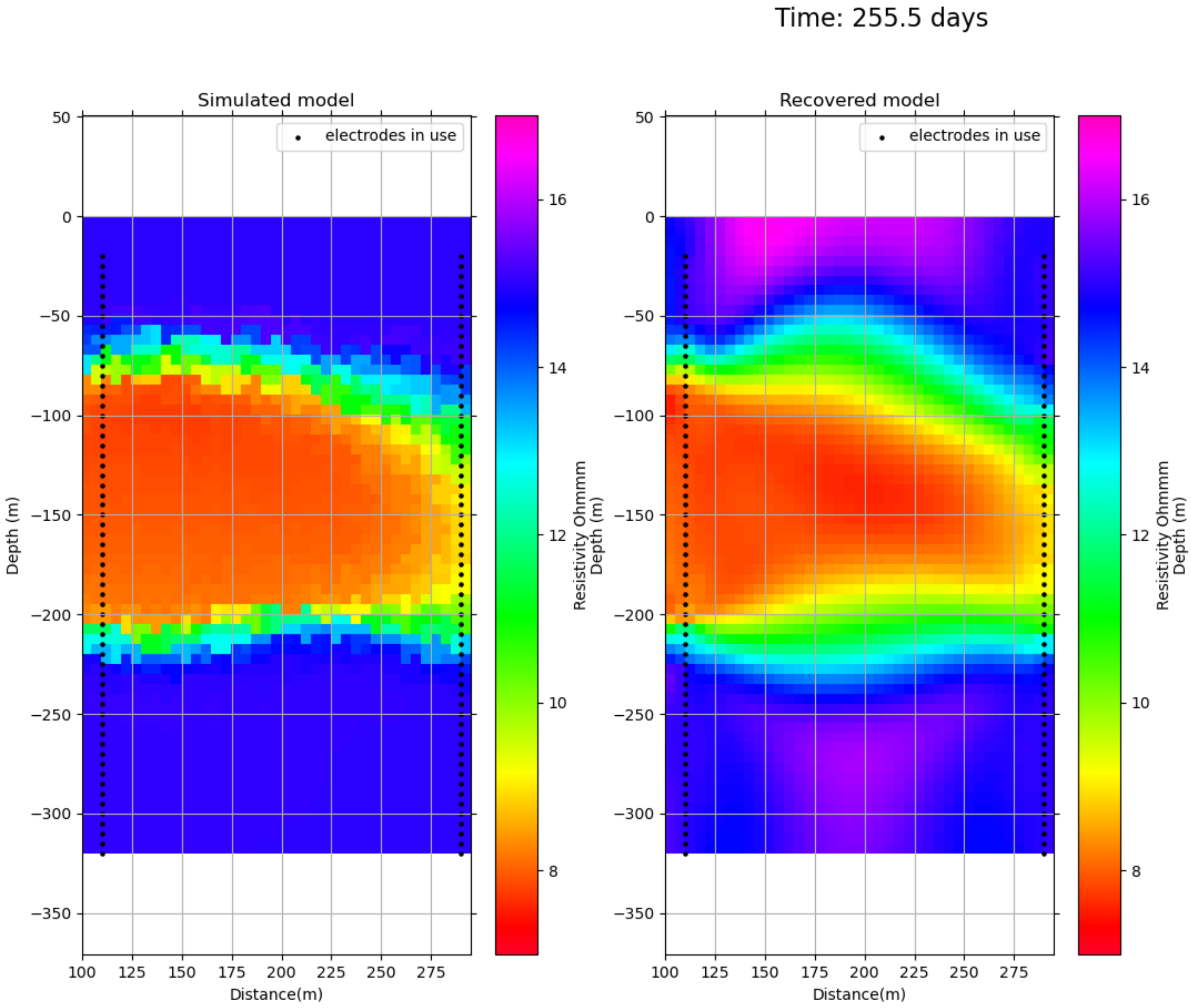

Figure 3 Results from a synthetic modelling example; left: real, synthetic resistivity; right: resistivity distribution obtained from ERT measurement. The electrode locations are denoted by the small black dots.

In this example, the ERT measurements provide useful information for the electrical resistivity and therefore also for the temperature distribution.

The lab experiment was executed in a sand-filled tank of 5.5m x 7.0m x 2.5m. Hot water was injected in one well and the same volume of water was subtracted from an adjacent well. The ERT monitoring set up around the injection well and is shown in Figure 4. The ERT cross-hole set-up consists of 4 boreholes with 11 electrodes per borehole (total 44 electrodes). The spacing between the electrodes is 20cm. Glass fibre along the poles and in a horizontal ‘spider web configuration’ at 4 different depths were used for local DTS measurements for validation. Unfortunately, the spatial resolution of the cross-well spider web data was very coarse and did not provide accurate information.

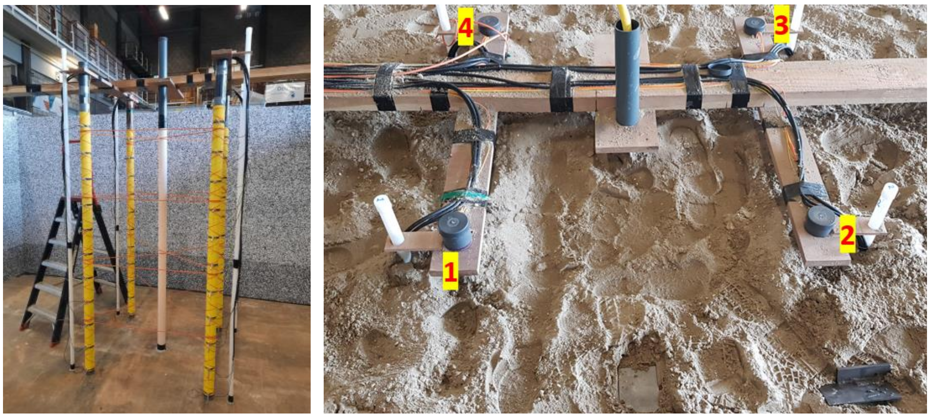

Figure 4 ERT and also acoustic measurements set-up during laboratory experiments; left the 4 pools and glass fibre cables for validation before the tank was filled with sand, right a top view after the tank was filled with sand

In Figure 5, the ERT derived resistivity is shown in the left figures and the DTS interpolated temperature is shown in the right figures for two times. Unfortunately, it is impossible to derive the temperature distribution from this experiment as we must conclude that another process, that also impacts the resistivity, has taken place. We have the hypothesis that it is either compaction or severe particle transport. The hypothesis is based on the increase of the resistivity that can be explained by a decrease in porosity. The increase of temperature gives a decrease in resistivity. At early monitoring times, we do see an increased resistivity along the center of the y-axis which is the location of the injection well, see Figure A22 in appendix A and therefore we conclude that disturbing process started at the injection well.

In the past, the ERT technique has been applied successfully at the Vitens drinking water ‘t Klooster where temporally water is injected for subsurface iron removal and the injected water has a slight temperature difference (Karaoulis et al., 2019).

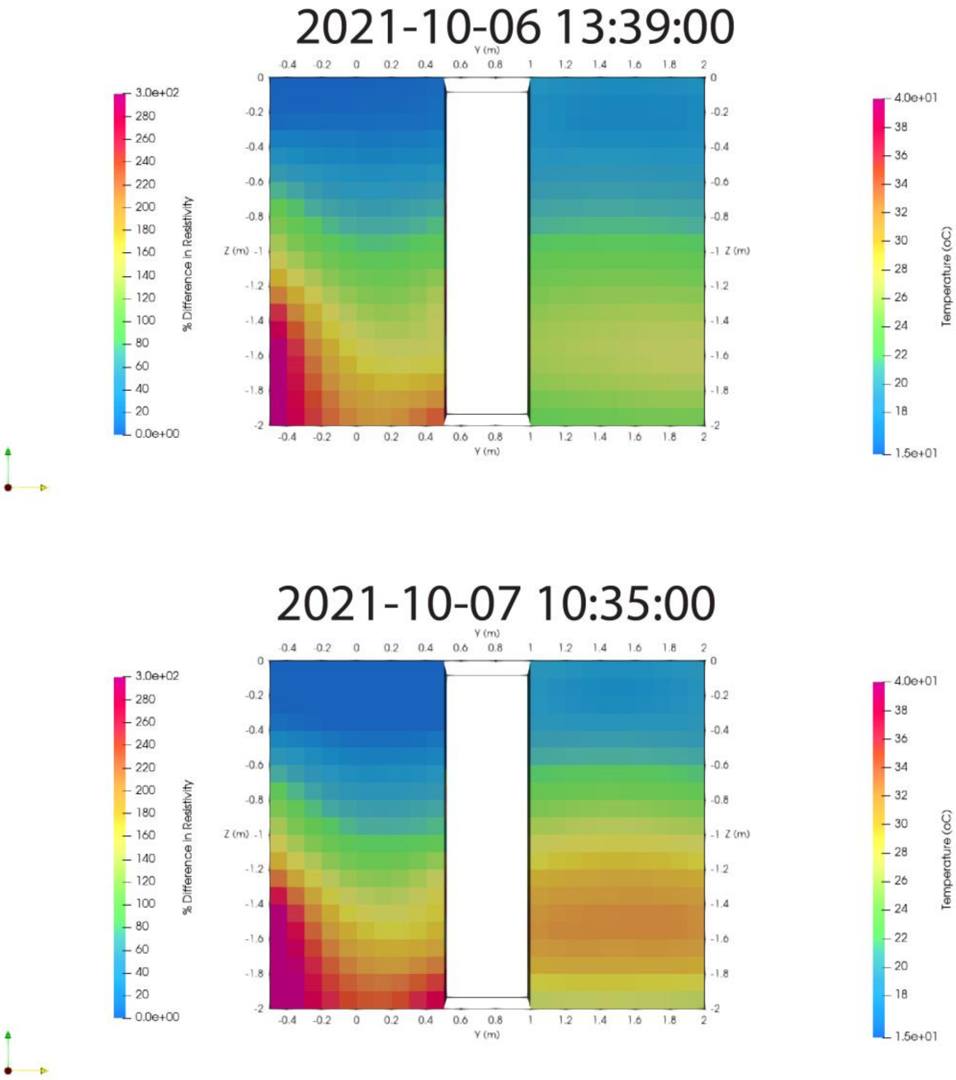

Figure 5 Snapshots of ERT analysis (left) and DTS interpolated data (right) at two times during the laboratory experiment

Expected temperature data results

- Location of data/ Resolution

The data is gathered for numerous combinations of electrodes. The electrodes themselves will be placed in the production and/ monitoring wells, provided that they do not contain any metal. The vertical resolution of the temperature distribution derived by the ERT measurements is equal to half the distance between the electrodes. So if the electrodes are placed at 1.0 m distance, the temperature distribution can be obtained for 0.5 m vertical resolution.
The horizontal extent that can be imaged with a good resolution is about ¼ of the distance between the highest and lowest electrodes in the wells. So, if a storage aquifer is 30 m thick and

the electrodes are placed at 60 m distance (from the bottom of the aquifer to 30 m above the top of the aquifer the front of the hot water plume can be obtained clearly up to 15 m from either well. This extent can be increased by putting the outer electrodes at a larger distance, but that would require either drilling deeper than the bottom of the aquifer or putting the electrodes asymmetric around the top of the storage aquifer.
Combining the time lapse information with a heat transport model may also improve the extent at which a clear thermal evolution image can be obtained, but that would require further research.

- Accuracy

According to the specialist an accuracy of less than 1.0 degree Celsius is possible.

- Costs

The execution of the ERT measurements demands the drilling of the wells, the installation of the equipment and the execution of the measurement including data analyses.

The costs of the drilling of the wells depend on the depth of the storage aquifer. If the production wells of test drilling can be used, it would save costs as they need to be drilled anyhow. However, the wells cannot be made of metal as it would disturb the ERT measurement severely.

The purchase and installation of the electrodes and further monitoring equipment costs about 80 k€.

The measurements themselves including processes is fully automated and can be executed numerous times per year for 10 k€. Provided that no unforeseen calamities take place and a personal visit to the site is necessary.

- Limitations of technique

The ERT measurements cannot be applied when metal is present in the wells that are used for the monitoring. So, if steel pumping wells are applied, two additional monitoring wells are needed to do ERT measurements.

Also, any changes in the porosity may also disturb the translation from the resistivity to temperature. If these changes are only very close to the injection well, it may be possible to still obtain accurate temperature distribution further in the aquifer, but that would require further research.

- Future research

For future research it is recommended to:

1. apply and validate the ERT technique at a real HT-ATES field site;
2. combine its result with a heat transport model and validate its predictions with other types of data, for instance the time series of DTS data in a monitoring well.
3. Analyze the effect of particle transport and account for its effect on the ERT.

3 Acoustic cross-well tomography

This chapter gives a short description of the technique and the modelling and laboratory results. In Appendix B an extensive description is given.

Short description of technique

Acoustic cross-well tomography (ACT) method uses travel times of an induced acoustic wave. It is typically applied in a two-neighbors borehole set-up. One of the boreholes is utilized to install an acoustic source (which is moved at various depths) which generates acoustic waves. These waves are recorded by an array of single or multi-component receivers localized at the neighbor borehole, see Figure 6. The recorded travel times from various shots at different depths are utilized to retrieve the primary wave (P-wave) and/or secondary wave (S-wave) velocity structure between the two wells.

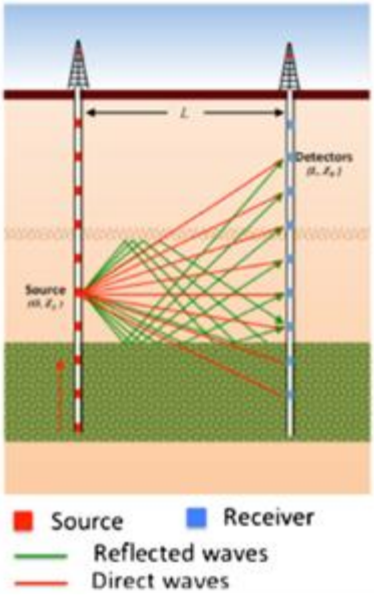

Figure 6 Schematic diagram of a cross-well seismic survey. The geometry consists of many source points (red) and many receiver points (blue) (Raji, Gao, & Harris, 2017)

The travel time depends on the wave velocity in the subsurface medium and is amongst others dependent on the temperature. By comparing the travel time during heat storage with travel time before heat storage information about the temperature distribution is obtained. For a single acoustic source and a single receiver, only a spatial averaged variation in the change of the wave velocity along the trajectory between source and receiver would be obtained. However, by using multiple receivers and applying the acoustic source at various depths, more information along unique trajectories is obtained which is used to generate a temperature distribution over the entire cross-section.

The technique was tested in a synthetic model and a laboratory experiment. For the synthetic model a heat transport model was used to simulate a thermal evolution during heat injection in a slightly heterogeneous aquifer, using different injection temperatures. At two different times, acoustic measurements were simulated and used as the only data source to recover the thermal evolution. The real synthetic primary wave velocity for an injection with 45 °C and the recovered thermal evolution at one time step for different injection temperatures is shown in Figure 7.

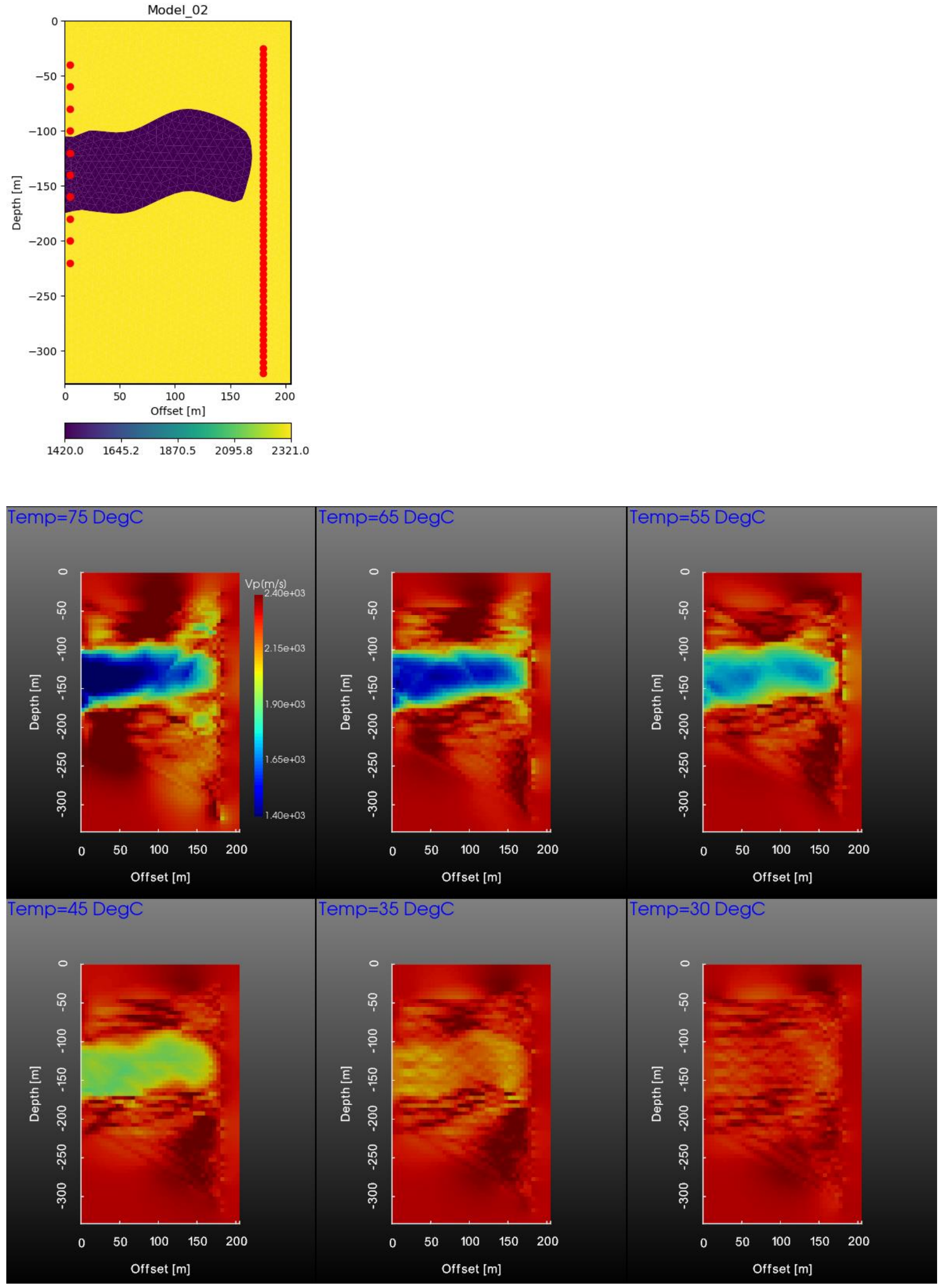

Figure 7 Results from a synthetic modelling example; top: real, synthetic wave velocity after injection with 45 °C with acoustic source (left well) and receiver locations (right well) ; below recovered thermal evolutions for various injection temperatures obtained from acoustic measurements

In this example, it is clear that the acoustic measurements provide useful information when the injection temperature is at least 45 °C.

For the lab experiment the same set-up was used as was described in the chapter of the 2 Electrical Resistivity Tomography. The acoustic monitoring set up is shown in Figure 4. Pole 3 was used as the acoustic source receivers are in poles 1, 2 and 4. Glass fiber along the poles and in a horizontal 'spider web configuration' at 4 different depths were used for local DTS measurements for validation. Unfortunately, the spatial resolution of the cross-well spider web data was very coarse and only depth average values near the wells were used for comparison.

In Figure 8, the spatial averaged wave velocity difference between pole 3 and 1 as obtained by the acoustic measurements is shown as well as the depth averaged temperature of the DTS measurements in both the poles and near the injection well (SPW) as a function of time.

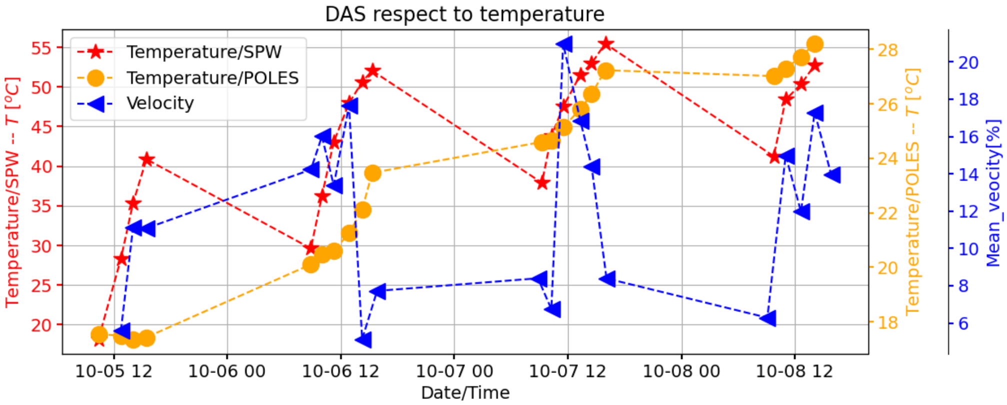

Figure 8 Spatial averaged acoustic wave velocity difference and DTS temperature measurement during laboratory experiment.

Note that the wave velocity difference is a spatially averaged value between the two poles whereas the DTS measurements provide local data. During the first day there is a clear correlation between the increase in temperature and the change in acoustic wave velocity difference. After the first day there is a sudden strong change in the wave velocity. We have the hypothesis that some compaction has occurred that also changed the porosity and consequently also the acoustic wave velocity. Therefore, the change of the acoustic wave velocity cannot be solely explained by the temperature change any more. An exact relation between the change in wave velocity and the temperature during the first day is not known for this laboratory experiment.

At the depth of a real field application, we would expect no problems with compaction, but particle transport or clogging may be of importance. The issue with the relation between the wave velocity and the temperature could be resolved by using information from the injection temperature into the data analysis. The technique seems promising for field applications, but additional research on a real field location is still needed.

Expected temperature data results

- Location of monitoring equipment/ Resolution

The monitoring equipment consists of an acoustic source and a fiber optic cable. The fiber optic cable is installed at the outer diameter of a monitoring well or production well. During a set of measurements, the acoustic source is put into a well and shifted to the desired depths where the acoustic signals are given.
The vertical resolution strongly depends on the vertical separation of the receivers as well as the vertical distance between the source locations that are applied. On the other hand, the smallest velocity variation depends on the amount of high frequency energy induced by the source which conditions the smallest wavelength that can be measured.

The horizontal distance between the 2 wells determines the attenuation of the signal and the amplitude of the signal. Field applications in the oil industry show horizontal distances of about 100 m to 1 km, but high frequency signals will decay more rapidly, so there is a trade-off between accuracy (a high frequency signal gives better accuracy) and measurement distance (lower frequency allows for larger distances between the monitoring wells).

- Accuracy

The accuracy of the method depends on how good the exact arrival time of the P-wave can be obtained. In the synthetic example a realistically considered noise of 1% was added to the arrival times. It resulted in a demand of at least 10% difference of the wave velocity, which was obtained for an injection temperature of 45 °C. For the determination of the magnitude of the noise in the acoustic signal and the consequence for the accuracy of the temperature determination, a pilot test at field scale is needed.

- Costs

A standard field survey would consist of a two wells set-up 300 m depth. One well equipped with a fibre optic cable, and the other well to place the acoustic source. An estimate a monitoring campaign of 3 days would be:

Some consideration for the installation:

1. Fibre optic cable -- 6.0k
2. Source rental (5 days) ---------------------------------6.0k
3. DAS interrogator rental (5 days) -------------------- 12k
4. Field survey --- 15.0k
5. Data processing --- 8.0k
6. Reporting --10 k

   Total ---57 k

- Limitations of technique

1. The acoustic cross-well tomography needs at least two boreholes in order two perform the measurements. These boreholes may consist of one or two production well and/or a monitoring well.
2. The technique should be applied when the pumps of a heat storage systems are not active.
3. The technique assumes that besides the temperature, the other aspects that impact the acoustic wave velocity do not change. Any compaction or fracking should be avoided and the effect of particle transport and clogging on the accuracy should be further investigated.
4. The technique requires human presence for positioning the acoustic source and retrieve the data from the receivers.

- Future research

For the acoustic cross-well topography, the following further research is recommended:

1. Apply, test and validate it at a real field site.
2. Combine the data obtained from the technique with information about the thermal evolution, for instance from a heat transport model.
3. Analyze the (potential) effects of particle transport or clogging and if necessary, account for these effects during the data processing.
4. Design a monitoring strategy that can optimally recover the relevant aspects for the thermal evolution, for instance the magnitude of density driven uplifting.

4 Distributed temperature sensing

Mariëlle Koenen[1], Stefan Carpentier[1], Boris Boulenger[1], Dorien Dinkelman[1], Lies Peters[1]
and Wim Bos[2]

[1] TNO, Princetonlaan 6, Utrecht, the Netherlands
[2] ECW energy, Agriport 201, Middenmeer, the netherlands

4.1 Short description of technique

Distributed temperature sensing (DTS) is a technique which uses the measuring of backscattered light along a fibre-optic cable to calculate temperature. By calculating the temperature using a DTS cable installed in a monitoring well useful insights can be obtained on the thermal evolution. The figure below shows the temperature as measured in the monitoring well during the first storage cycle of the HT-ATES system in Middenmeer. Post-processing of the data was required to remove poor data and filter noise. The visualized, processed data show the arrival of the heat front at the monitoring well, the effect of buoyancy, heat losses to over and underburden and retreat of the heat front during production. The combination of DTS measurements and thermal model calibration by history matching provides a powerful methodology to evaluate thermal evolution of the HT-ATES site and study relevant subsurface characteristics such as heat capacity and thermal conductivity of overburden clay layers. This allows improved predictions of overburden heating on the long term, crucial information to demonstrate that drinking water sources can be protected.

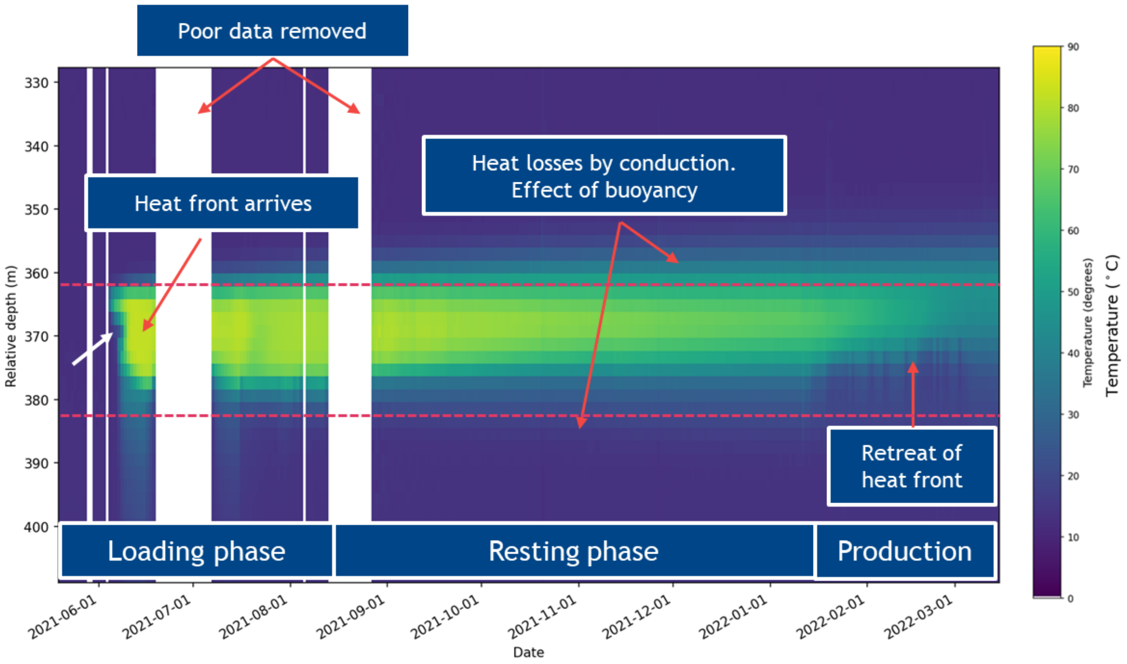

4.2 Expected temperature data results

- Location of data/ Resolution

The vertical resolution of DTS ranges from several meters to several centimeters, depending on the sample rate in time, the amount of available data storage, the required detection threshold etc.

- Accuracy

When installed correctly, the accuracy of the measurements is high (<1°C).

- Costs

The costs for different types of cables vary significantly. There are state-of-the-art, cream-of-the-crop cables with enhanced fibre-optic properties that deliver superior signal-to-noise ratio of fibre-optic measurements which come at a higher price. But in practice for DTS measurements more simple and cost-effective cables are sufficient as DTS constitutes a relatively simple measurement at low-frequency sampling rate.

- Limitations of technique

Installation of a DTS system is a precarious matter and needs careful thinking and execution. Once damage is done to a DTS system, mostly the fibre optic cable, then repairing the damage is extremely difficult, if not impossible. As a result, removal of poor data from the dataset, filtering of noise etc is needed to obtain a reliable dataset. Proven installation procedures are required by certified fibre-optical engineers to prevent occurrences of for example a kink in the fibre-optic cable.
The combination with thermal simulations is required to obtain information on the spatial temperature evolution in the subsurface.

- Future research

The history match methodology will be further improved by matching the production temperature and downhole pressure in the hot well, in addition to the temperature along the monitoring well. In the TKI HTO-PEN, the history matching exercise will be extended with the second storage cycle.
The occurrence and impact of clay swelling in underburden and overburden on temperature measurements needs to be studied.
Improved design of a monitoring well with DTS cable to prevent vertical flow through the (gravel) material around the tubing, preventing distortion of the temperature signal.

5 Pulse testing

Peter A. Fokker[1], Dario Viberti[2], Eloisa Salina Borello[2], Francesca Verga[2], Jan-Diederik van Wees[1], Arjan Konijn[3], Wim Bos[3], Mariëlle Koenen[1]

[1] TNO, Princetonlaan 6, Utrecht, the Netherlands
[2] University of Turin, Giuseppe Verdi, 8, 10124 Torino TO, Italië
[3] ECW energy, Agriport 201, Middenmeer, the netherlands

5.1 Short description of technique

Harmonic Pulse Testing (HPT), or pulse testing in short, is a technique to determine the thermal front in HT-ATES (or geothermal) systems during ongoing operations without requiring significant alteration of the net production or injection. The technique makes use of the viscosity difference between water with high and low temperature. By imposing a regular alternation of two rate values in an injection well, a periodic pressure response can be measured using pressure gauges, preferable downhole, which can be used to calculate the thermal front. The equations for a radial system, which can be used as an approximate for the storage well of an ATES system, can be found in Fokker et al. (2021). The design of the pulse test, e.g. the rate variation and duration, depends on the injected volume and approximation of the thermal front; the farther away the front, the higher the duration of the pulse and the larger the rate change.

Pulse testing has been applied in the HT-ATES system in Middenmeer, the Netherlands. A baseline pulse test prior to heat storage was followed by a test after 5 days of storage. At the end of the storage phase, the pulse test was repeated. The results show that it is possible to deploy this technique to obtain knowledge about the reservoir properties, including the position of the thermal front. The technique has potential as a powerful monitoring technique but needs to be designed with care and operated with dedicated monitoring equipment. Several improvements are required in the design of the pulse test compared to the test as executed in Middenmeer. One of them is that interference with the effect of simultaneous pulsing of the producer well must be incorporated in the analysis. For details of the pulse tests in Middenmeer, see Appendix.

5.2 Expected temperature data results

- Location of data/ Resolution

The data resolution depends on the design of the pulse tests and the frequency of measurements of the pressure gauges.

- Accuracy

The technique gives an average value for the thermal front, which implies that the lower the buoyancy effect, the higher the accuracy. However, a combination of issues in the present test made it difficult to quantify the accuracy.

- Costs

Downhole pressure gauge including data acquisition system and well connector costs roughly 50 k€.
Estimation of man hours for the tests and evaluation: ~20 k€
The technique is very cost-effective since it does not need a dedicated monitoring well but the downhole pressure gauge is costly.

- Evaluation of the technique and limitations

The technique has potential as a powerful monitoring technique but there are some conditions that need to be improved in comparison with the tests performed in Middenmeer, and some uncertainties and limitations may remain.

- When pulse tests in a doublet are not performed independently, i.e. when production and injection in the two wells are coupled and pulsed in the same way, interference will show up. The pulse period at which this happens depends on the distance between the wells and the reservoir properties. In the tests performed in Middenmeer, interference was clear and needed to be accounted for. We created a basic method to account for the interference; this should be further validated and developed. Simultaneous evaluation of the signal in the producer well could possibly be helpful in such analyses.

- Bottomhole pressures are instrumental in collecting high-quality data. Bottomhole pressures are not influenced by friction and by fluctuations in hydraulic head. The latter were present in our last test due to the varying injection water temperature and the associated density variations. A reliable calculation of the hydraulic head would involve more than what we have been able to do here: in particular the temperature development of the stagnant measurement tubing could not be faithfully determined.

- Temperature variations of the injected water should be prevented during the pulse test. For an unambiguous analysis it is beneficial to not change injection rate and temperature simultaneously. Temperature variations can, however, bear additional information: they inflict pressure fluctuations at the point of injection because the temperature in the reservoir also fluctuates and through the water viscosity causes fluctuations of the viscous pressure drop in the reservoir. For a robust analysis, either temperature pulse testing or pulse testing by injection rate should be performed.

- The interpretation of pulse tests relies on the calculation of a pressure derivative vs harmonic period. This is easier to obtain when many frequencies can be used. It is therefore important to have fast switching procedures of the injection rate – fast switching results in many more observable high-frequency signals. For the longer times, it is beneficial to complement a pulse test with a traditional well test with pressure transient analysis during shut-in.

- Pulse testing, when performed properly, will result in an average thermal front. Yet, the heat front around the injector cannot be expected to be radially symmetric and independent of depth, especially further away from the injection well. This is due to gravitational upwelling of the hot brine as well as permeability subject to more or less heterogeneity. Furthermore it cannot be excluded that viscous fingering can occur as a consequence of the low viscosity ratio of injected and reservoir brine. Finally, the production from the other well will cause preferential flow in that direction.

- Future research

It is important to build more confidence in pulse testing technology by applying it to storage operations using a downhole pressure gauge. Interference with the producer well requires a dedicated theoretical treatment.

6 Comparison of techniques

For several aspects, the four techniques are compared. In the present study, only the DTS measurements are combined with a heat transport model calibration whereas the other techniques are not. These techniques, however, could also be combined with a heat transport model, which will be studied in the follow-up project WarmingUP GOO.

Experimental / Field experience;

The Distributed Temperature Sensing (DTS) technique has been applied frequently in the Netherlands in low-temperature thermal energy storage projects and also on the HT-ATES systems of ECW-Middenmeer and at Koppert Cress. The Harmonic Pulse Testing (HPT) method has only been applied in heat storage on the HT-ATES in Middenmeer.

The Electrical Resistivity Tomography (ERT) has been applied successfully during the injection at a drinking water well with a deviating injection temperature, but not in a real world HT-ATES-system in the Netherlands. It has been applied numerously in geological characterization. It was also applied in the laboratory set-up in this project, provided numerous data but the interpretation of the data was difficult as the experiment was disturbed by an unforeseen change in the sand containers, presumably compaction.

The Acoustic Tomography (AT) has not been applied to real world heat storage systems in the Netherlands but has been applied in geological characterizations. It was also applied in the same laboratory set-up in this project and provided numerous data, but the interpretation of the data was also difficult.

Robustness

The DTS technique is quite robust as it obtains a temperature measurement directly at the measurement location. For the DTS monitoring in Middenmeer some filtering was needed to correct for noisy measurements. The calibration of a heat transport model using the DTS measurements in this study did not fully recover the time varying temperature profiles as measured by the DTS, but additional research on history matching is highly promising.

The other techniques obtain measurements that are impacted by the thermal evolution over a larger area and make use of the difference in the measurement data with a baseline to derive the thermal evolution. Any additional changes to the subsurface, such as particle transport near the production well, may hinder the interpretation of the data.

The robustness of the combination of any of these techniques with a numerical heat transport model has not been studied in general. It is presumably dependent on the heterogeneity in the subsurface and consequently a more or less smooth temperature distribution.

Resolution

The DTS technique can provide data on the scale of several meters to several centimeters, but only at the monitoring well. By combining it with a heat transport model estimates of the thermal evolution within the reservoir, but also at under- and overburden can be obtained, but its accuracy strongly depends on the success of the model calibration.

The HTP provides an estimate of the location of the front of the plume and the resolution depends on the design of the pulse test and the frequency of the measurements.

The vertical resolution of ERT equals half the electrode distance and a resolution in the order of a few meters can easily be achieved. The horizontal extent which gives good estimates is about 1/4 of the distance between the upper and lower electrodes.
For the AT the vertical resolution depends on the vertical distance between the receivers as well as the vertical distance between the acoustic source locations. The horizontal distance between two wells that are used in the AT should not be too large as the acoustic signal is attenuated; in oil industry application distances of 100 m to 1 km are applied.

Accuracy

The DTS technique can provide accurate measurements (<1 °C) when installed correctly at the measurement location. The HPT technique gives an estimate for the average value of the thermal front and its accuracy is expected to be higher when the buoyancy effect is smaller. In this study it was difficult to quantify the accuracy of this technique.
For ERT the expected accuracy is less than 1 °C. For AT the accuracy depends on the noise to signal ratio, but in a realistic considered synthetic example an injection temperature that is 15 °C higher than the aquifer temperature was needed to obtained good results.

Costs

The DTS measurements are relatively cheap and once installed can easily provide data for multiple times. Analysis and filtering of the monitoring results including calibration of a heat transport model can be time consuming and costly. The costs for HPT are approximately 50 k€ for investment costs and 20 k€ for operational costs. For ERT, the investment costs are estimated at 80 k€ and the operational costs are 10 k€ per year for numerous measurements per year. For AT the estimated costs are 57 k€ for each measurement period.

The DTS and ERT measurements can be performed without human presence at the site and can be applied multiple times very cost-efficient, once installed. The AT and HPT technique needs human presence and repeating numerous measurements will significantly increase the costs.

The HPT does not require a monitoring well. The AT may not require a monitoring well if the distance between the hot and warm wells is not too large. ET could be performed in the hot production well, but the horizontal extent that can be measured with good resolution may be smaller than desired.

Limitations

The DTS technique requires a careful installation of the DTS cable and the presence of a monitoring well at a location where the temperature is affected. An estimation about the horizontal thermal evolution can only be obtained when the technique is combined with a heat transport model.
The ERT can only be applied when production and monitoring wells do not conduct electricity considerably and consequently these wells should not contain any steel.

Use of data

Value for validation goal

All techniques can be used for the validation of the heat front displacement. The DTS, ERT and AT can be used to validate the prediction of the buoyancy effect.

Value for operational management goal

For the operational management the monitoring data must help improve to optimize the operational strategy. For both the prediction of the production temperature during ‘normal’ pumping as well as to increase pumping rates in the upper part of the aquifer to counteract the effect of density flow, knowledge about the spatial thermal evolution, including its vertical distribution is crucial. DTS, ERT and AT do provide information about this spatial distribution, but a comparison about the value of monitoring data for these techniques has not been quantified. It will be studied in the WarmingUP GOO project.

7 Conclusions and recommendations

In this report, four different monitoring techniques for temperature measurement during high temperature aquifer thermal energy storage were studied. The DTS and HPT techniques were applied at ECW site in Middenmeer and the ERT and AT techniques were applied in a synthetic and laboratory experiment.

The conclusions of this research are:

- All techniques are able to provide information about the temperature distribution.
- The laboratory set-up for the ERT and AT measurements gave unexpected problems that made it impossible to derive a good temperature distribution. It is probably caused by compaction of the sand during the experiment. These techniques could best be validated in a real-world experiment.
- The field test at ECW Middenmeer gave adequate monitoring results, but specific issues do require additional research.
- The thermal evolution at ECW Middenmeer shows more spatial variability than was predicted by numerical modelling based on the geological characterization before operation.
- DTS, ERT and AT can provide information about the buoyancy effect which is useful during operational management of a HT-ATES system.
- At present the DTS technique is the most mature monitoring technique for heat monitoring at HTS systems.
- The ERT and AT technique have the potential to provide most information about the spatial thermal evolution when model calibration is not considered.
- Calibration of numerical models using data about the thermal evolution will improve estimated about the temporal and spatial thermal evolution.
- ERT can only be applied when no steel is applied in the wells.

Based on this research the following recommendation are made:

- The DTS measurements that are continued at the ECW-site should be analyzed and used during additional model calibration.
- Calibration techniques that can handle more spatial geological variability should be tested for HTS systems.
- The ERT and AT technique should be tested at a real field site.
- The costs of monitoring should be compared with improved benefits from heat recovery of HTS systems using information from these measurements.

Some of these recommendations will be addressed during the follow-up projects WarmingUP GOO and Nieuwe Warmte Nu!

8 Literature

Karaoulis, M., Bakx, W., Doornenbal, P., Kruiver, P., & Rijpkema, S. (2019). Visualising Groundwater Flow Using Time-Lapse Electrical Resistivity Tomography. 25th European Meeting of Environmental and Engineering Geophysics. doi:10.3997/2214-4609.201902439

Appendix A: Electrical Resistivity Tomography; detailed description

A1 Introduction

The Dutch government pursues a rigorous climate policy to achieve the objectives of the Paris climate agreement. Surface water and groundwater are key sources of heating, cooling and thermal energy storage systems. In this work we explore the ERT (Electrical Resistivity Tomography) and DAS (Distributed Acoustic Sensing) geophysical methods, to monitor the development and performed of collective heating systems, when hot water is injected into the subsurface for storage.

The ERT method allows measuring the electrical properties of the subsurface and it is mostly sensitive to the water content. The electrical properties of the water, among other parameters, depend on the temperature and thus making ERT a suitable tool to monitor the warm water evolution (Munoz et al., 2013, Karaoulis et al., 2019). DAS, on the other hand, allows measuring acoustic wavefield that provides valuable information on the dynamic characteristics in geothermal borehole systems. In high temperature storage wells, the high temperatures can modify the elastic properties of the solid media around the well, which can be captured via traditional acoustic surveys.

In this project we perform a laboratory experiment that is compounded by partially saturated sands where an injection and extraction well were installed. We installed 4-well set-up electrodes on each borehole to allow a 4D tomographic inversion of the resistivity data. By imaging the changes on the electrical properties of the subsurface, we can image the evolution of the warm water front.

A2 Electrical properties – property we measure

Electrical properties of soils are related to the chemistry and mineralogy of the soil material and the porosity and any fluids on the grains or in the pores of the soil. The electrical properties can provide indirect indications of the nature of soils and of the spatial variation of the nature of soils. The measurement is known as the direct current resistivity. The Direct Current (DC) resistivity method is an active method aimed at imaging the resistivity (the resistance of a material to the flow of an electrical current) of the subsurface by determine the electric potential field induced by applying an electric potential to a soil at electrodes.

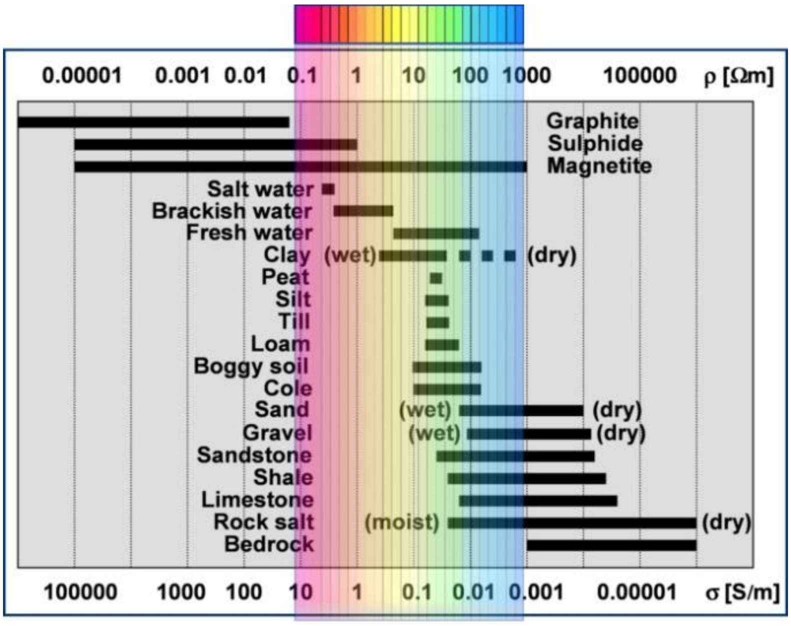

Figure A1 Typical electrical conductivities (resistivities) for diverse materials

A3 ERT principles

The extensive use of ERT in fundamental- and applied research, but also for monitoring all over the world is driven both by the relative ease with which data can be collected and by the thorough understanding of how changes in electrical properties can be interpreted in terms of geo-hydrological and geochemical processes. Resulting in the off the shelf availability of hardware and software. Such software packages have capabilities which can be used to convert time-lapse geophysical data into actionable information on subsurface processes (Karaoulis et al. 2011).

A typical acquisition system for DC (Direct Current) resistivity measurements comprises of a resistivity meter, an electric source (battery), cables with electrodes, a switching box and control and storage unit (computer). For each measurement, two current electrodes are used: one to inject the current into the subsurface and the other to retrieve the same amount of current from it. By convention, these electrodes are named A and B, respectively. The electric field is measured (at least) with two other electrodes (M and N) called the potential electrodes (Figure A2a). The way in which the current and potential electrodes are arranged on the Earth's surface is called an array. By changing the configurations of the array, the properties of subsurface are mapped (Figure A2c). Numerous electrode arrays have been designed and use several electrodes positions along a profile. Using switch boxes allows for a large number of measurements to be taken in a short time, resulting in the capability for repeating measurements over longer time periods (time-lapse data) (Figure A2b). These systems are able to collect data with high spatial resolution, allowing better and more reliable tomographic results (Figure A2d).

To increase vertical resolution, electrodes can also be places within boreholes, allowing higher resolution imaging between the boreholes. Boreholes can be placed in a 2D plane or distributed in 3D to get 3D tomographic images. Collecting data over time (time-lapse ERT), we can image the resistivity property in 4D dimensions.

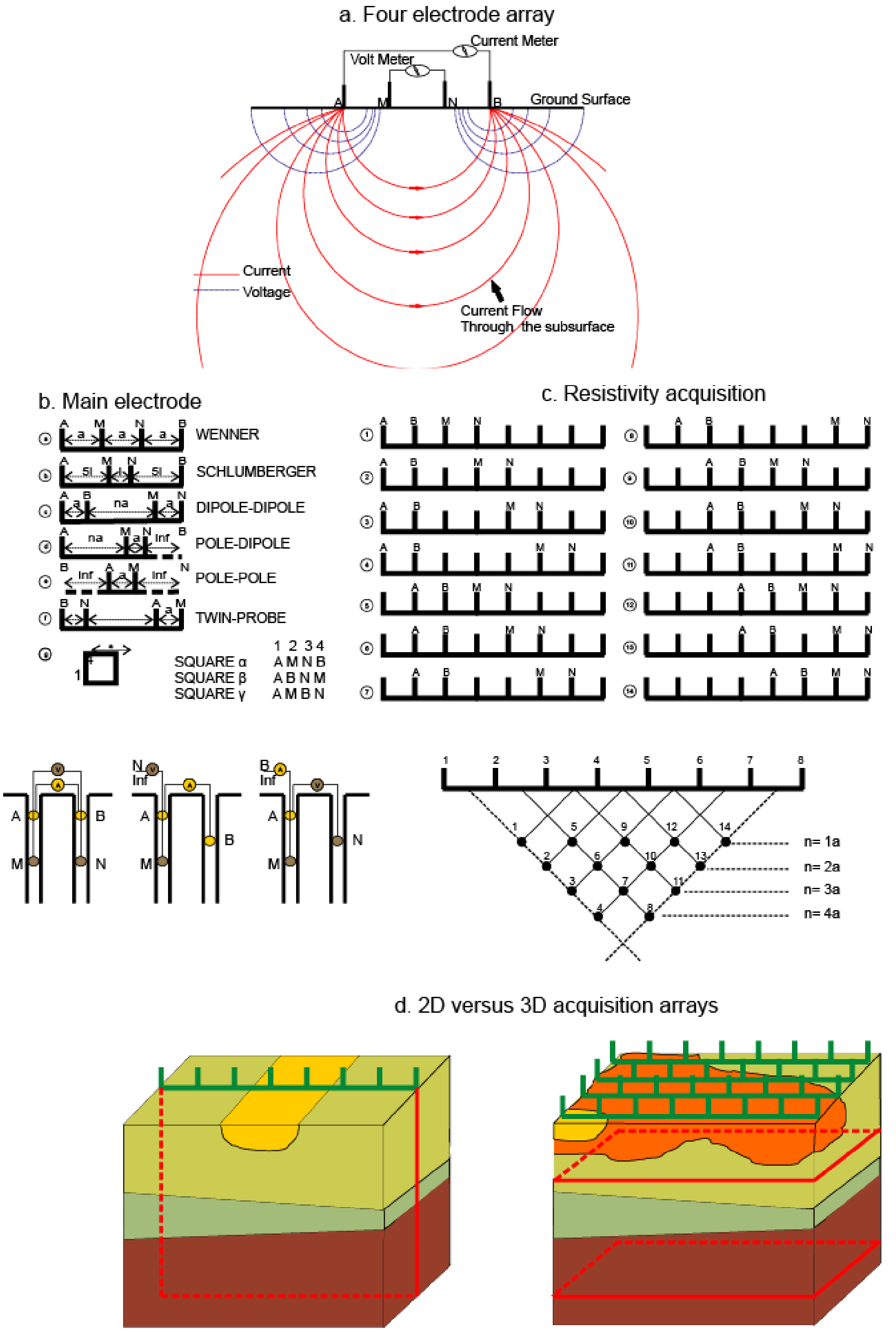

Figure A2: a) The principle of an ERT measurement, showing the currents in a cross-section; b) The effect of the spacing in the look-ahead of the measurements; c) Using 3 or 2 electrodes to increase the look-ahead of the measurements (source: Karaoulis et al., 2014)

The resistance R (in ohm) measured across a cylindrical sample of resistivity ρ (in Ohm m), length L, and cross section A is given by R = ρ L/A, where g = A/L (in m) is called the geometric factor. For field acquisition, the geometric factor depends on the position of the electrodes as discussed below. The resistance is obtained by applying Ohm's law, U = R I, where U is the voltage (difference of potential) in volts measured between M and N and I is the strength in amperes of the injected current. During measurements, the volt- and current meter are calibrated to check the accuracy of the measurements for a broad range of resistances.

By using multiple electrodes spread on the surface or in the water bottom (for resistivity acquisition), a tomographic resistivity image of the medium can be obtained. The way in which the current and potential electrodes are arranged is called a resistivity array. A large number of electrode arrays have been suggested in the literature, but only a few such as ‘dipole-dipole’, ‘Schlumberger’ and ‘Wenner’ array, are extensively used. The main characteristic of an array is its geometrical factor, which is uniquely related to the respective distances between the probes as discussed above. The choice of a particular resistivity array for a survey is based upon considerations regarding theoretical advantages and drawbacks of the array and its signal-to-noise ratio (Ward, 1990). More recently, approaches have been suggested to compute optimized measurement protocols, i.e., which provide best resolution, based for instance on sensitivity criteria (e.g., Stummer et al., 2004).

In the general case of a heterogeneous medium, for any possible four-electrode arrangement the geometrical factor g, when multiplied with the measured resistance R, yields the so-called apparent resistivity ρ_a,

$$\rho_a = R \cdot g$$

The apparent resistivity ρ_a represents a weighted average of the true resistivity of the subsurface. By definition, the apparent resistivity is equal to the true resistivity in the case of a homogeneous medium. Generally, however, the true resistivity is only obtained after inversion of the apparent resistivity data (see section below).

Inverse modelling is the procedure to convert apparent resistivity data to an inverted resistivity image, also called a tomogram. Correspondingly, the approach to construct an electrical tomogram is also referred to as electrical resistivity tomography (ERT). Inverse modelling is usually performed with deterministic approaches. These approaches look for retrieving the true resistivity distribution of the ground from the apparent resistivity data. In other words, inverse modelling seeks to find a resistivity model that explains (or “predicts”) the given field measurements. It is obvious, that the initial step of inverse modelling is to perform a forward modelling (what are the apparent resistivity data for a given resistivity distribution?). This is done by solving numerically the Poisson equation for the electric potential. There are many references on how to solve the Poisson equation in both 2D and 3D, using numerical methods like the finite-element method, the finite-difference method, or the boundary element method. More general information about the method and its applications can be found in Revil et al., 2012.

A4 Synthetic modelling and laboratory experiment

The performance of the ERT was tested in both a synthetic modelling and a laboratory experiment.

A4.1 Modelling description

The spatial resolution in an ERT as mentioned, depends on two parameters. The spacing between electrodes placed within each borehole and the spacing between the boreholes. While the costs associated with the number of electrodes per borehole in typically not a limiting factor, the spacing between boreholes has huge effect on the budget. In a typical crosshole scenario, the area that can be imaged with good resolution is about ¼ to the total length of each borehole. In other words, there are two ways to increase the resolution of the area between two boreholes

- Decrease the distance between two boreholes
- Increase the length of each borehole.

The impact of the distance was tested in a synthetic experiment. The model geometry consists of three geological layers, one sandy layer where the infiltration takes place and two clay layers to confine (for permeabilities see Figure A3). The layers, their elevation are interpolation functions from an artificial dataset that represents potentially expected field conditions. Different hydraulic and thermal properties are defined for the layers as starting model, to represent a gradient in salinity and temperature with depth (Figure A4 and Figure A5). A natural groundwater flow is presented as can be seen from the initial hydraulic heads in Figure A6. In this simulation we infiltrate warm, brackish water of 90 °C, into a less brackish water (than the infiltrated) and temperature of about 30 °C. The evolution of the flow and temperature field over 10 years is simulated. The location of the wells is shown in Figure A7. The results of the simulation are discussed in paragraph 0

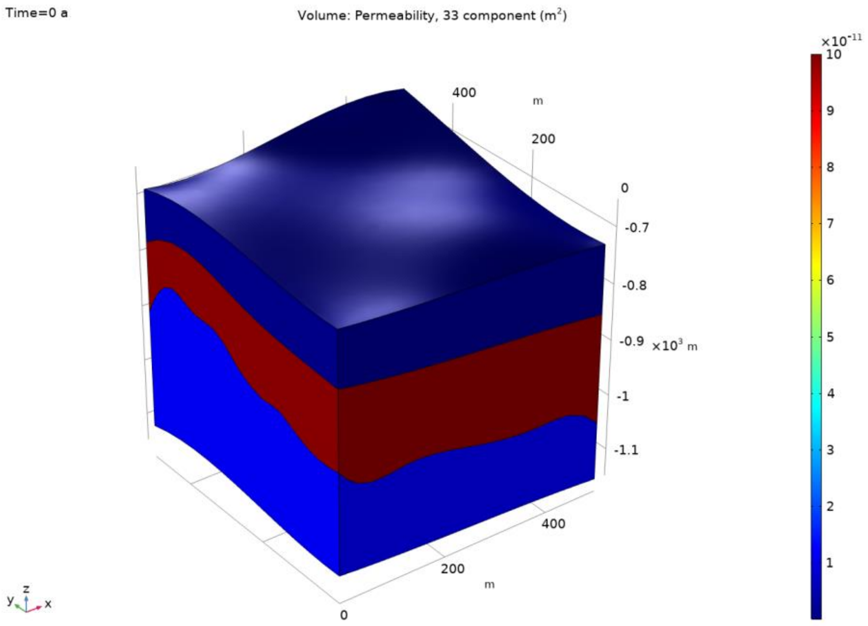

Figure A3 Permeability values of the three layers simulated

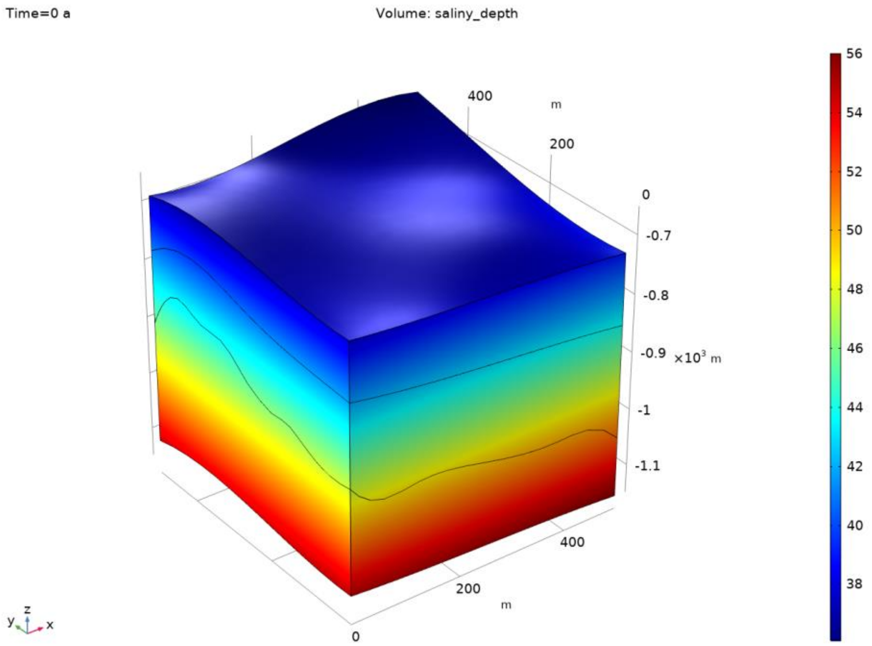

Figure A4 Initial salinity simulated

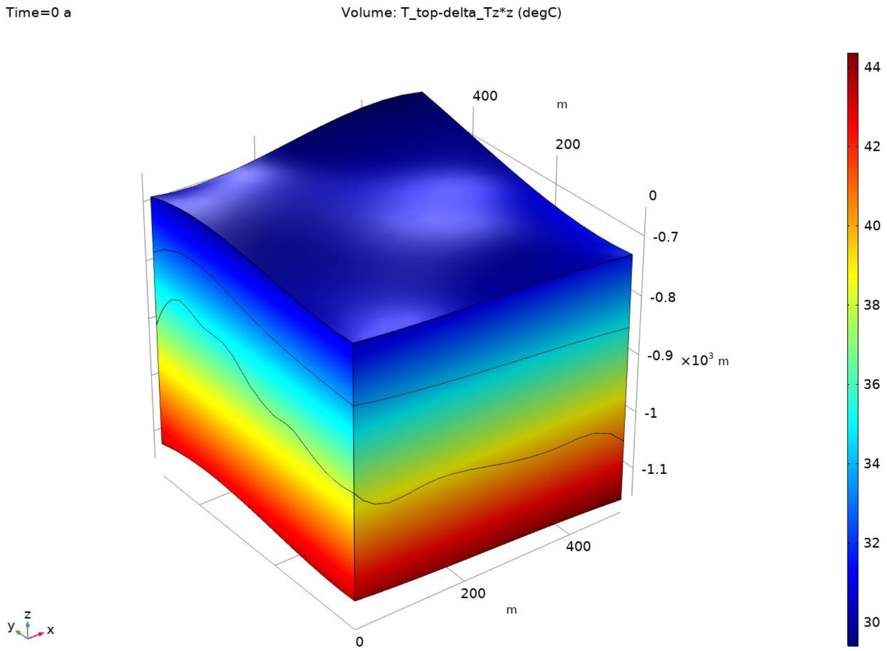

Figure A5 Initial temperature

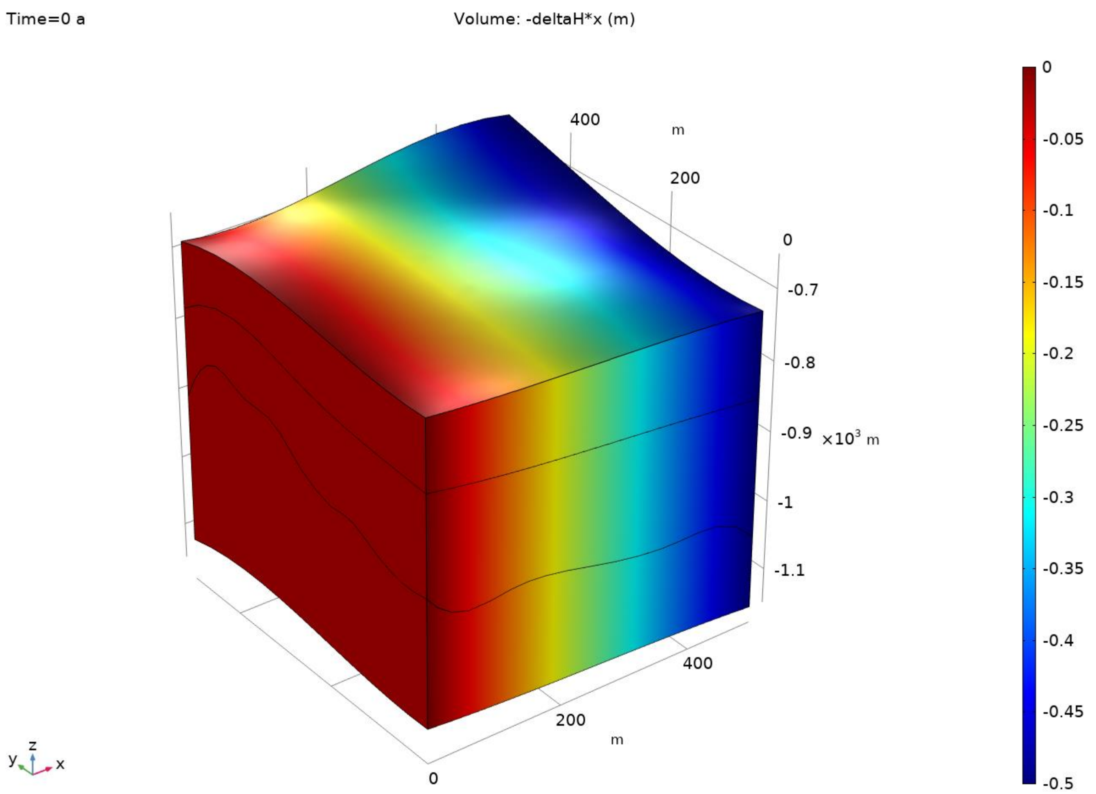

Figure A6 Initial hydraulic heads

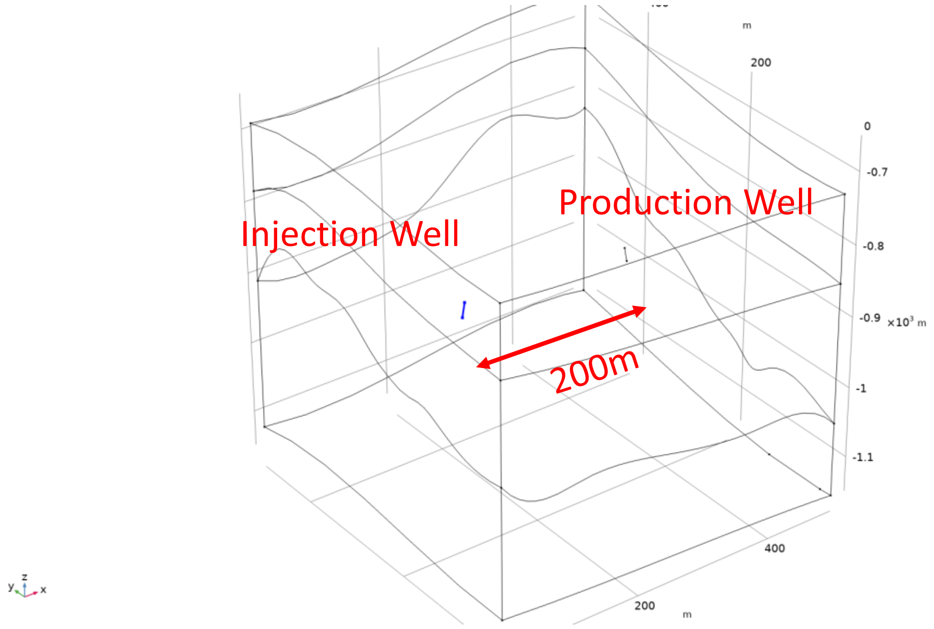

Figure A7 Location of injection and production well 200m apart. Infiltration rate of 190 L/sa5.2

A4.2 Lab experiment description

Lab setup

The ERT measurements were carried out in the Geohal facilities at Deltares. The test site is comprised by partially saturated sands contained in a rectangular tank of 5.5 m x 7.0 m x 2.5 m. The survey set-up consists of 4 poles arrayed in a square shape of 1.0 m separation. In the middle of the square array there is an injection well where hot water is injected. In order to maintain the injected water circulating within the tank, an extraction well is localized at 5.8 m from the injection well.

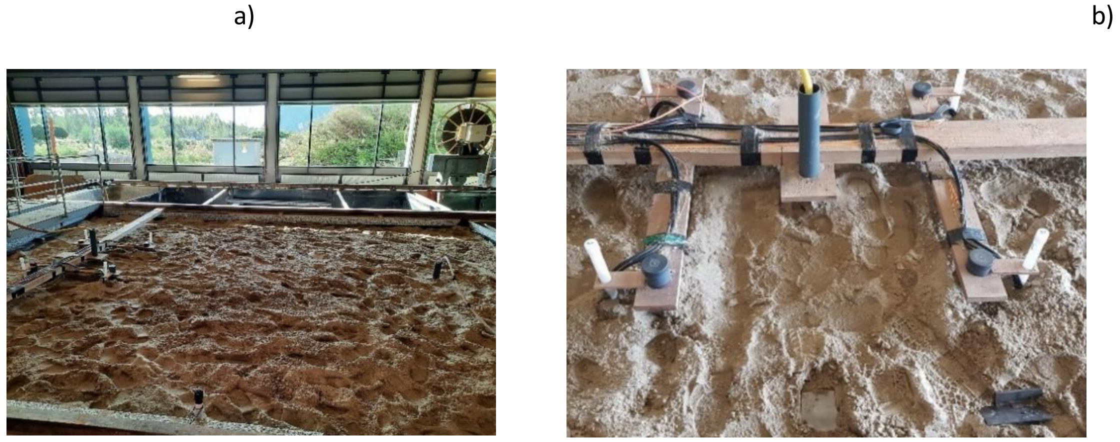

Figure A8. a) Overview of the test site with the DAS array, the injection and extraction wells, and b) Top view of 4-pole array for the cross-hole test.

Cross-hole set-up

The ERT cross-hole set-up consists of 4 boreholes with 11 electrodes per borehole (total 44 electrodes) (Figure A9). The spacing between the electrodes is 20 cm.

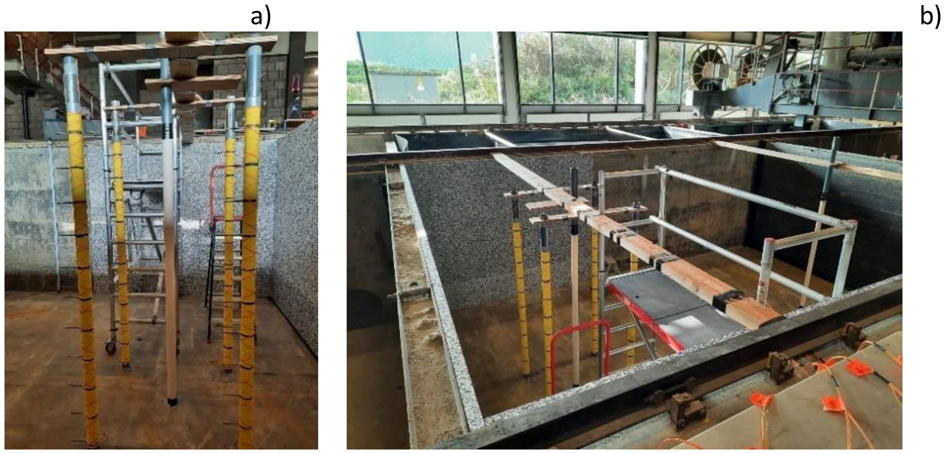

Figure A9: a) ERT array along 4 survey poles, and b) 4-poles array including injection (within the ERT array) and extraction (at the right end) wells.

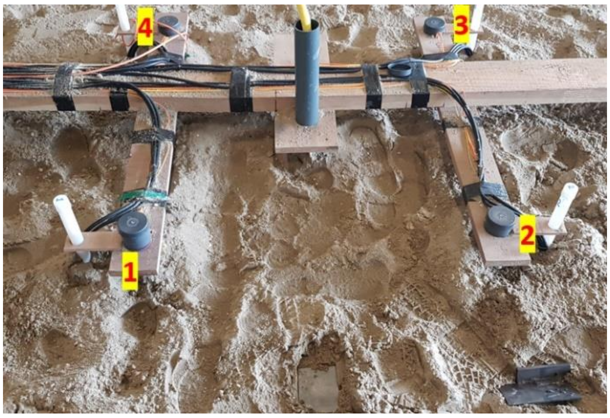

Figure A10: Lay-out of 4-pole array for cross-hole surveying. Name assigned to each survey pole is indicated by red color numbers.

Using a combination of pole-tripole, bipole-bipole and multigradient array, each acquisition consists of 428 measurements. Each data acquisition (cycle) takes about 4 minutes and we repeat each cycle every 10 or 20 minutes, depending on side activities during the injection.

It is important to notice, that ERT gives a tomographic model (a true 3d model), where the DTS data we use for validation, sense the warm water when the water from does reach the cable itself. All information in between the boreholes, in the DTS case, is a simple interpolation.

We recorded 210 time-lapse ERT data, and for each time-step we compare the result with the DTS. For simplicity, we will show only one cross section along the volume, to make comparison easy. The data collection was split in 4 sections section
1) 5 October, 8.00 till 16.25
2) 6 October, 8.00 till 14.30
3) 7 October, 8.40 till 16.30
4) 8 October, 9.00 till 12.30. ERT continued to measure till 9 October.

In the beginning of each section, the operator started the geophysical measures, did a quality control on the status, turned on the pumps and started the infiltration. In the end of each day, all systems were shutdown and no infiltration took place during the night.

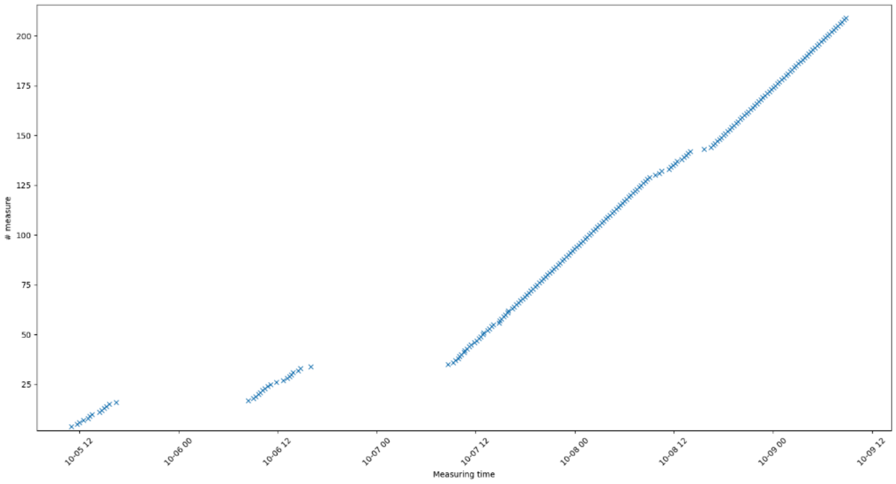

Figure A11 The time schedule of each ERT data time step.

A4.3 Data processing

The collected data from this experiment are potential differences between the transmitting and receiving electrodes, and depend upon the distribution of the subsurface resistivity, which is the material property we are interested in. Before starting with data processing, an evaluation of data quality was undertaken. At this stage, erroneous data, appearing as unreasonably high or low values, are filtered out. Erroneous data can result, for example, from electrical noise and improper electrode coupling to the ground. Filtering was performed on all lines to ensure optimal data quality.

Inversion aims to determine the subsurface resistivity configuration that gave rise to the measured data at the surface. It is a mathematical optimization procedure which uses the acquired data as input and the prior knowledge (for example the depth to certain layers) to constrain the produced models.

The subsurface below the lines is first meshed into a grid. Inversion processing starts with an initial estimate of the subsurface resistivity configuration based on prior information. A geometrical factor, accounting for the electrode's topography and relative location is applied. The algorithm then proceeds with a forward calculation on this model to predict the potential differences that would arise if a survey were carried out over it.

At this stage, the actual field data are brought in and the inversion algorithm calculates the misfit between the actual data and the initial predicted mode. Depending on the desired misfit between the model and the measurements, additional iterations of this process will be performed (i.e. new configurations generated and tested), until a suitable model (satisfying the misfit criteria and inversion iteration numbers) is reached. The mathematically acceptable model must then be assessed for its geological and geophysical plausibility. The workflow is shown in Figure A12.

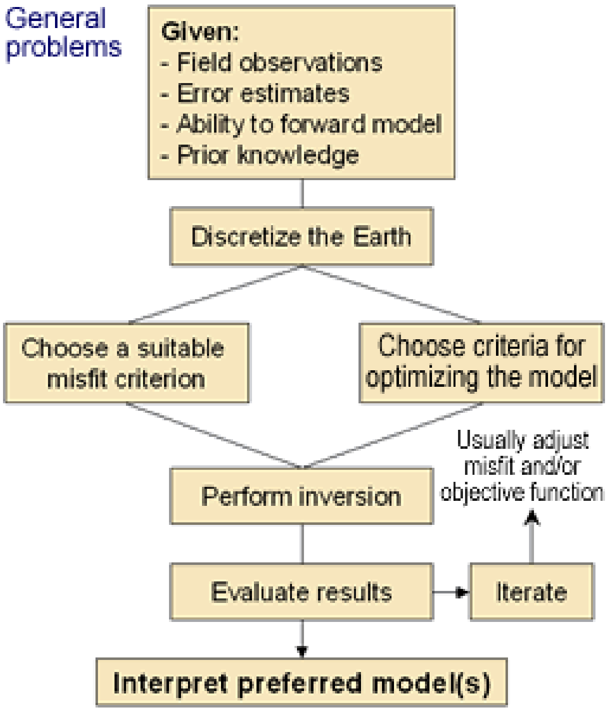

Figure A12 The data processing workflow

A geophysical inversion was conducted using the pyGIMLI (Rucker et al.,2017) and Res2DINV (M.H. Locke, 2010) software packages in order to assess the impact of different inversion options (such as the application of smoothing to regulate the sharpness of transitions between different layers) and to identify common features from these results in order to confidently interpret them. After comparing the two sets of results, the pyGIMLI inversions were selected for interpretation due to their greater geological plausibility and lower misfit.

A5 Simulation results

A5.1 Synthetic experiment

Here we present the results that are relevant for the ERT simulations. The main goal of this simulation is indicating the number of boreholes needed in which distance to be able to capture the warm water. Thus, we make a 2D slice based on the simulation results and focus on the temperature distribution after 14.6 and 255.5 days, see Figure A13. We consider 4 cases:

- Case a: 2 boreholes, at 75 m distance.
- Case b: 2 boreholes, at 125 m distance
- Case c: 2 boreholes, at 175 m distance
- Case d: 4 boreholes, at 75 m each.

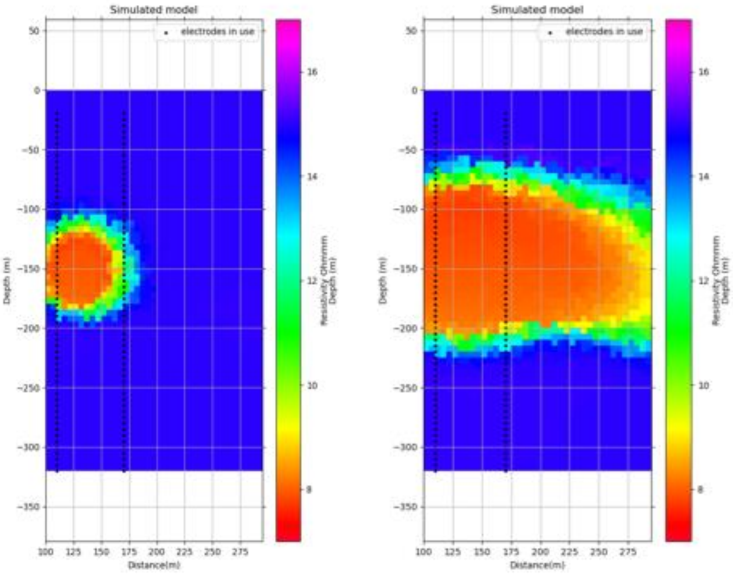

Figure A13 Modelled temperature distribution after 14.6 (left) and 255.5 days (right) in the ERT monitoring profile.

Each figure below is divided in 3 panels. Left panel shows the simulated model, the middle panel the recovered model after processing and the right panel the difference between the simulation and recovered model. Obviously, there we seek to have values close to 1 (meaning that the recovered model matched the simulated one). Here we show the results after 14.6 days of infiltration and 255 days.

Case a

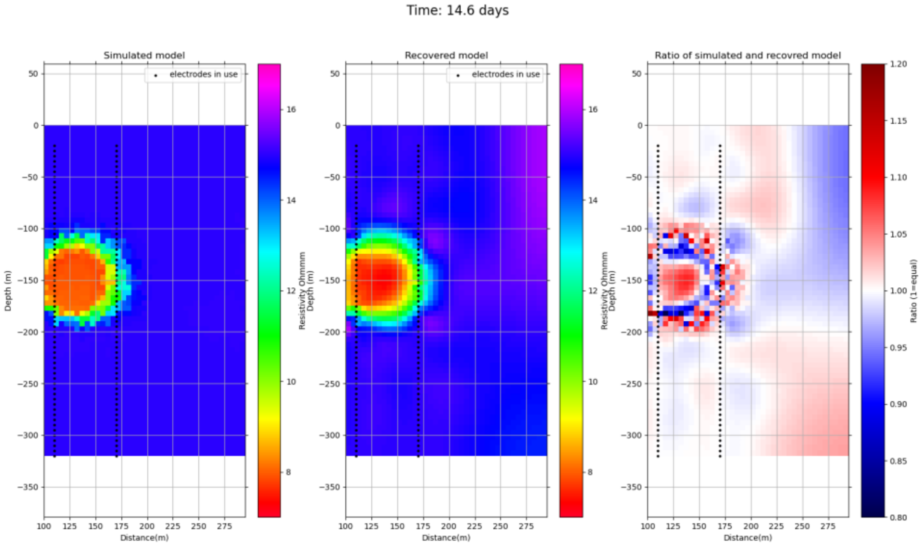

Figure A14 Simulated, recovered model for case a.

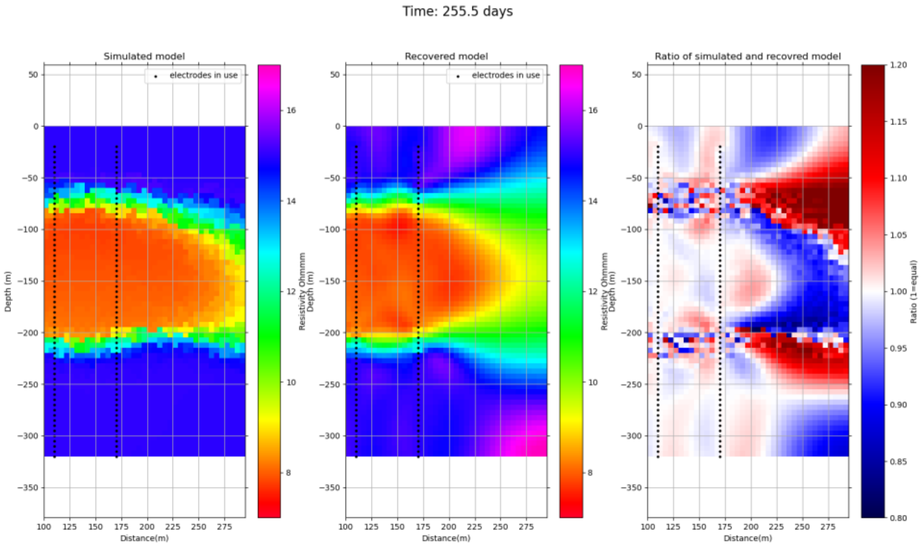

Figure A15 Simulated, recovered model for case a.

Case b

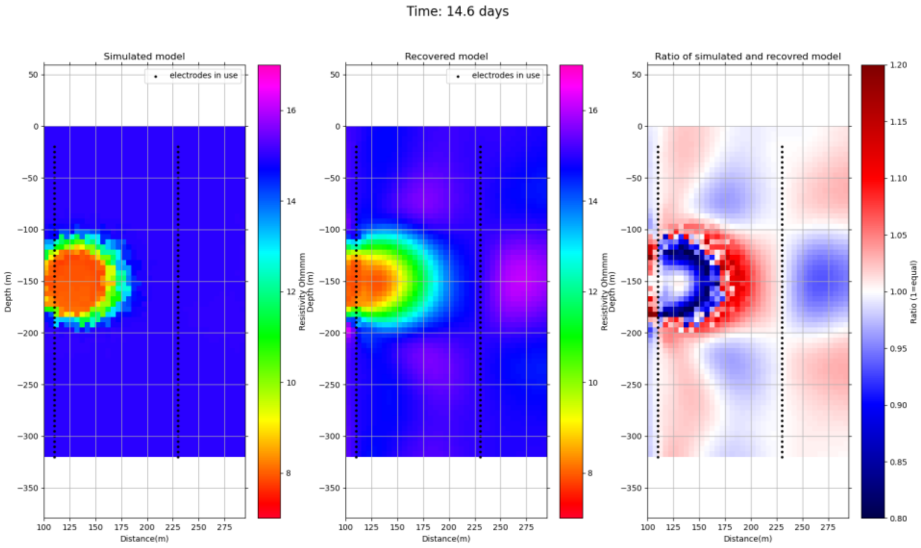

Figure A16 Simulated, recovered model for case b.

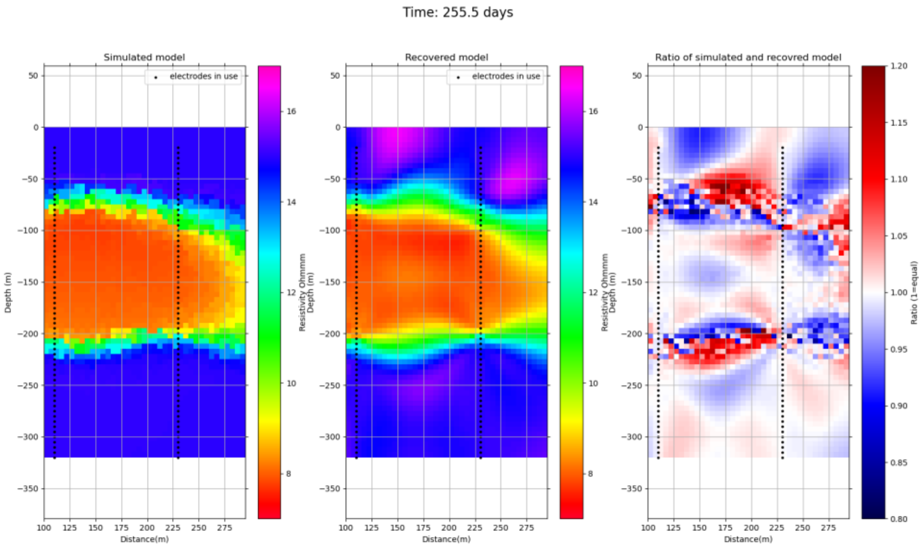

Figure A17 Simulated, recovered model for case b.

Case c

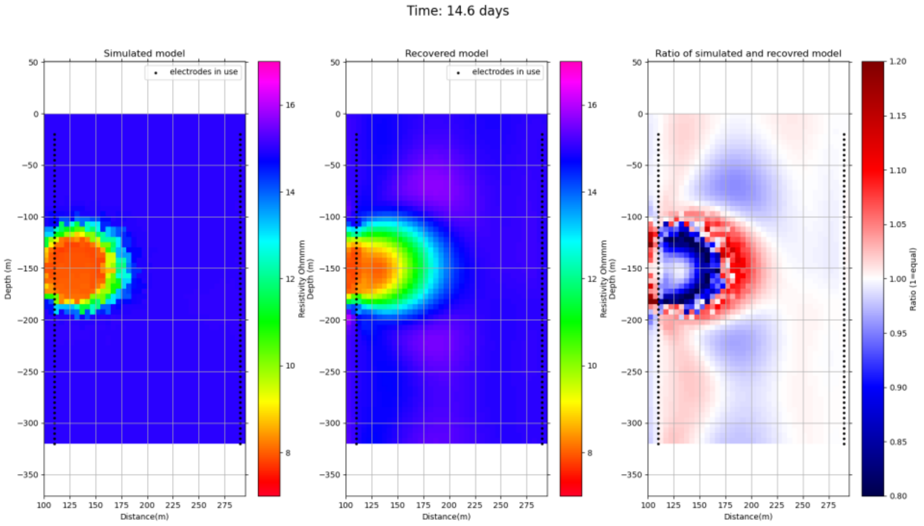

Figure A18 Simulated, recovered model for case c.

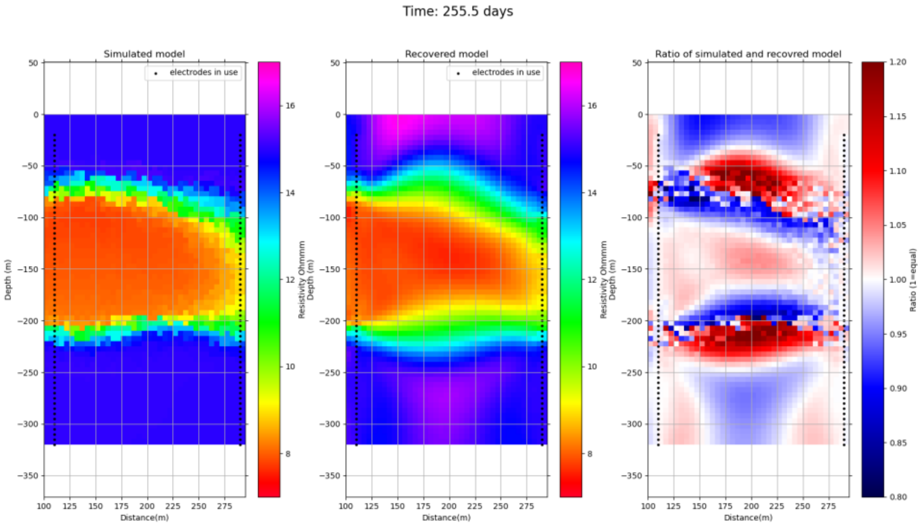

Figure A19 Simulated, recovered model for case c.

Case d

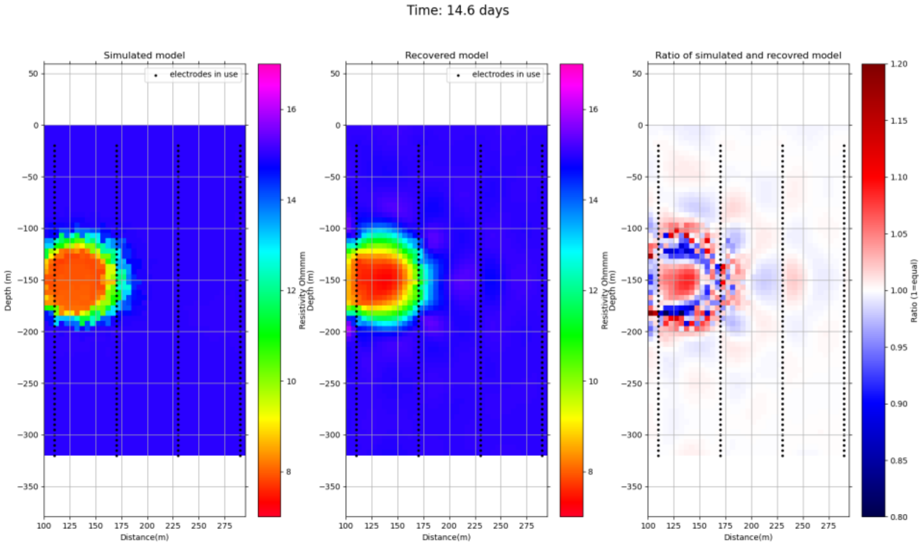

Figure A20 Simulated, recovered model for case d.

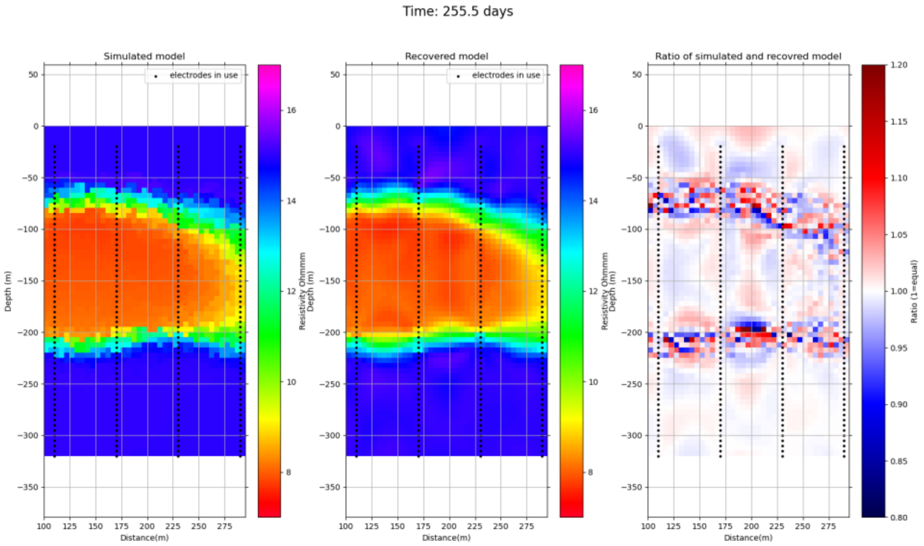

Figure A21 Simulated, recovered model for case d.

Conclusions from synthetic model

As expected, the distance between the boreholes plays an important role on the recovered resolution. For instance, we observe that for the 14.6 days of infiltration, we see a loss in resolution from case a to case c (with increased the distance of the boreholes). On the other hand, in case of 255 days infiltration, we observe the exact oppose phenomena, the resolution is decreased from case c toward case a. Of course, in the case d, where multiple boreholes are presents, we can mix and match from early and late infiltration very accurately.

Thus, the design and number of boreholes to be utilized on field applications, should be considered combined to the desired resolution. Yet, for a distance of 200 meters between the injection and production well, 2-3 boreholes are sufficient.

A5.2 Laboratory results

As mentioned, the ratio that the resistivity changes, is (among others) depending on the temperature change. If we assume that nothing else is changing in our model (since it is a lab enclosed tank) we can relate all the changes to the temperature change. Yet it should be mentioned here that we have the hypothesis that during the experiment compaction or particle transport has taken place. The hypothesis is based on the increase of the resistivity that can be explained by a decrease in porosity. The increase of the temperature will give a decrease in resistivity. At early monitoring times we do see an increased resistivity along the center of the y-axis which is the location of the injection well, see Figure A22. In this figure, the left panel shows the resistivity change based on the ERT measurements and the right panel shows the temperature changes as obtained by the interpolation of the DTS data.

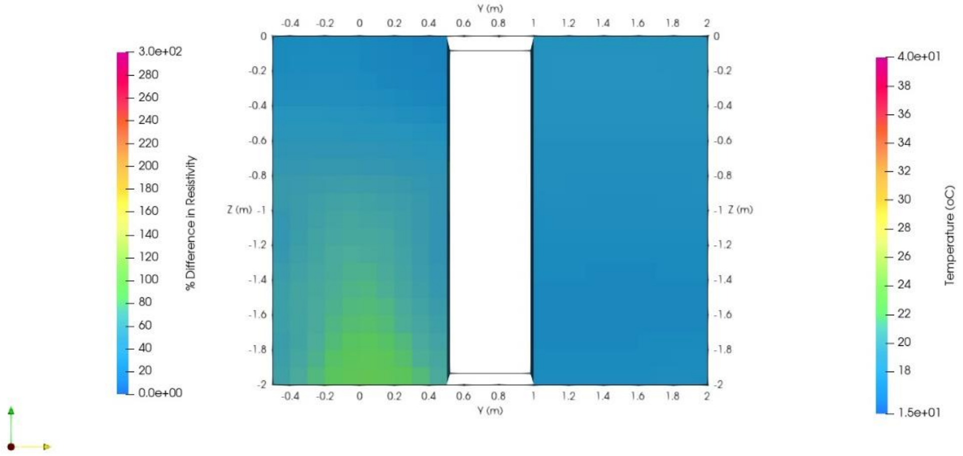

Figure A22 Change in resistivity (left) at an early monitoring time of the experiment and interpolated temperature (right) from the DTS data.

Figure A23 shows on top left panel the resistivity value changed well before that the DTS data (top right panel). This is due that DTS only senses the warm water when the water front is in contact with the fibre. The area in between the two boreholes is a simple interpolation.

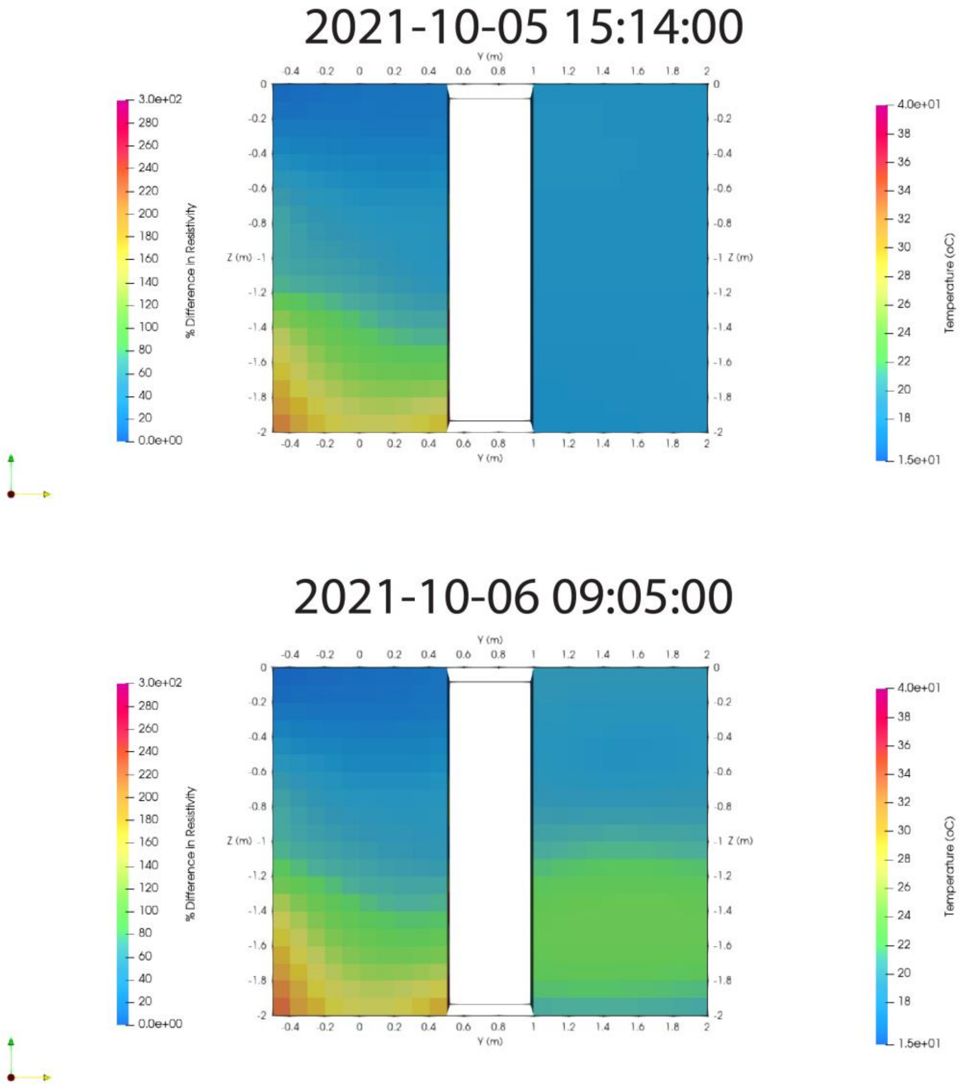

Figure A23 Snapshots of ERT model (left) and DTS interpolated data (right)

Figure A24 and Figure A25 shows similar results from later times. We observe that in the center part of the ERT model, a "valley" type of anomaly, with resistivity changes smaller than the surroundings. This is the area of the infiltration screen. The reason that this increased resistivity at later time is not the highest near the injection well, where flow velocity is the highest, may be due to the contradicting effect of the temperature increase there.

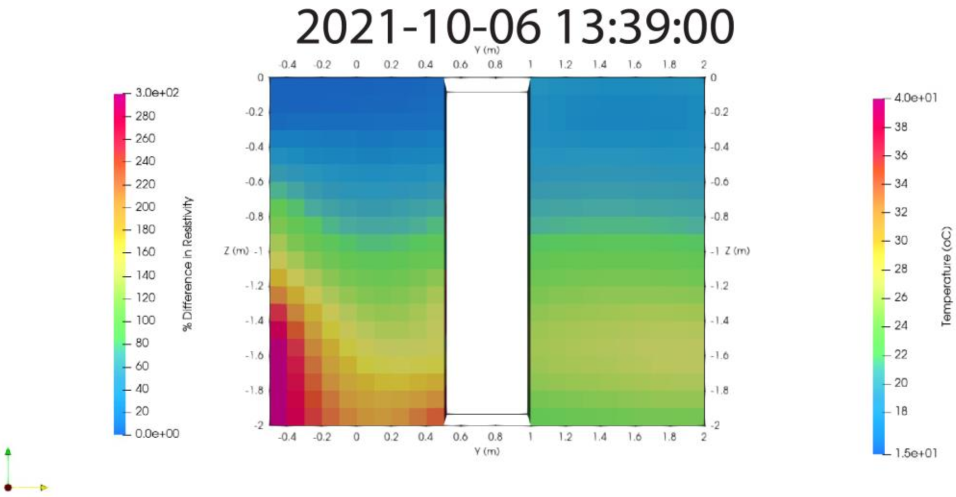

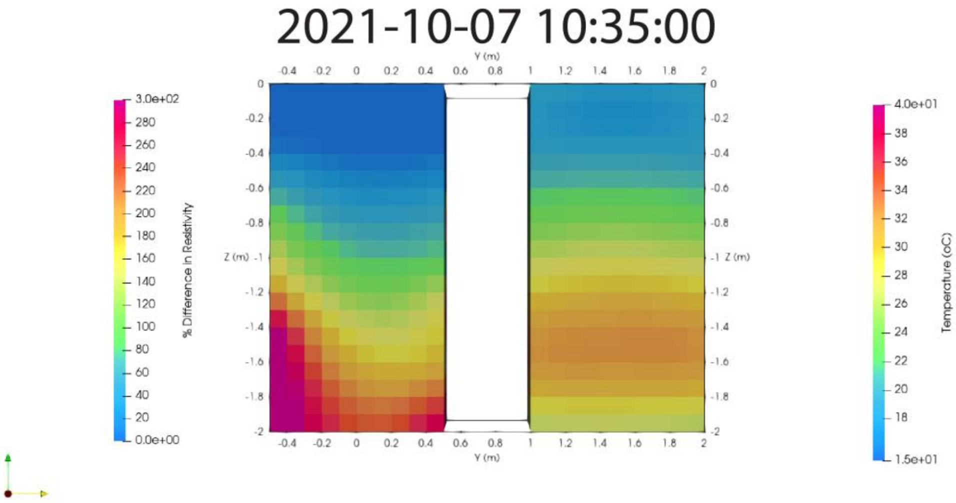

Figure A24 Snapshots of ERT model (left) and DTS interpolated data (right)

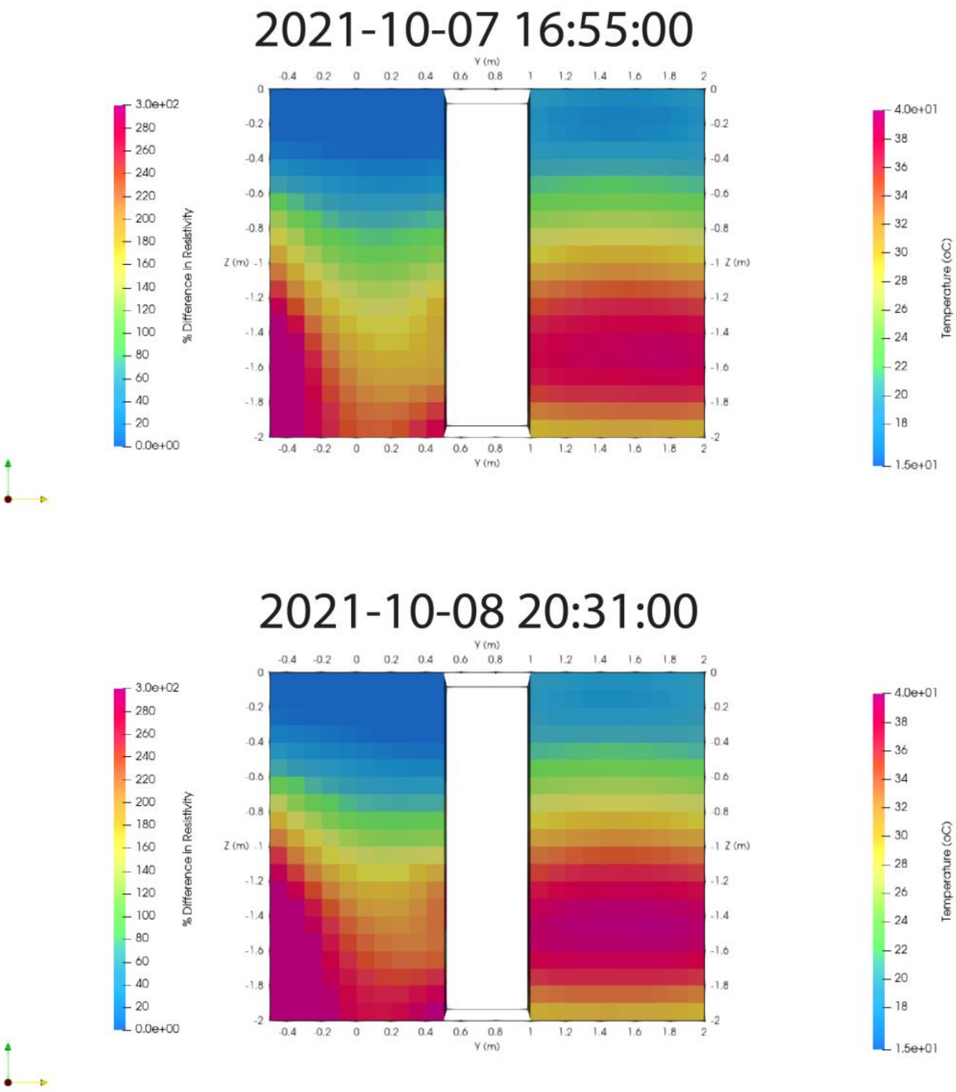

Figure A25 Snapshots of ERT model (left) and DTS interpolated data (right)

A6 Conclusions

In this work we presented the feasibility study of using ERT as a method to monitor the injection of warm water in a laboratory experiment. The data were validated with DTS measures. Unfortunately during the experiment another process occurred that also had an impact on the electrical resistivity near the injection well. Our hypothesis is that this process may be either compaction or particle transport. Therefore, we were not able to translate the ERT data into a temperature distribution. For practical applications of high temperature storage, we do not expect compaction to occur, and particle transport will likely to be limited by the direct surroundings of the production well. Therefore, we recommend applying the ERT measurements in a real field application and also combine it with information from a heat transport model.

The synthetical situations showed that if there is sufficient a-priori knowledge about an area, then we can calculate the monitoring set-up needed to successfully monitor the injection of warm water.

The conversion of resistivity change to temperature is based on some empirical relations and needs improving.

Appendix B: Acoustic cross-well tomography; detailed description

B1 Introduction

The Dutch government pursues a rigorous climate policy to achieve the objectives of the Paris climate agreement. Surface water and groundwater are key sources of heating, cooling, and the thermal energy storage systems. Borehole Geophysics and, in particular, acoustic cross-well tomography (ACT) offers the opportunity to monitor the geothermal processes in relation to temperature variations inside the storage system. The temperatures changes can modify the elastic properties of the solid media around the well, which can be captured via traditional acoustic surveys (Makky S Jaya et al., 2010; Nalonnil, Marion, & Engineering, 2012; Schön, 2011). A method that monitors the elastic properties in wells at a very high spatial resolution is the distributed acoustic sensing (DAS) survey system (Chang & Nakata, 2022). However, the implementation of DAS to monitor the variation of elastic properties due to temperature variation in geothermal wells should be further investigated.

In this project, we perform a modelling to assess the reliability of ACT for mapping velocity changes induced by warm water at similar temperature conditions of high temperature storage wells. For the modelling we consider a soil media that consist of sandy and saturated homogenous soil of 330 depth, which is subjected to P-wave velocity (Vp) changes at localized depths which are associated to temperature variations in a range of 30 and 90 °C. We also assume a separation between receiver and source of 175 m. The aim of the modelling is to determine to what extent the ACT technique can effectively distinguish, potential velocity variation for various P-wave velocity contrasts occurring within the receiver and shots positions.

In order to investigate the potential of DAS for performing an ATC survey, we carried out a laboratory experiment that consists of monitoring the effect of warm water of various temperatures that is injected in partially saturated sands. The laboratory experiment consists of a cross-well set-up that is assembled using fibre optics cable wrapped around a 4-PVC poles. Shot-gathers are generated by using an impulsive P-wave source creating energetic compressional or P-waves trends. The measured first breaks (P-waves) are then utilized to calculated P-wave cross-sections via tomographic inversion. The measurements are performed in a time-lapse fashion, so the velocity differences respect to the initial conditions can be determined.

Besides DAS measurements, simultaneous ERT, and DTS measurements were carried out at very similar time instants. ERT will monitor changes in resistivity after injecting warm water. The DTS measurements will provide information on the evolution of temperature with time inside the partially saturated sand layering inside the 4-poles array. Both resistivity and temperature information was utilized to interpret the changes observed in the measured Vp. The measured Vp was compared to Vp values obtained via standard refraction measurements using 10 Hz vertical geophones. Detailed description of the ERT is given in appendix A.

B1.1 Goals and research question

The target of this project is to assess the reliability to of ACT to capture the velocity variations induced by temperature variations in a high temperature storage system. In addition, we aim at evaluating the potential of DAS to monitor P-wave velocity changes due to injected warm water at conditions that are like a high temperature storage well.
Thus, the goals of the project are:

ACT Modelling:

- To evaluate the sensitivity of the ACT method to velocity variations induced by temperature changes.
- To evaluate the effect of large shot-receivers separation in an ATC survey to capture the small velocity variations in high temperature storage well.
- To determine the acquisition parameters and geometry of an ACT survey according to the most typical temperature variations.

DAS Lab experiment:

- To determine if DAS can retrieve the local P-wave velocities in ACT set-up.
- To determine if DAS is sensitive to velocity variations induced by temperature changes.
- To evaluate if the Vp changes determined via DAS-ATC correlate with other geophysical methods.

B1.2 Structure of the appendix

This appendix is comprised by the following chapters:

Chapter 1 contains an introduction that includes the main scope and main objectives of the project for the modelling and laboratory experiment.

Chapter 2 provides a theoretical description of the cross-well method. It covers a summary of the correlations (available in the literature) between Vp, temperature, thermal conductivity, and porosity for sandy saturated soils.

Chapter 3 presents the modelling and DAS laboratory set-up description including the fibre optics array, acquisition parameters, and survey schedule. The chapter also includes a brief description of the reference data utilized to validate the Vp recorded from travel times measured with DAS. It also describes the processing scheme adopted for synthetic (modelling) and laboratory data.

Chapter 4 presents the modelling results for the 2 scenarios and 6 cases of velocity variations. It described the results of the laboratory experiment including the typical P-wave velocity range obtained through travel time inversion. It describes the reference Vp values obtained after inverting travel times from a reference refraction seismic set-up. It shows the Vp differences as a function of temperature variations. Finally, it proposes a correlation between temperature Vp differences where temperature utilizing a clustering procedure.

Chapter 5 provides a discussion of the relevance of the main findings of the experiment and to what extent this can be reproduced in a field scale set-up.

Finally, chapter 6 and 7 provides conclusions and recommendations.

B2 Methods

B2.1 Acoustic cross-well tomography

Acoustic cross-well tomography (ACT) method uses travel times typically recovered from a two-neighbors borehole set-up. One of the boreholes is equipped with a set of geophones which recovers signals generated by a source located in neighbor well. The recorded travel times from various shots at different depths are utilized to retrieve the P-wave and/or S-wave velocity structure between the two wells. Acoustic cross-well survey originally developed in oil industry applications, is regarded as very reliable and high-resolution tomography (Justice et al., 1993; Justice et al., 1992; Justice et al., 1989; Liu, 1999). The field set-up consists of two vertical boreholes separated at a distance L (Figure B1). One of the boreholes is utilized to install an acoustic source (which is moved at various depths) which generates acoustic waves which are recorded by an array of single or multi-component receivers localized at the neighbor borehole.

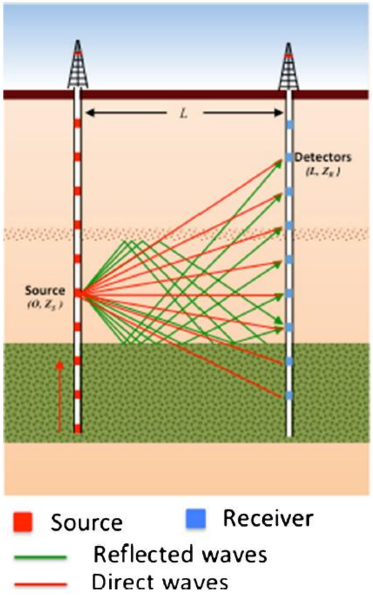

Figure B1. Schematic diagram of a cross-well seismic survey. The geometry consists of many source points (red) and many receiver points (blue). Source and receiver wells are separated by a distance, L meters. (Raji, Gao, & Harris, 2017)

A very important aspect in the ACT survey is the vertical resolution. The receiver separation determines the minimum wavelength that can be recorded. The minimum wavelength is determined by the maximum frequency and the minimum existing velocity inside the array. Thus, the vertical resolution is determined as 1/4 of the minimum measured wavelength. Therefore, for a saturated media a minimum Vp of e.g. 3000 m/s and a maximum frequency of 1000 Hz gives a minimum wavelength of 3.0 m, which provides a resolution of 0.75 m. This would be the minimum thickness that can be measured. This indicate that for designing a survey set-up it is necessary to have some prior knowledge of the local velocity, so the source type and receiver configuration can be effectively selected depending on the target resolution. Another aspect to consider is the source-to-receiver distance. The longer the source-to-receiver separation the more attenuation the data will have, the less accurate the travel time estimation.

B2.2 Effect of temperature in elastic soil properties

Thermal conductivity

In this section we stress the importance of understanding the effect of the temperature in the compressional velocity. The existing literature broadly discuss the relation between the temperature in relation to elastic properties such as Vp, Vs, density (Hartmann, Rath, Clauser, & Sciences, 2005; Makky Sandra Jaya et al., 2010; Jones, Murphy, & Nur, 1980; Schön, 2011). The natural connection between the elastic properties and temperature is by means of the thermal conductivity. Some of the conditioning factors to increase the thermal conductivity are decreasing porosity and water content. Schon (2011), presents (Figure B2) the relation between rock/soil porosity for various type of materials including sandstone and sands in saturated conditions. It is clear that thermal conductivity decreases as the porosity increases for both sands and sandstones formations.

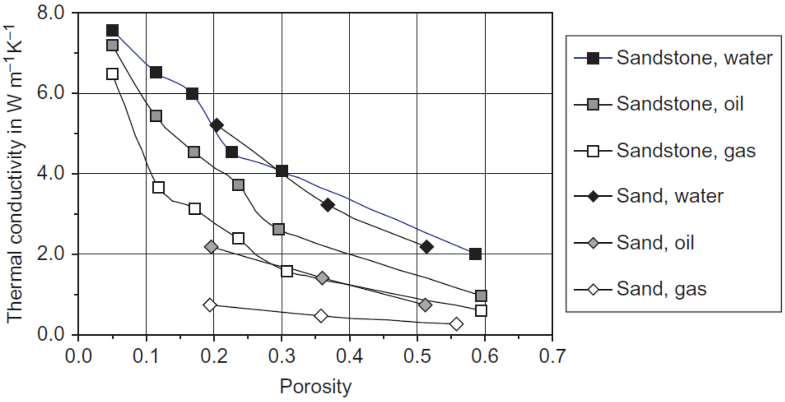

Figure B2 Thermal conductivity versus porosity sand and sandstone at different pore fluids. (Schön, 2011)

The correlation between thermal conductivity as a function of pressure and temperature are presented in Figure B3. The plots described focus on sedimentary rock conditions. The thermal conductivity appears to be almost constant with pressure, while it appears to decrease with temperature.

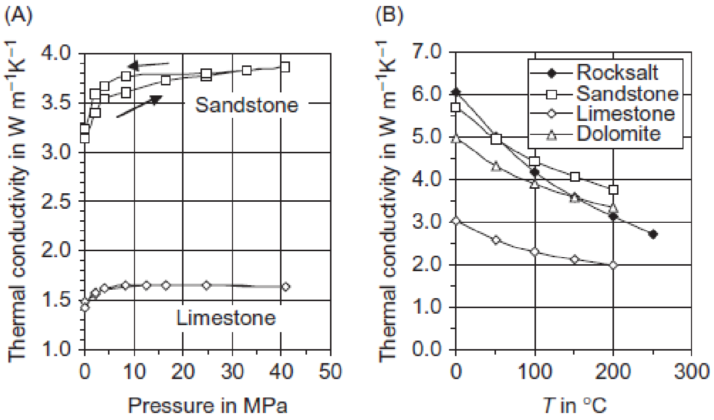

Figure B3 Thermal conductivity as a function of pressure and temperature (sedimentary rocks). (A) Thermal conductivity versus uniaxial pressure. (B) Thermal conductivity versus temperature.

The formulations that describe the correlation of P-wave velocity, porosity, and density are described in the following section.

Velocity – temperature correlation

Generic formulation

In this section we seek to determine the connection between Vp and temperature, thus the effect of temperature changes in the geological formation of the high temperature storage wells can be characterized. The density, viscosity and P-wave velocity of water each vary in a seemingly unrelated manner with respect to temperature, at a constant pore fluid pressure (Makky Sandra Jaya et al., 2010).

$$\boldsymbol{K_{sat}} = \boldsymbol{k_{dry}} + \propto^2 \boldsymbol{M}$$ *Equation 0-1*

$$M = \frac{K_g}{(1-K_{dry}/K_g)-\emptyset(1-K_g/K_f)}$$ *Equation 0-2*

$$\mu_{sat} = \mu_{dry}$$ *Equation 0-3*

Where $\propto = 1 - K_{dry}/K_g$ is the Biot-Willies coefficient, $\emptyset$ is the porosity, K_g and K_f are the bulk moduli of the solid grain material and fluid. The Gassmann equation is normally utilized to represent the dependency of temperature of the fluid on the bulk modulus. Thus, the formulation is as follows:

$$\boldsymbol{K_f} = \boldsymbol{\rho}(\boldsymbol{T})[\boldsymbol{v}(\boldsymbol{T})]^2$$ *Equation 0-4*

Where ρ, and v are the fluid density and velocity as a function temperature, T, respectively.

Sandy soils

Elastic properties of saturated sediments can be expressed as function of thermal conductivity (Hamdhan & Clarke, 2010; Hartmann et al., 2005; Schön, 2011). Hartmann et.al. (2005) formulated an empirical equation for thermal conductivity of saturated sandy sediments (λ_{sat}) as a function of P-wave velocity (V_p), density (ρ), and porosity (ϕ).

$$\boldsymbol{\lambda_{sat} = (1.07 \pm 0.27) + (0.239 \pm 0.002)V_p + (0.504 \pm 0.053)\rho + (0.042 \pm 0.02)\phi} \quad \text{Equation 0-5}$$

Thermal conductivity λ_{sat} is in units of $Wm^{-1}K^{-1}$, density ρ in units of $g\ cm^{-3}$, and P-wave velocity V_p is in units of $km\ s^{-1}$.

Thus, for sedimentary rocks the thermal conductivity can be expressed in function of temperature as follows:

$$\boldsymbol{\lambda(T) = \frac{\lambda_0}{a_1 + T(a_2 - a_3/\lambda_0)}} \quad \text{Equation 0-6}$$

Where the empirical constants are:

$a_1 = 0.960\ with\ standard\ deviation = 0.011$
$a_2 = 0.007\ with\ standard\ deviation = 0.001$
$a_3 = 0.014\ with\ standard\ deviation = 0.003$

λ_0 is the thermal conductivity at 25^oC. Thermal conductivity at ambient temperature, can be expressed in terms of porosity.

$$\boldsymbol{\lambda_0 = a_2 - b_2\phi} \quad \text{Equation 0-7}$$

Finally, with the following expression:

$$\boldsymbol{V_p = \frac{\lambda_{sat} - (1.07 \pm 0.27) - (0.504 \pm 0.053)\rho - (0.042 \pm 0.02)\phi}{(0.239 \pm 0.002)}} \quad \text{Equation 0-8}$$

Equation 0-8 can be used to estimate the compressional velocity ($\boldsymbol{V_p}$) as a function of thermal conductivity and hence from temperature. A graphical representation of the correlation between Vp, thermal conductivity, density and porosity for sandy sediments is presented in Figure B4 (Hartmann et al., 2005)

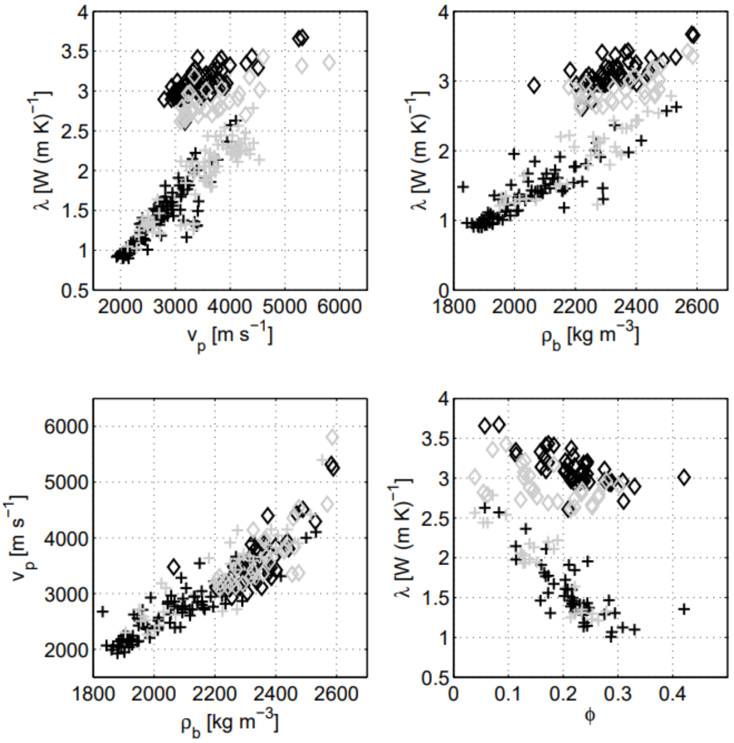

Figure B4 Correlation between Vp, thermal conductivity, density and porosity for both dry and saturated sand conditions. (Hartmann et al., 2005)

B3 Synthetic modelling and Laboratory experiment

B3.1 Cross-hole acoustic modelling

The cross-hole modelling is aimed at determining the sensitivity of the ACT to map the velocity variations induced by the increase temperature due to warm water injection. Figure B5 shows the modelled geometry where warm water induces temperatures that varies from 35 to 70 °C, which is based on the same synthetic simulation as was used in appendix A.

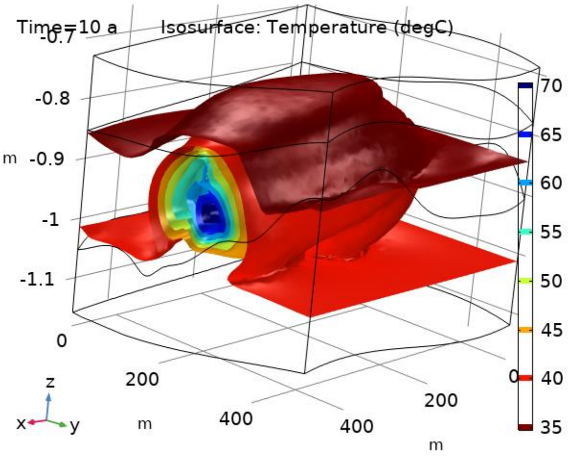

Figure B5 Modelled temperature distribution in a geothermal well.

We use the equations 2-5 to 2-8 to estimate velocity variation for 4 cases with temperature values ranging from 35 to 70 °C. Thus, for saturated sands with ρ = 2.1 $g\ cm^{-3}$, $\phi = 0.35$ and a temperature T range between 25^oC and 90^oC , the Vp varies as follows:

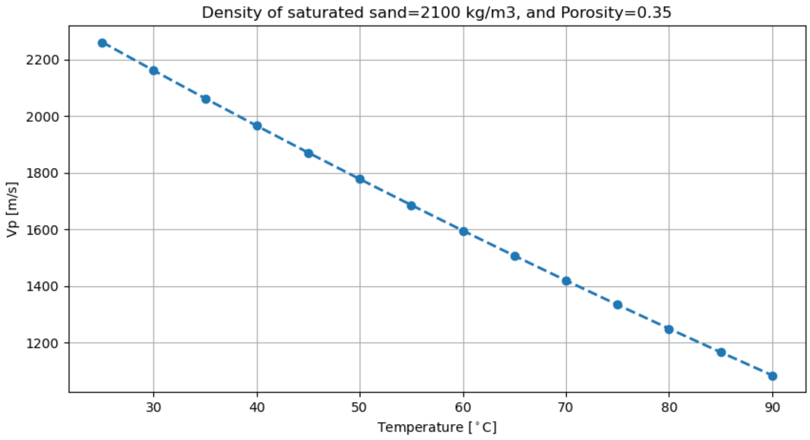

Figure B6 Estimated Vp variation for cold (25^oC) and warm (90^oC) water conditions. Computed from formulation.

From this temperature range the velocity can be reduced between 7% (30^oC) up to 53% (90^oC), respect to the cold-water condition.

Table B1 Elastic parameters for modelling ATC with initial temperature of 30 °C.

Case	Vp [m/s] –>T0=25 °C	Vp[m/s] anomaly	Temperature [°C]
I	2321	1420 (39%)	75
II	2321	1596 (31%)	65
III	2321	1778 (23.4%)	55
IV	2321	1966 (15.3%)	45
V	2321	2161 (6.9%)	35
VI	2321	2261 (2.6%)	30

The modelling is carried using pygimli. The survey configuration consists of 70 receivers at every 5 m covering around 300 m. For the modelling we built the mesh domain with embedded anomaly using the gmsh tool (Gmsh: a three-dimensional finite element mesh generator with built-in pre- and post-processing facilities).

We consider 2 scenarios, for small (14.6 days) and large (255.5 days anomaly) size anomaly (see also appendix A). The separation between receiver and shot position is of 175 m. This large separation constitutes the less favorable scenario (maximum shot – receivers string separation) and is the maximum distance at which the test could be successfully implemented.

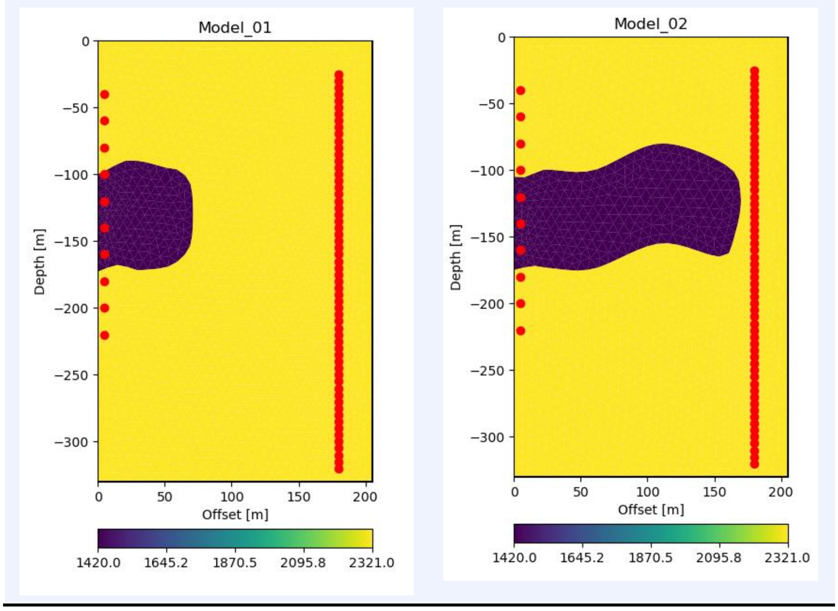

Figure B7 Modelling scenarios: left (14.6 days) and right (255.5 days) cases as described in Table B1, case IV.

The selection of the scenarios is based on the temperature distribution as simulated.

Processing framework

In this section we describe the processing scheme implemented for the acoustic modelling. We assess the accuracy of the ATC method varying the velocity difference between the background medium and the anomaly.

Thus, the processing workflow is as follows:

a) Forward modelling for each selected case to create synthetic travel times. For a more realistic assessment 1% of noise is added to all computed travel times.
b) Inverting synthetic data for 2 anomaly cases and for 4 combinations.
c) Compute mean velocity as a function of depth for all inverted models
d) Computed the difference in percent between true model and inverted model for all velocity combinations.
e) Plotting together the 6 cases for each scenario, so the minimum velocity difference that can be effectively mapped via ACT is determined.

The results obtained from the ATC modelling are described in section B4.1.

B3.2 Laboratory experiment

The lab experiment is aimed at testing the capabilities of DAS for detecting velocity changes, so it can be later utilized to perform ATC survey. Although the lab conditions does not necessarily recreate the actual soils conditions e.g. in-situ confining pressure, density, and degree of saturation, the changes induced by the injected warm water should be enough to capture the Vp variations. The acoustic measurements were carried out in the Geohal facilities at Deltares. The test site is comprised by partially saturated sands contained in a rectangular tank of 5.5 m x 7.0 m x 2.5 m. The survey set-up consists of 4 poles arrayed in a square shape of 1.0 m separation. In the middle of the square array there is an injection well where hot water is injected. In order to maintain the injected water circulating within the tank, an extraction well is localized at 5.8 m from the injection well. The same experiment was also applied for the ERT measurements in appendix A.

Figure B8 a) Overview of the test site with the DAS array, the injection and extraction wells, and b) Top view of 4-pole array for cross-hole test.

Cross-hole set-up

The DAS cross-hole set-up consists of 1300 m of single mode fiber optic cable of 2mm diameter which is wrapped around 4” diameter PVC poles (Figure B9). The effective measuring length along the pole is of ~2.2 m which for 1.0 m channel spacing, provides up to 251 measurement points per pole. The fiber optic cable was also used for DTS measurements and at four depths also some horizontal lines were installed, including some diagonal lines that pass near the injection well.

a) b)

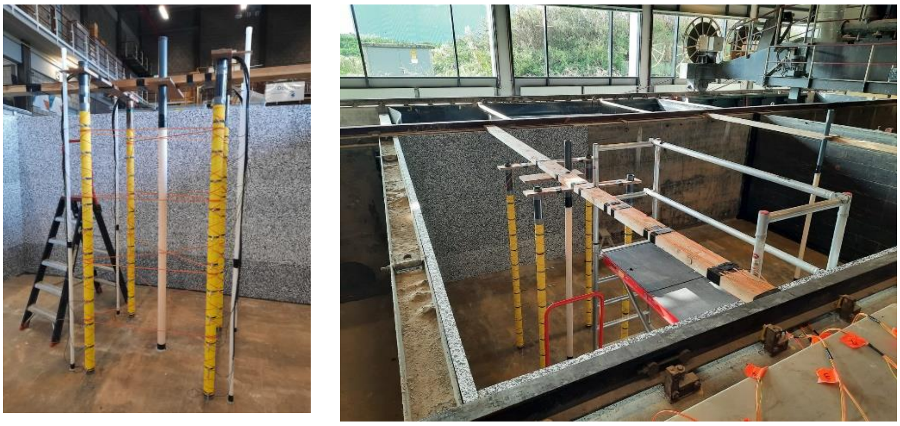

Figure B9 a) DAS array along 4 survey poles, and b) 4-poles array including injection (within the DAS array) and extraction (at the right end) wells; a) also shows horizontal diagonal fiber optic cables for validation with DTS measurements.

The acoustic source utilized was the SBS42 P-wave borehole sparkle system that is manufactured by http://geotomographie.de/. The SBS42 source delivers strong discharge that vaporizes water by a high-pressure plasma which expands and collapses, generating high-frequency seismic waves. The source is highly repeatable at frequencies up to 4-5 kHz.

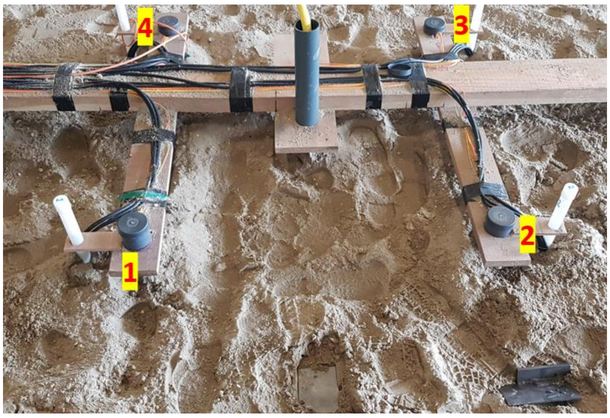

Figure B10 Lay-out of 4-pole array for cross-hole surveying. Name assigned to each survey pole is indicated by red color numbers.

The source was placed inside pole 3, so acoustic signals could be simultaneously recorded by poles 1, 2, and 4 (see configuration in Figure B10). For the measurements the borehole source was placed at 5 depth locations (with 0.4 m of vertical offset), namely, 0.6 m, 1.0 m, 1.40 m, 1.80 m, 2.2 m. At each depth location up to 5 individual shots were recorded. The cross-hole measurements at all 5 locations were repeated up to 21 times distributed along 4 days of measurements (see appendix B-A). The measurements were performed at different temperature conditions, so the effect of hot-water in the acoustic wavefield could captured. Notice that the measurements were performed after the warm water was injected, so no noise coming from water pumping was present in the records.

DAS Acquisition parameters

The DAS measurements were performed utilizing an iDAS interrogator version 02, manufactured by Silixa. To cover high frequencies, the sampling frequency utilized was 50 kHz. The duration of each record was set to 5 seconds. The channel spacing assigned to the iDAS interrogator was of 1.0 m.

The time table of the measurements performed between 05-10-2021 and 08-10-2021 is provided in appendix B-A.

Reference geophone measuring parameters

In order to somehow validate the Vp values determined from inverted DAS travel times, we performed reference measurements on top of the sand layering to measure the overall Vp after warm water was injected. We placed a 6 m linear geophone array of 10 Hz, 24 vertical receivers, separated at 0.25 m. Measurements are recorded using hammer impact at several positions utilizing a refraction seismic acquisition scheme. The sampling frequency was set to 16 kHz or 62.5 micro-seconds. The 10 Hz geophones should provide energy of frequencies from 10 Hz up to 250 Hz before sporous amplitudes become visible (Hearn, Strong, & Kinmont, 2019). In partially saturated sands (degree of saturation below 90 %) Vp should be below 1500 m/s which is typical values for fully saturated conditions (Tamura, Tokimatsu, Abe, Sato, & foundations, 2002).

Figure B11: Geophone array to obtain reference Vp inside the partially saturated sand layering.

Thus, at a maximum Vp of 1500 m/s and maximum frequency of 250 Hz provide wavelengths almost equivalent to the length of the linear array of 6.0 m. Thus, Vp slower than 1500 m/s should be visible by the geophone array.

Processing framework

The recorded DAS data is processed as follows:

a) Data pre-processing

The DAS records consists of individual traces at every 1.0 m which provides up to 250 measurements points. In order to account for the 10.0 m wavelength, the records are downsampled down to 25 traces distributed along 2.2 m.

b) First arrival picking/travel times

The 25 traces records are converted to seg2 format so the first break picking is carried out manually utilizing *pickwin* tool from SeisImager2D software. The picking is made using 5 shots from which the mean travel times is calculated.

c) 3D inversion

The inversion is performed in 3D utilizing pygimli inversion tool (https://www.pygimli.org/.). The inversion carried out utilizing the mean travel times from 75 traces distributed in poles: 1, 2, and 4.

The computed cross-sections are exported to VTK format to be post-processed. Notice that the inversion is carried out utilizing travel times obtained from individual shot positions.

d) Time-lapse

All exported VTK files are used to compute the velocity difference between consecutive measurements. The velocity difference are plotted together with reference temperature DTS data in a time-lapse fashion so the effect of temperature changes in the velocity media can be analyzed.

e) Vp – Temperature correlation

Finally, we implement DBSCAN clustering method to correlate Vp differences and temperature in a common spatial domain. This result should help to determine at which temperature the velocity changes respect to the initial condition occurs.

B4 Results

B4.1 Modelling results

The modelling is based on 2 scenarios and 6 cases as described in section B3.1. The modelled anomalies are plotted together with its corresponding temperature value. Figure B12 depicts the 6 selected cases for the first scenario. It appears that the anomaly starts to be visible when the temperature reaches 35 °C or higher. Thus, the difference between the anomaly and the surrounding media should have a difference not less than 10% so the anomaly starts to become visible.

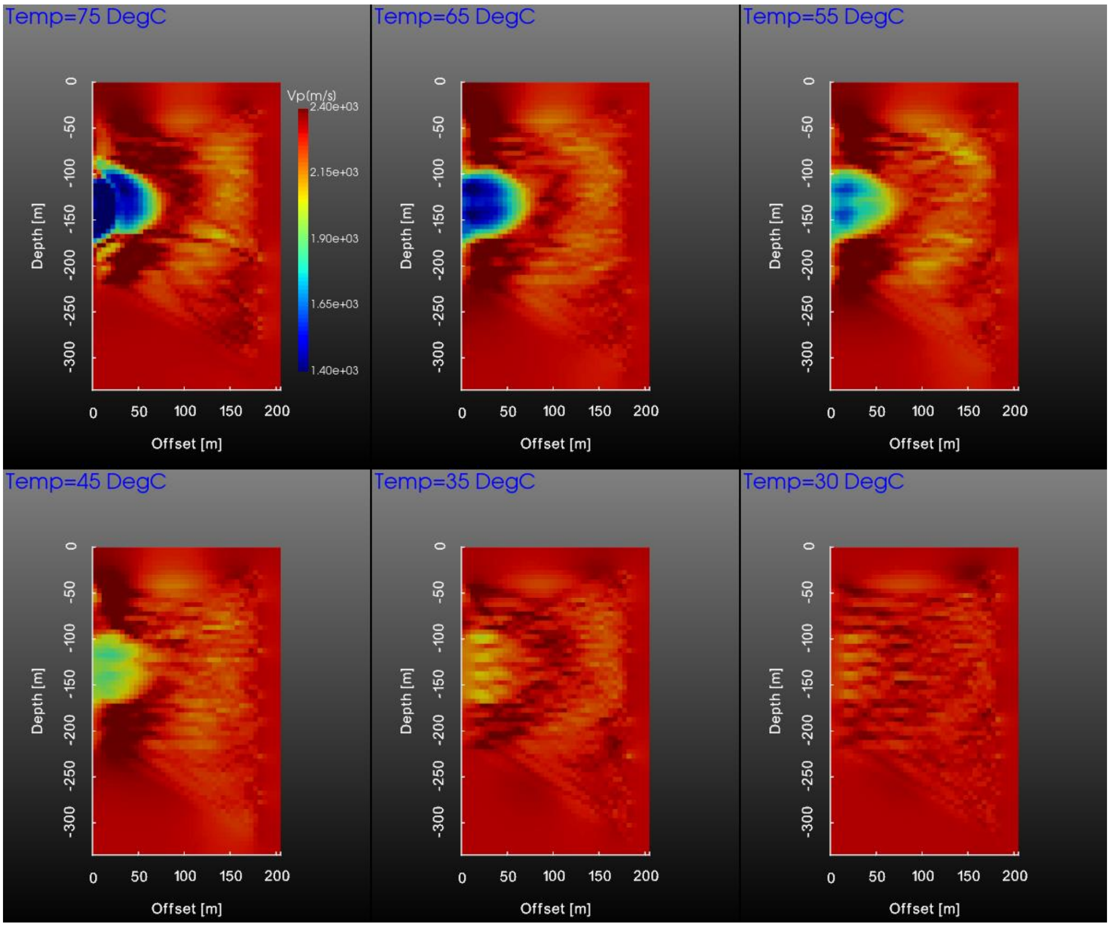

Figure B12 Inverted Vp models for various temperature conditions for scenario I (14.5). Case I (75 °C), Case II (65 °C), Case III (55 °C), Case IV (45 °C), Case V (35 °C), Case VI (30 °C)

The same analysis was performed for the second scenario where the simulated anomaly is further extended at the receiver position. Again, the selected array maps a clear distribution of the anomaly only when the temperature higher than 35 °C.

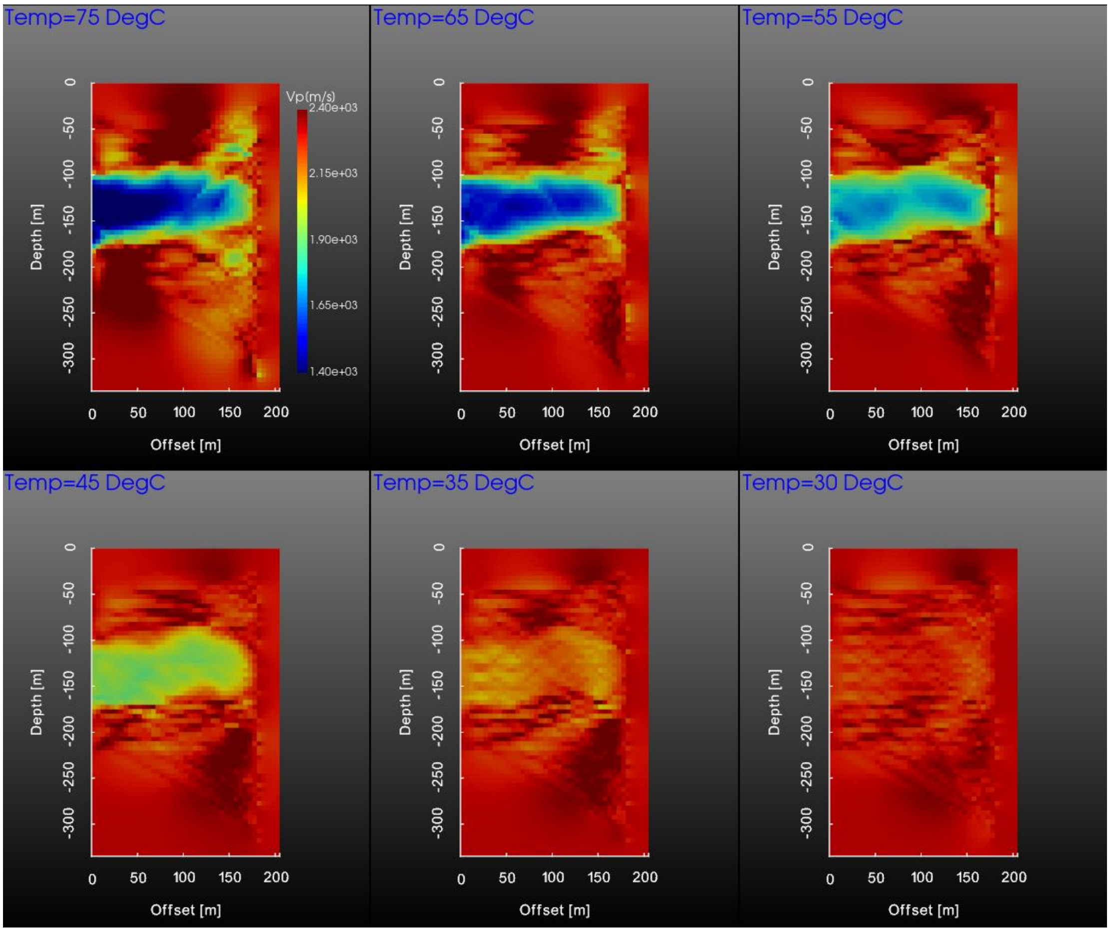

Figure B13 Inverted Vp models for various temperature conditions for scenario II (Day 255.5). Case I (75 °C), Case II (65 °C), Case III (55 °C), Case IV (45 °C), Case V (35 °C), Case VI (30 °C)

Conclusions

From the modelling results we can conclude that the selected ATC configuration, the method is capable to distinguish the velocity changes. The velocity changes are clearly observed at the early and later stage only when the temperature reaches 35 or higher. Thus, this indicate that the velocity difference between the geothermal anomaly and the surrounding media should be 10% or higher.

B4.2 Laboratory results

Recorded DAS signals

An example of a 75-traces (25 traces per pole) raw record is displayed in Figure B14. For the computation of the travel times, we used the first arrivals which are plotted as a function of depth. The time signals depict a visible first arrivals followed by a strong reflection from the bottom of the of the well.

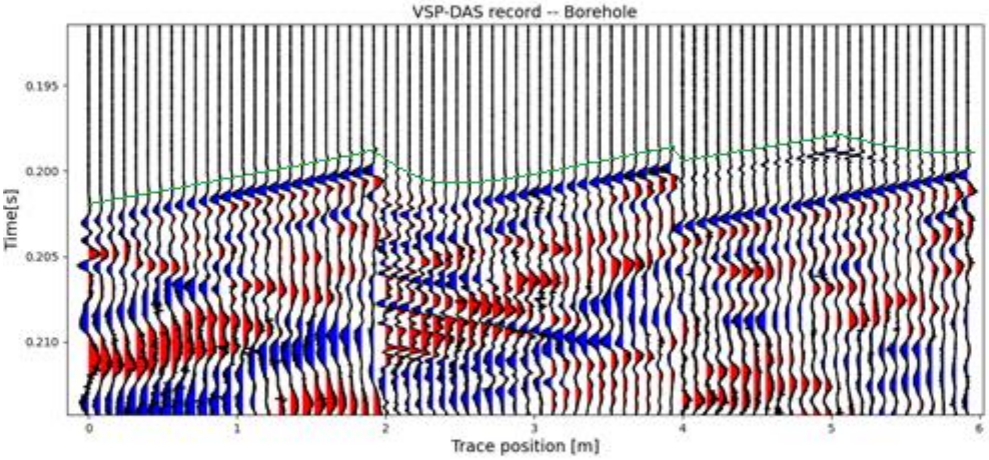

Figure B14: 75 traces shotgather recorded at poles 1,2,4 with source position in pole 3 at 1.4 m depth. The green line shows the first arrival time.

Travel times

The travel times are obtained by hand-picking the first arrivals of recorded 75-traces shotgathers. Figure B15 depicts average travel times (including standard deviation) computed with the source position down to 1.4 m depth. It appears that the slower travel times occur in pole 4. All poles show decremental behavior with depth from top down to 1.5 m.

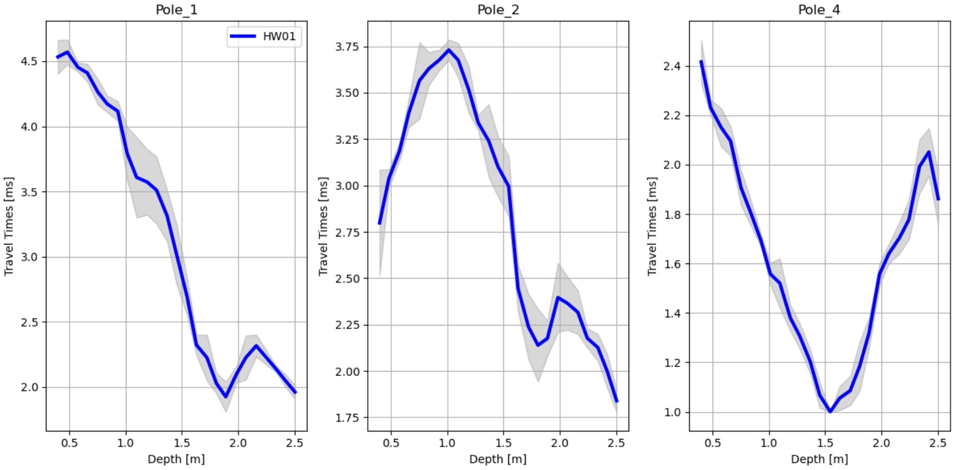

Figure B15: Computed mean travel times at poles 1,2, and 4 for a single instant.

Inverted borehole travel-times

The travel times recorded in poles 1, 2, and 4 are inverted simultaneously to construct 3D volume within the 4-pole set-up. Figure B16a depicts an example of inverted volume with the source position at 1.4 m depth coordinate. The computed velocities vary between 200 m/s to 1200 m/s.

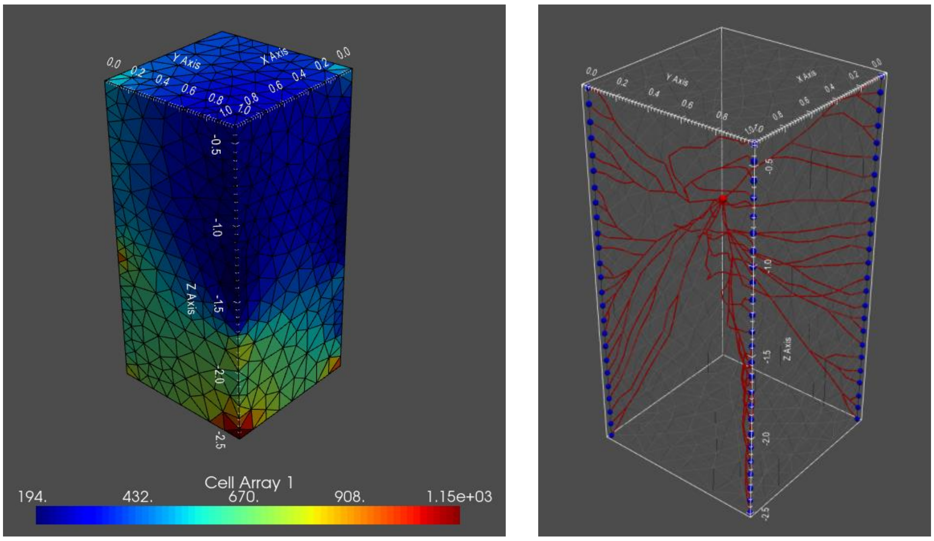

Figure B16: a) Inverted velocity volume and b) Raypath distribution.

Reference local velocity

Reference sledgehammer shots records were collected using 10 Hz geophones. A recorded hammer blow is shown is Figure B17. The first arrivals depict two well defined apparent velocities of 179 m/s and 542 m/s. The refracted travel times related to the Vp of 542 m/s for a cross-over distance indicates that depth of the high velocity refractor occurs at an approximate depth of 1.8 m from the surface. For a more complete analysis, the travel times measured at 5 shot positions were used to invert a 2D Vp section which provides information about the velocity structure during after introducing warm water. Examples of individual shotgathers together with picked travel times are displayed in appendix B-F.

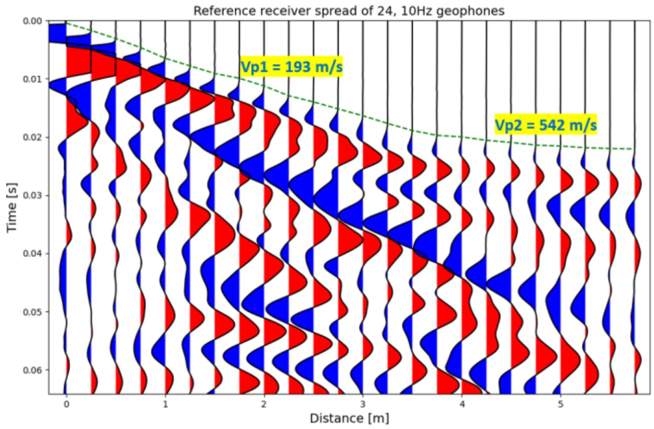

Figure B17: Hammer blow record using 24, 10 Hz vertical geophones.

Figure B18 shows the amplitude Fourier spectra along receiver position. The higher spectral amplitudes correspond to ground-roll of surface waves dominating the records. The P-wave propagates between 130 – 150 Hz along the whole survey length. Thus, the wavelength range falls between 1.3 m - 4.2 m proving a resolution between 0.33 m – 1.05 m.

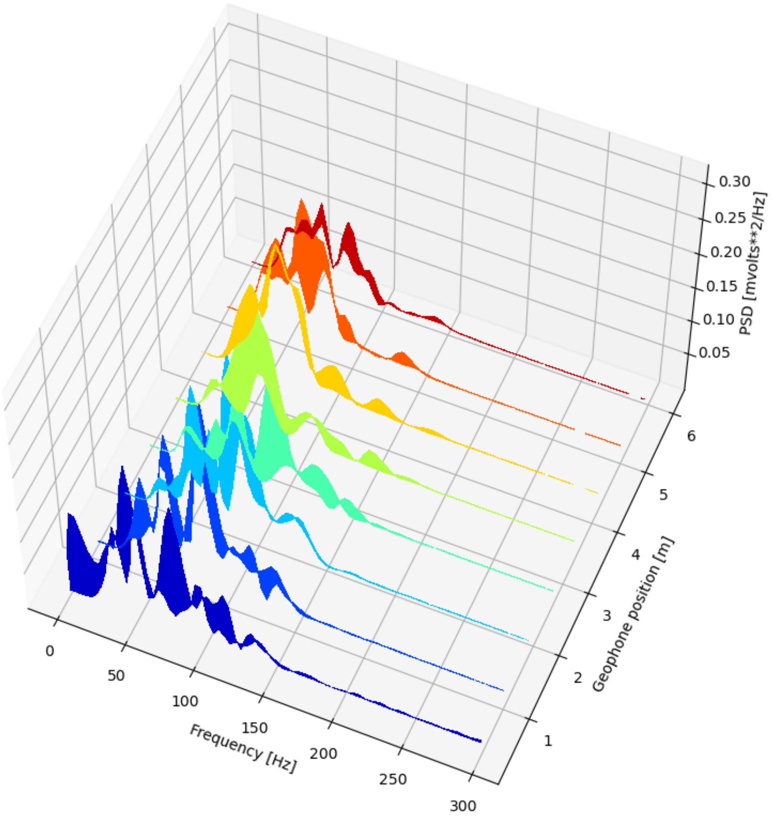

Figure B18: Frequency distribution along receiver position.

The mean travel times at all 5 positions provided a general overview of the Vp distribution along 24 geophones line (see Figure B11). Figure B19 shows that a predominance of Vp of ~ 200 m/s in the first 1.5 m, which increases up to 600 m/s at the lower part of the sand layering.

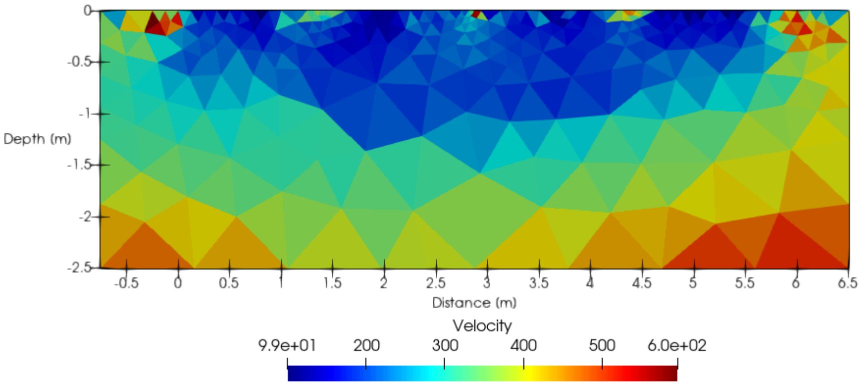

Figure B19: Inverted Vp using recorded travel times with 10 Hz geophones.

The low Vp velocity indicates that the sand layer was not fully saturated which causes that the propagating P-wave velocity decreases due to predominance of air bubbles between particles.

Temperature variation of injected warm water

Here we display the temperature variation along all measuring times. We plot together the measured temperature at pole positions and in the middle using the diagonal fibres. It is observed that the mean temperature at the middle of the volume is much higher compared to the one measured at the pole positions, which are below 30 °C.

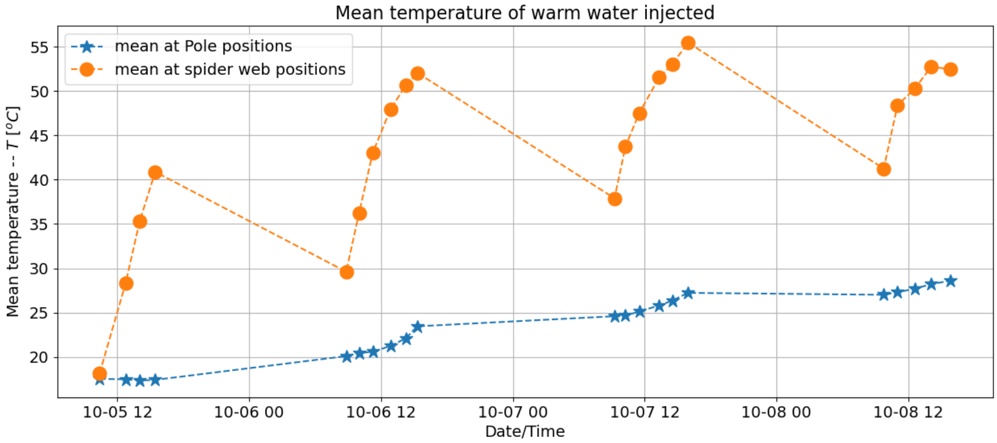

Figure B 20 Mean temperature measured at the pole and spider web (diagonal) fibres for selected time instants.

The temperature measured near the injection well appears to drop rather consistently at about 15 °C after the last measurements of each day. At the pole positions on the other hand, the remains almost constant. This is logical as the injection of hot water was stopped at the end of each working day.

Inverted P-wave velocity after warm water injection

The acoustic measurements were performed under different temperature conditions repeatedly during 4 days. Figure B21 shows 4 Vp scenarios with mean temperature of 18.0, 36.0, 47.0 and 52.0 °C. It is observed that there is a tendency of reducing Vp while increasing temperature of injected water. The mean temperature values indicated are average values from the DTS temperature measurements recorded near the injection well using a spiderweb configuration for the four depths as presented in detailed in Figure B9a.

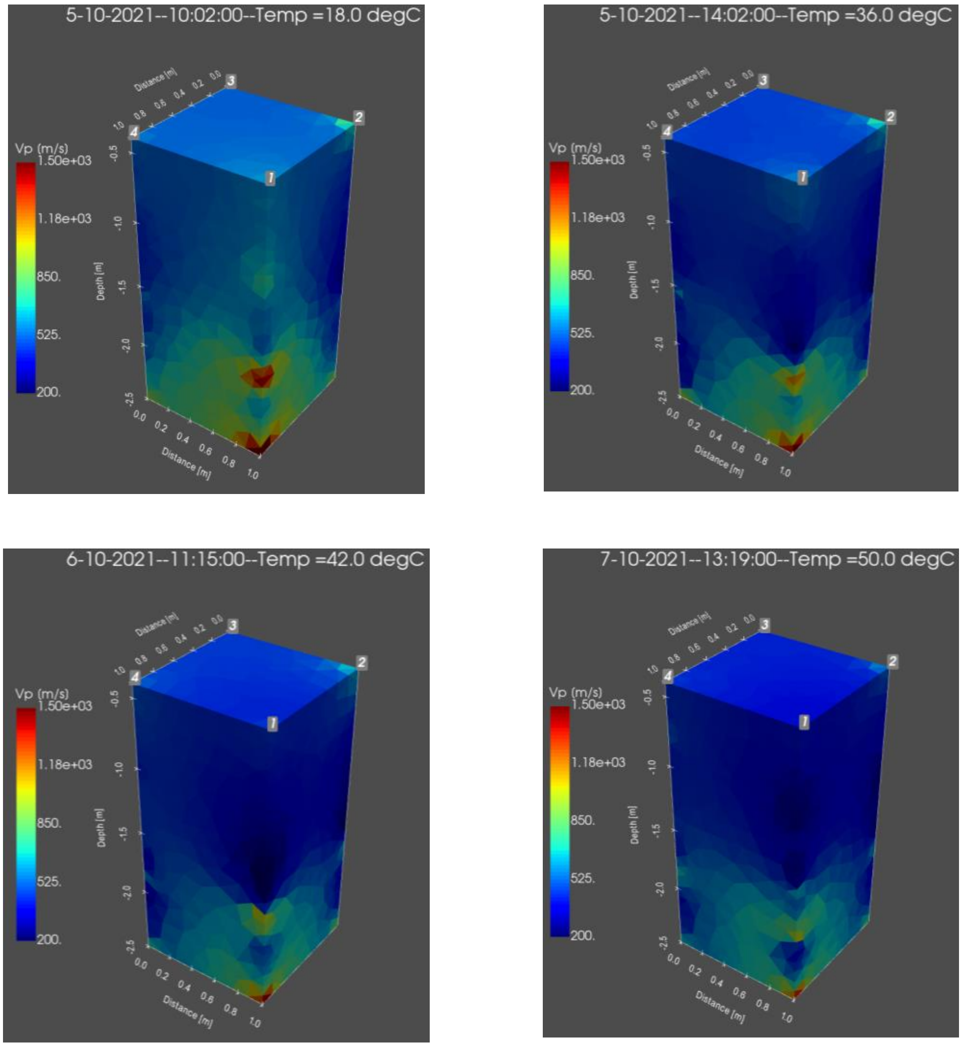

Figure B21: Vp distribution respect to time under different temperature conditions. The tomographic images are referred to the borehole source position at -1.8 m depth.

In Figure B22, we show the inverted Vp volumes for individual sources positions at -0.6 m, -1.0 m, -1.40 m, -1.8 m, and -2.2 m recorded at a common measuring time. In general, the Vp appears a similar velocity distribution except at source position at -2.2 m depth which depicts higher than the other 4 cases. It would be ideal to combine the 5 inverted images in Figure B22, as was done in the synthetic test. For this case we would need to filter out the noisy part of the results, which will be addressed in future research.

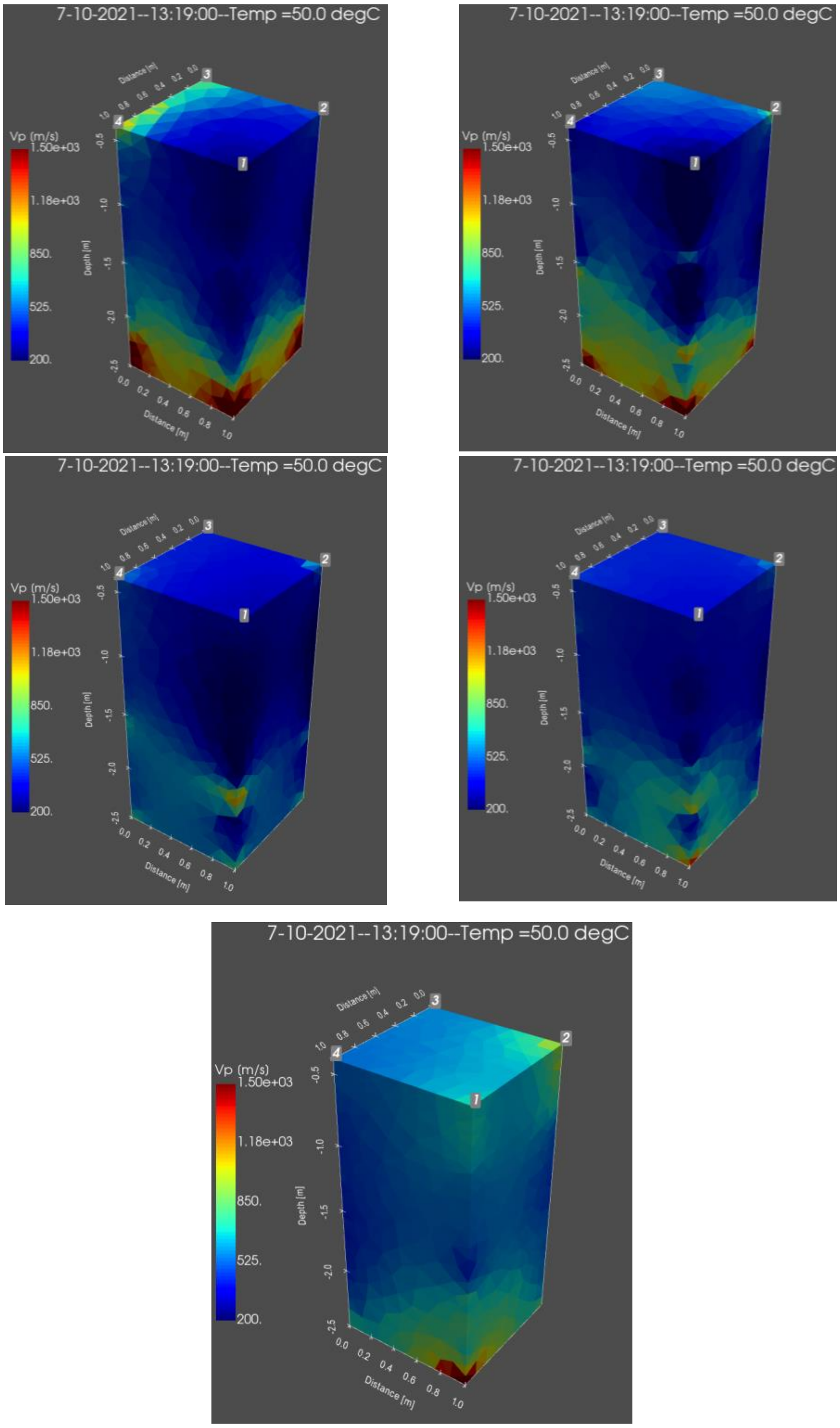

Figure B22: Inverted Vp per source position at -0.6 m, -1.0 m, -1.4 m, -1.8 m, and -2.2 m depth.

Velocity difference respect to initial condition

A more detailed analysis is made if plotting velocity different using slices of the same axis as the DTS cross-sections is displayed in Figure B23. The plots display the velocity difference between measurements performed on: 5-10-2021 – 14:02:00, 06-10-2021 – 11:15:00, and 07-10-2021 – 13:19:00 respect to the very initial condition. We can observe how Vp appears to be reduced while increasing the temperature in the middle and the lower part of the well. This behavior is also observed in other instants as shown in appendix B-C.

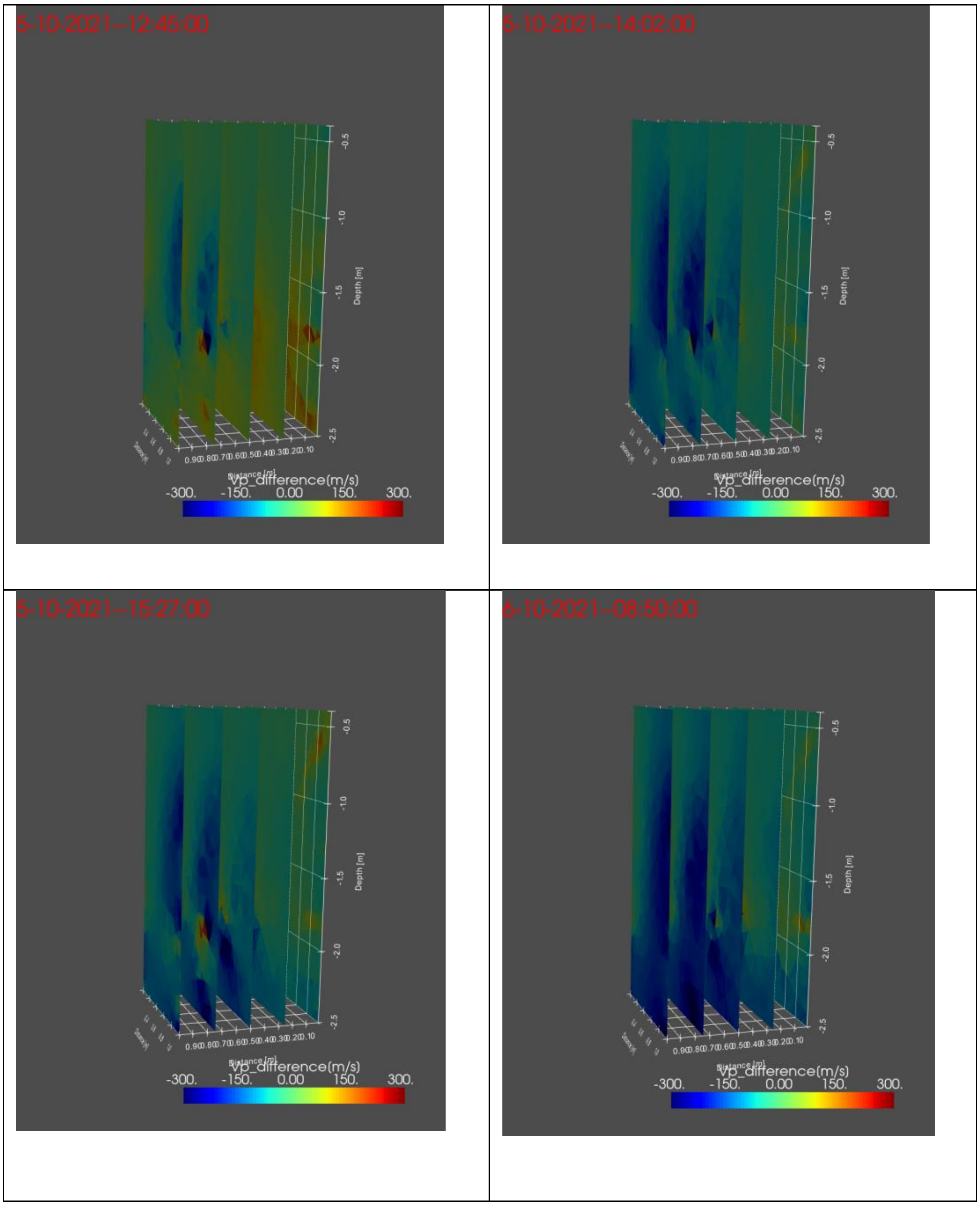

Figure B23: Vp differences respect to temperature for a single source position down to -1.8 m depth.

In Figure B24 the spatial averaged velocity difference (decrease) is plotted for various monitoring times together with spatial averaged DTS measurements: temperature in the 4 poles and the depth averaged temperature near the injection well (center of the spiderweb).

During the first day there is a clear correlation between the DTS measurements and the change in velocity. After 1 day there is a clear drop in the velocity difference that cannot be explained by the temperature distribution. Our hypothesis is that some compaction or escape of trapped gas has taken place in the tank resulting in a change of the P wave velocity.

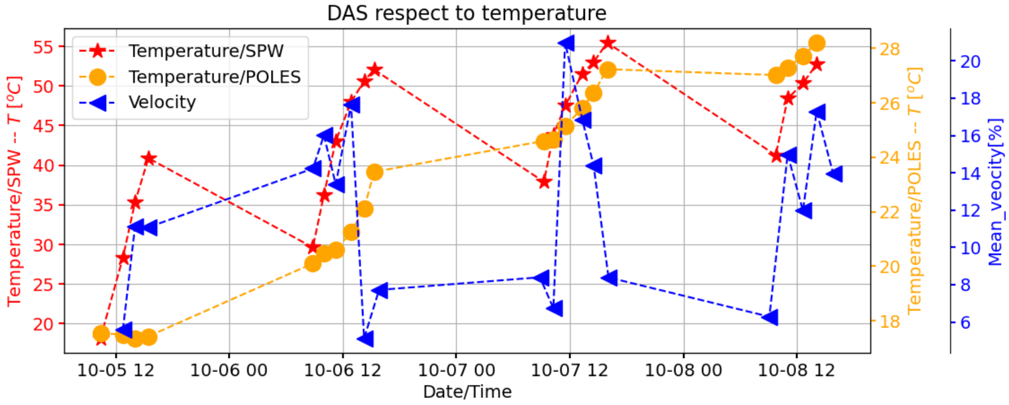

Figure B24 Velocity difference in percentage respect to temperature of injected warm water.

Converting Vp to temperature

For the lab experiment it turned out difficult to obtain a temperature distribution that strongly resembles the temperature distribution as obtained by the DTS measurements. We believe that is at least partly due to the location of the hot water in relation to the acoustic source and monitoring locations: the injection of hot water results more or less in a cylinder of hot water around the injection well from the water table to the bottom of the tank. All waves propagating from each acoustic source along the diagonal plane through the injection well will always pass this cylinder of hot water, which will result in a delay of the arrival time compared to the initial temperature distribution. However, during the inversion of the data, there is no information that there is this cylinder of hot water around the injection well and an increase of the temperature at any location along the diagonal plane from top to bottom will be able to give similar arrival times.

In the results of the synthetic example, this problem was not encountered, but it is clearly visible in Figure B7 that there will always be some waves between acoustic source and receiver that propagates through areas without increased temperature.

The ill-posed inversion of the lab experiment tells us that it is necessary to provide the inversion with adequate information by either have acoustic sources and/or receivers outside the storage formation or provide additional information where the hot water might be, for instance using a heat transport simulation.

Conclusions from laboratory experiment

The recorded DAS signals appears to be sensitive to the velocity variations caused by the induced warm water. The increase in temperature appears to reduce the Vp which appears consistent with the DTS profiles recorded at equivalent time instants.

Furthermore, the temperature and Vp depict consistent correlation that is the higher the temperature the lower the velocity respect to the initial condition. Thus, DAS should depict similar response in field-scale experiment making possible to map velocities changes induced by warm water.

Based on the lab experiment two additional conclusions about the applicability of the technique can be drawn. The first is that an unexpected change, such as the hypothesized compaction or escape of trapped gas in the tank, has an impact on the DAS measurements. In practical applications of high temperature storage compaction is not likely to occur, but particle transport may also have an impact.
The second conclusion is that the inversion by the DAS should be provided good data either by a good set up of the sources and receivers of by additional data for instance from a heat transport simulation.

B5 Discussion

From the modelling it seems to be very clear that the ACT method has the capabilities of mapping velocity changes induced by temperature. However, considering the limited information about the actual effect of temperature for local Vp in geothermal well, the correlation utilized in this study may be not representative for all conditions.

Even though the recorded Vp with DAS in the lab experiment seems to be in good agreement with the recorded reference data, only 4 borehole depths provided similar Vp distribution in the velocity range between 200 m/s – 600 m/s. The travel times obtained with borehole depth at -2.2 m appears higher than the other 4 positions. This disagreement could be related the proximity of the source to the bottom of the well which resulted in a destructive effect of the strong reflection coming for the bottom, so the actual first arrivals were not consistent.

For the lab experiment, the computed velocities which are below 1500 m/s indicates that the sandy layers were not fully saturated or contained trapped gas; thus, the results presented in this work corresponds to partially saturated soils which is not really the case in real world conditions. Nevertheless, despite the fully saturated condition was not satisfied, DAS should be successfully implemented at fully saturated conditions so potential changes of Vp due to changes in thermal conductivity should be observed.

B6 Conclusions

The main conclusions of the research are as follows:

- The modelling results indicate that ACT would be sensitive at velocity differences of 10% or higher. This velocity difference occurs approximately when the injection temperature is about 15 °C higher than the initial temperature. For high temperature storage systems, the temperature difference is thus large enough to be able to use ACT.
- The setup of an ACT experiment in a tank did encounter various unexpected effects, such as compaction or escape of trapped gas that has an impact on the ACT signal, but during the initial stage of the experiment there was a clear correlation between the decrease of the p wave velocity and the increased temperature.
- The inversion of the ACT data should be based on an adequate set up of the acoustic sources and receiver or should be supplied with additional information about center of the hot water.

B7 References

Chang, H., & Nakata, N. J. R. S. (2022). Investigation of Time-Lapse Changes with DAS Borehole Data at the Brady Geothermal Field Using Deconvolution Interferometry. *14*(1), 185.

Hamdhan, I. N., & Clarke, B. G. (2010). *Determination of thermal conductivity of coarse and fine sand soils.* Paper presented at the Proceedings of World Geothermal Congress.

Hartmann, A., Rath, V., Clauser, C., & Sciences, M. (2005). Thermal conductivity from core and well log data. *J International Journal of Rock Mechanics, 42*(7-8), 1042-1055.

Hearn, S., Strong, S., & Kinmont, A. J. A. E. A. (2019). Observations of geophone spurious resonance. *2019*(1), 1-5.

Jaya, M. S., Shapiro, S., Kristindóttir, L., Bruhn, D., Milsch, H., & Spangenberg, E. (2010). *Temperature-Dependence of Seismic Properties in Geothermal Core Samples at In-Situ Reservoir Conditions.* Paper presented at the Proceedings World Geothermal Congress. Bali, Indonesia.

Jaya, M. S., Shapiro, S. A., Kristinsdóttir, L. H., Bruhn, D., Milsch, H., & Spangenberg, E. J. G. (2010). Temperature dependence of seismic properties in geothermal rocks at reservoir conditions. *39*(1), 115-123.

Jones, T., Murphy, W., & Nur, A. (1980). *Effects of temperature and saturation on the velocity and attenuation of seismic waves in rocks: applications to geothermal reservoir evaluation*. Retrieved from

Justice, J., Mathisen, M., Vassiliou, A., Shiao, I., Alameddine, B., & Guinzy, N. (1993). Crosswell seismic tomography in improved oil recovery. *J First Break, 11*(6).

Justice, J., Vassiliou, A., Mathisen, M., Singh, S., Cunningham, P., & Hutt, P. (1992). Acoustic tomography in reservoir surveillance. *J Reservoir geophysics: Soc. Expl. Geophysics, Investigations in Geophysics, 7*, 321-334.

Justice, J., Vassiliou, A., Singh, S., Logel, J., Hansen, P., Hall, B., . . . Solanki, J. (1989). Acoustic tomography for monitoring enhanced oil recovery. *J The Leading Edge, 8*(2), 12-19.

Liu, W. (1999). *Time-lapse crosswell seismic monitoring of the Athabasca Tar Sands.*

Nalonnil, A., Marion, B., & Engineering. (2012). High-resolution reservoir monitoring using crosswell seismic. *J SPE Reservoir Evaluation, 15*(01), 25-30.

Raji, W. O., Gao, Y., & Harris, J. M. (2017). Wavefield analysis of crosswell seismic data. *Arabian Journal of Geosciences, 10*(9). doi:10.1007/s12517-017-2964-6

Schön, J. (2011). *Physical properties of rocks: A workbook* (Vol. 8): Elsevier.

Tamura, S., Tokimatsu, K., Abe, A., Sato, M. J. S., & foundations. (2002). Effects of air bubbles on B-value and P-wave velocity of a partly saturated sand. *42*(1), 121-129.

Appendix B-A: Recording schedule

Activity	Date	Initial time [HH:MM:SS]	Ending time [HH:MM:SS]	Record duration [s]	Source depth [m]	Number of shots per position	Record name
CW	**5-10-2021**	**10:02:00**		3	2.2	5	WMUP5C_SBS42_50kHz
				3	1.8	5	WMUP5C_SBS42_50kHz
				3	1.4	5	WMUP5C_SBS42_50kHz
				3	1	5	WMUP5C_SBS42_50kHz
			10:40:00	3	0.6	5	WMUP5C_SBS42_50kHz
HW1		**12:45:00**		3	2.2	5	WMUP5C_SBS42_50kHz
				3	1.8	5	WMUP5C_SBS42_50kHz
				3	1.4	5	WMUP5C_SBS42_50kHz
				3	1	5	WMUP5C_SBS42_50kHz
			12:56	3	0.6	5	WMUP5C_SBS42_50kHz
HW2		**14:02**		3	2.2	5	WMUP5C_SBS42_50kHz
				3	1.8	5	WMUP5C_SBS42_50kHz
				3	1.4	5	WMUP5C_SBS42_50kHz
				3	1	5	WMUP5C_SBS42_50kHz
			14:10:00	3	0.6	5	WMUP5C_SBS42_50kHz
HW3		**15:27**		3	2.2	5	WMUP5C_SBS42_50kHz
				3	1.8	5	WMUP5C_SBS42_50kHz
				3	1.4	5	WMUP5C_SBS42_50kHz
				3	1	5	WMUP5C_SBS42_50kHz
			15:33	3	0.6	5	WMUP5C_SBS42_50kHz
HW4	**6-10-2021**	**08:50**		3	2.2	5	WMUP5C_SBS42_50kHz
				3	1.8	5	WMUP5C_SBS42_50kHz
				3	1.4	5	WMUP5C_SBS42_50kHz
				3	1	5	WMUP5C_SBS42_50kHz

			08:57	3	0.6	5	WMUP5C_SBS42_50kHz
HW5		**10:00**		3	2.2	5	WMUP5C_SBS42_50kHz
				3	1.8	5	WMUP5C_SBS42_50kHz
				3	1.4	5	WMUP5C_SBS42_50kHz
				3	1	5	WMUP5C_SBS42_50kHz
			10:17	3	0.6	5	WMUP5C_SBS42_50kHz
HW6		**11:15**		3	2.2	5	WMUP5C_SBS42_50kHz
				3	1.8	5	WMUP5C_SBS42_50kHz
				3	1.4	5	WMUP5C_SBS42_50kHz
				3	1	5	WMUP5C_SBS42_50kHz
			11:28	3	0.6	5	WMUP5C_SBS42_50kHz
HW7		**12:52**		3	2.2	5	WMUP5C_SBS42_50kHz
				3	1.8	5	WMUP5C_SBS42_50kHz
				3	1.4	5	WMUP5C_SBS42_50kHz
				3	1	5	WMUP5C_SBS42_50kHz
			13:08	3	0.6	5	WMUP5C_SBS42_50kHz
HW8		**14:15**		3	2.2	5	WMUP5C_SBS42_50kHz
				3	1.8	5	WMUP5C_SBS42_50kHz
				3	1.4	5	WMUP5C_SBS42_50kHz
				3	1	5	WMUP5C_SBS42_50kHz
			14:30	3	0.6	5	WMUP5C_SBS42_50kHz
HW9		**15:50**		3	2.2	5	WMUP5C_SBS42_50kHz
				3	1.8	5	WMUP5C_SBS42_50kHz
				3	1.4	5	WMUP5C_SBS42_50kHz
				3	1	5	WMUP5C_SBS42_50kHz
			16:05	3	0.6	5	WMUP5C_SBS42_50kHz

HW10	**7-10-2021**	**08:50**		3	2.2	5	WMUP5C_SBS42_50kHz
				3	1.8	5	WMUP5C_SBS42_50kHz
				3	1.4	5	WMUP5C_SBS42_50kHz
				3	1	5	WMUP5C_SBS42_50kHz
			09:05	3	0.6	5	WMUP5C_SBS42_50kHz
HW11		**10:15**		3	2.2	5	WMUP5C_SBS42_50kHz
				3	1.8	5	WMUP5C_SBS42_50kHz
				3	1.4	5	WMUP5C_SBS42_50kHz
				3	1	5	WMUP5C_SBS42_50kHz
			10:30	3	0.6	5	WMUP5C_SBS42_50kHz
HW12		**11:30**		3	2.2	5	WMUP5C_SBS42_50kHz
				3	1.8	5	WMUP5C_SBS42_50kHz
				3	1.4	5	WMUP5C_SBS42_50kHz
				3	1	5	WMUP5C_SBS42_50kHz
			11:45	3	0.6	5	WMUP5C_SBS42_50kHz
HW13		**13:19**		3	2.2	5	WMUP5C_SBS42_50kHz
				3	1.8	5	WMUP5C_SBS42_50kHz
				3	1.4	5	WMUP5C_SBS42_50kHz
				3	1	5	WMUP5C_SBS42_50kHz
			13:34	3	0.6	5	WMUP5C_SBS42_50kHz
HW14		**14:30**		3	2.2	5	WMUP5C_SBS42_50kHz
				3	1.8	5	WMUP5C_SBS42_50kHz
				3	1.4	5	WMUP5C_SBS42_50kHz
				3	1	5	WMUP5C_SBS42_50kHz
			14:44	3	0.6	5	WMUP5C_SBS42_50kHz
HW15		**16:05**		3	2.2	5	WMUP5C_SBS42_50kHz

				3	1.8	5	WMUP5C_SBS42_50kHz
				3	1.4	5	WMUP5C_SBS42_50kHz
				3	1	5	WMUP5C_SBS42_50kHz
			16:27	3	0.6	5	WMUP5C_SBS42_50kHz
HW16	**8-10-2021**	**09:05**		3	2.2	5	WMUP5C_SBS42_50kHz
				3	1.8	5	WMUP5C_SBS42_50kHz
				3	1.4	5	WMUP5C_SBS42_50kHz
				3	1	5	WMUP5C_SBS42_50kHz
			09:37	3	0.6	5	WMUP5C_SBS42_50kHz
HW17		**11:01**		3	2.2	5	WMUP5C_SBS42_50kHz
				3	1.8	5	WMUP5C_SBS42_50kHz
				3	1.4	5	WMUP5C_SBS42_50kHz
				3	1	5	WMUP5C_SBS42_50kHz
			11:27	3	0.6	5	WMUP5C_SBS42_50kHz
HW18		**12:38**		3	2.2	5	WMUP5C_SBS42_50kHz
				3	1.8	5	WMUP5C_SBS42_50kHz
				3	1.4	5	WMUP5C_SBS42_50kHz
				3	1	5	WMUP5C_SBS42_50kHz
			12:54	3	0.6	5	WMUP5C_SBS42_50kHz
HW19		**14:05**		3	2.2	5	WMUP5C_SBS42_50kHz
				3	1.8	5	WMUP5C_SBS42_50kHz
				3	1.4	5	WMUP5C_SBS42_50kHz
				3	1	5	WMUP5C_SBS42_50kHz
			14:20	3	0.6	5	WMUP5C_SBS42_50kHz
HW20		**15:50**		3	2.2	5	WMUP5C_SBS42_50kHz
				3	1.8	5	WMUP5C_SBS42_50kHz

			3	1.4	5	WMUP5C_SBS42_50kHz
			3	1	5	WMUP5C_SBS42_50kHz
		16:05	3	0.6	5	WMUP5C_SBS42_50kHz

Appendix B-B Coordinates of sources and receivers

Receiver number	Receiver Depth[cm]	Depth Interval [cm]	Source depth_ref level in cm	Depth respect to ref in cm	Source Depth
1	0	8.35	40	40	
2	8.35	8.35	40	48.35	
3	17.7	9.35	40	57.7	**Source_60**
4	26.05	8.35	40	66.05	
5	35.4	9.35	40	75.4	
6	43.75	8.35	40	83.75	
7	53.1	9.35	40	93.1	
8	61.45	8.35	40	101.45	**Source_100**
9	69.8	8.35	40	109.8	
10	79.15	9.35	40	119.15	
11	87.5	8.35	40	127.5	
12	96.85	9.35	40	136.85	**Source_140**
13	105.2	8.35	40	145.2	
14	114.55	9.35	40	154.55	
15	122.9	8.35	40	162.9	
16	132.25	9.35	40	172.25	
17	140.6	8.35	40	180.6	**Source_180**
18	148.95	8.35	40	188.95	
19	158.3	9.35	40	198.3	
20	166.65	8.35	40	206.65	
21	176	9.35	40	216	
22	184.35	8.35	40	224.35	**Source_220**
23	193.7	9.35	40	233.7	
24	202.05	8.35	40	242.05	
25	210.4	8.35	40	250.4	

Appendix B-C Inverted Vp for individual borehole source depths

Borehole source depth at - 0.6 m

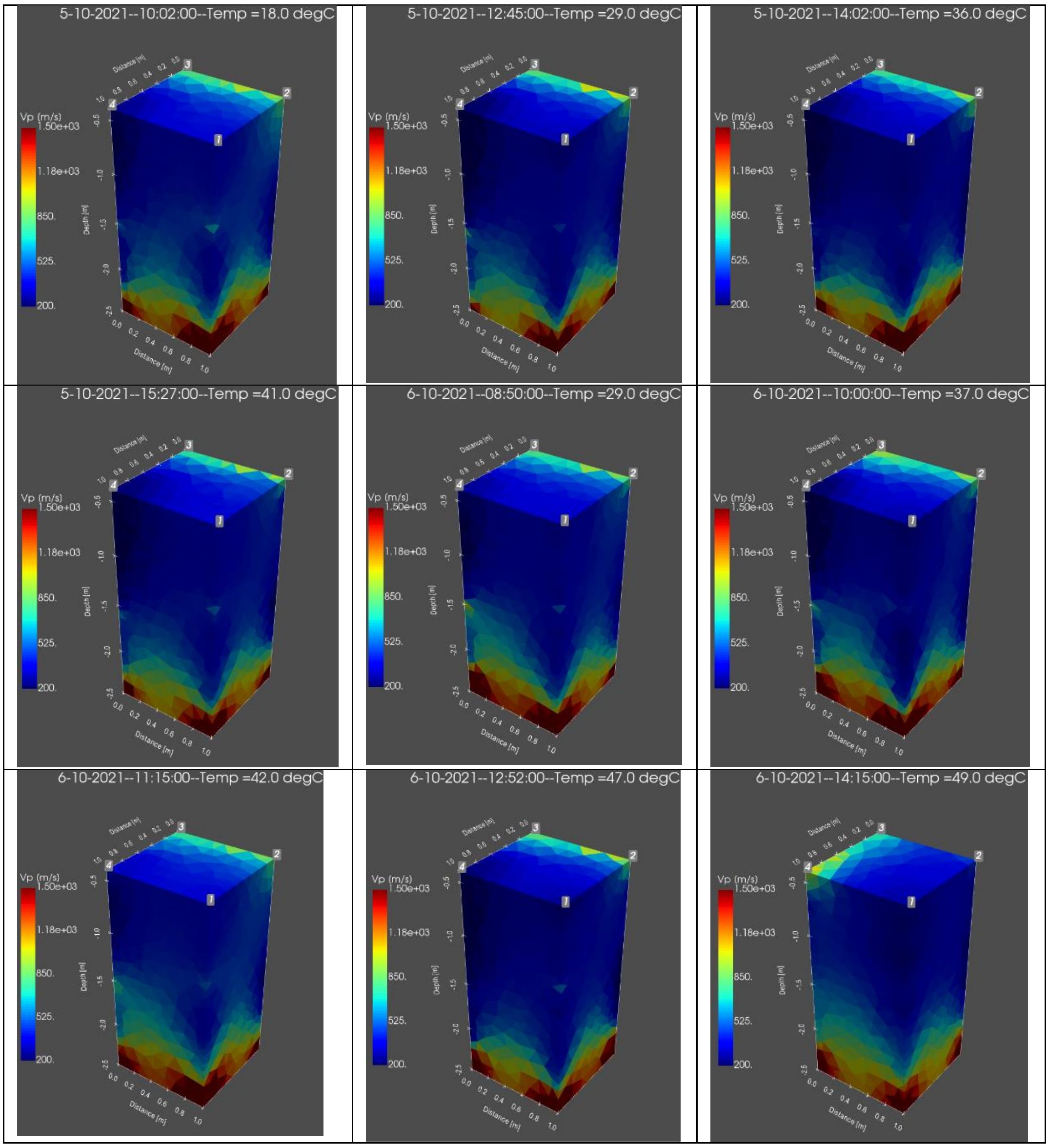
5-10-2021--10:02:00--Temp =18.0 degC
5-10-2021--12:45:00--Temp =29.0 degC
5-10-2021--14:02:00--Temp =36.0 degC
5-10-2021--15:27:00--Temp =41.0 degC
6-10-2021--08:50:00--Temp =29.0 degC
6-10-2021--10:00:00--Temp =37.0 degC
6-10-2021--11:15:00--Temp =42.0 degC
6-10-2021--12:52:00--Temp =47.0 degC
6-10-2021--14:15:00--Temp =49.0 degC
Vp (m/s)
1.50e+03
1.18e+03
850.
525.
200.
Depth [m]
-0.5
-1.0
-1.5
-2.0
-2.5
Distance [m]
0.0
0.2
0.4
0.6
0.8
1.0
1
2
3
4

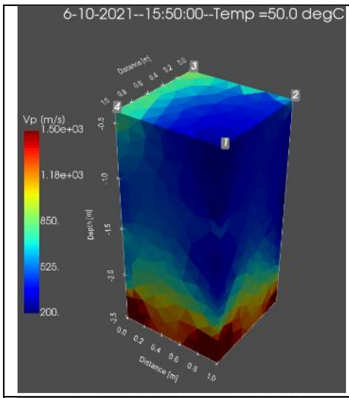
6-10-2021--15:50:00--Temp =50.0 degC

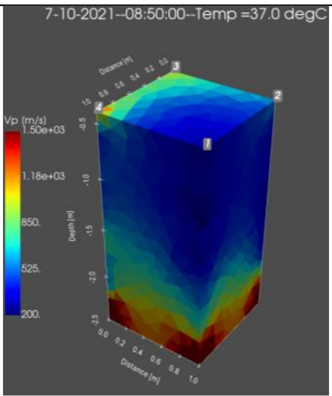
7-10-2021--08:50:00--Temp =37.0 degC

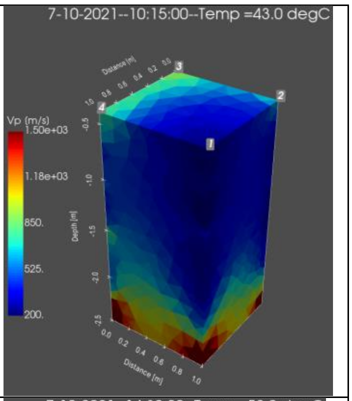
7-10-2021--10:15:00--Temp =43.0 degC

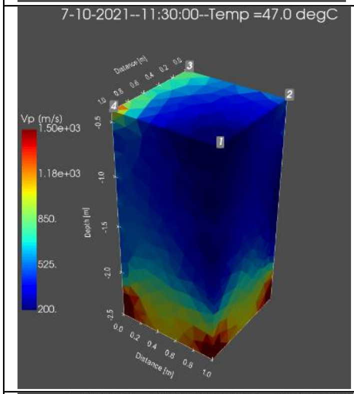
7-10-2021--11:30:00--Temp =47.0 degC

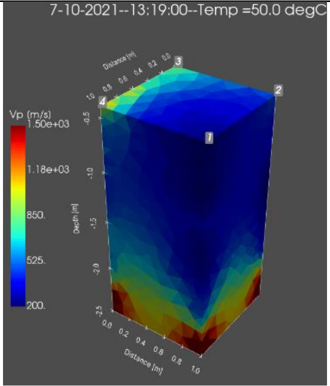
7-10-2021--13:19:00--Temp =50.0 degC

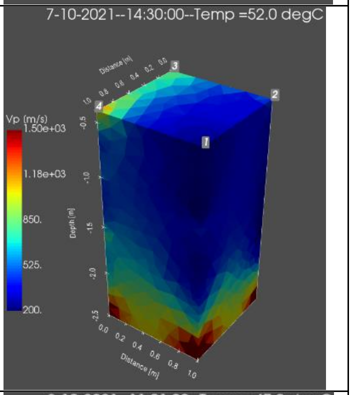
7-10-2021--14:30:00--Temp =52.0 degC

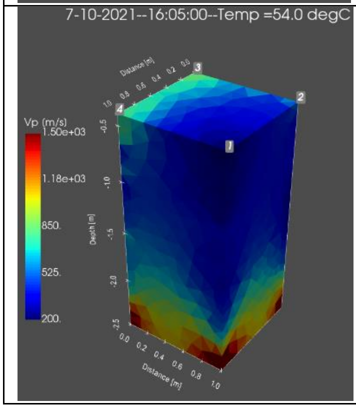
7-10-2021--16:05:00--Temp =54.0 degC

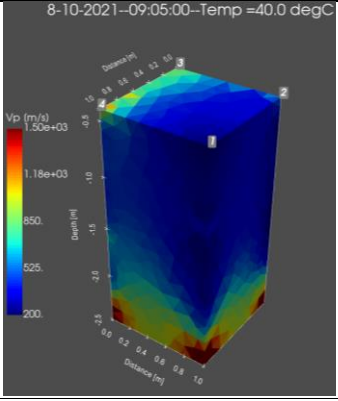
8-10-2021--09:05:00--Temp =40.0 degC

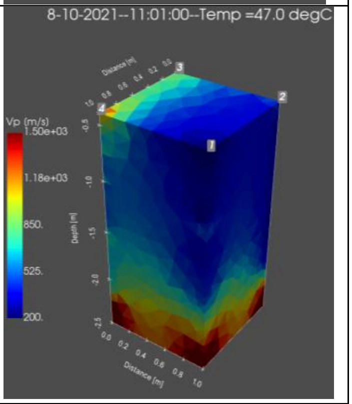
8-10-2021--11:01:00--Temp =47.0 degC

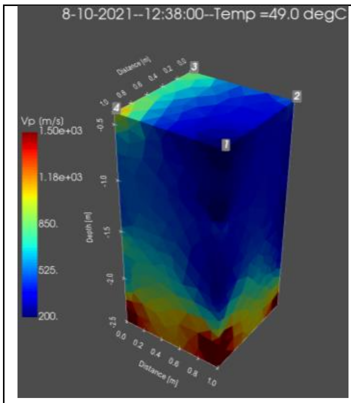
8-10-2021--12:38:00--Temp =49.0 degC

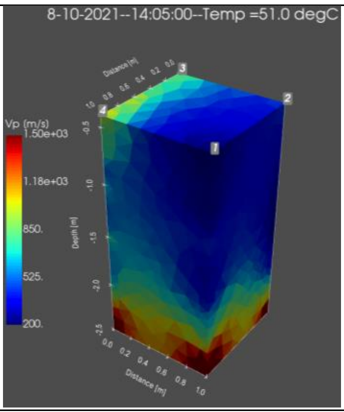
8-10-2021--14:05:00--Temp =51.0 degC

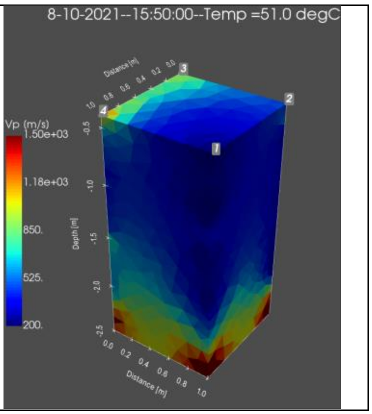
8-10-2021--15:50:00--Temp =51.0 degC

Borehole source depth at – 1.0 m

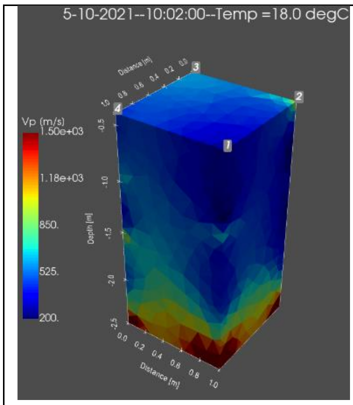

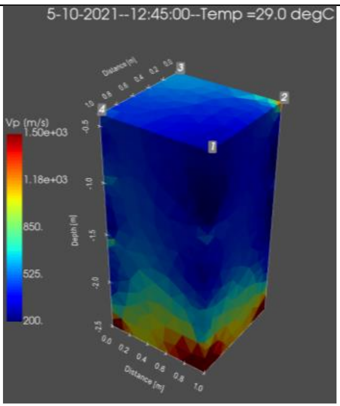

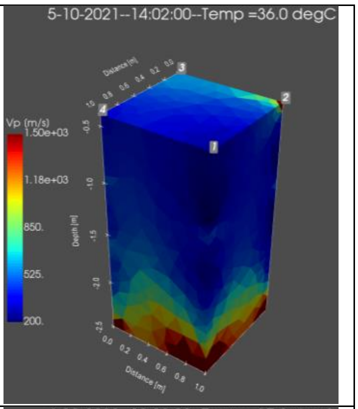

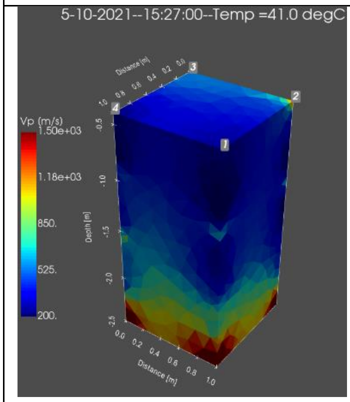

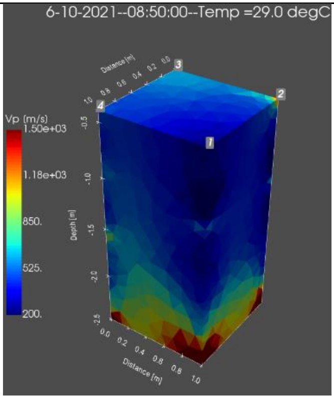

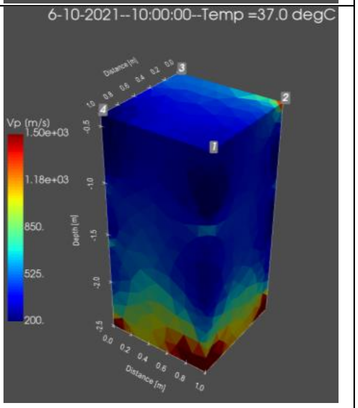

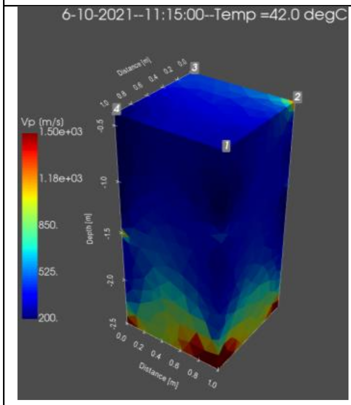

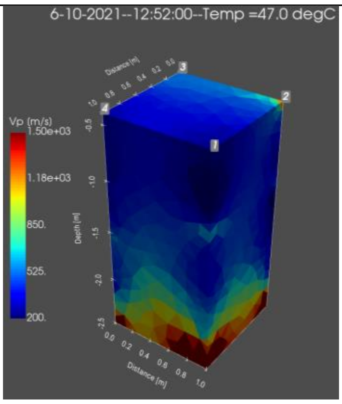

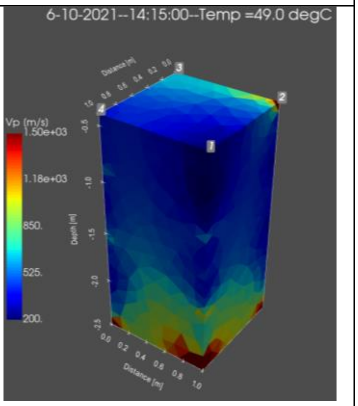

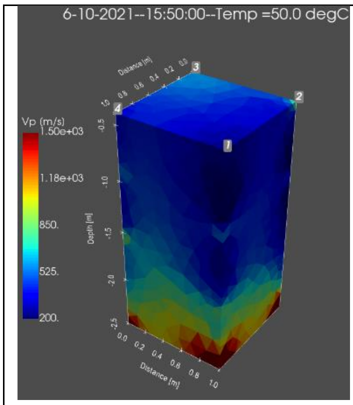

6-10-2021--15:50:00--Temp =50.0 degC

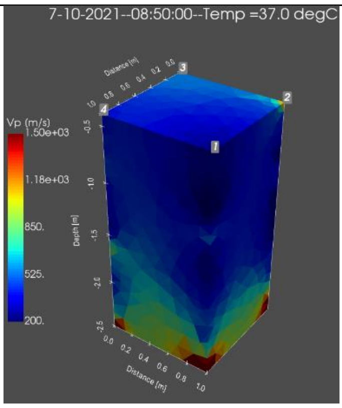

7-10-2021--08:50:00--Temp =37.0 degC

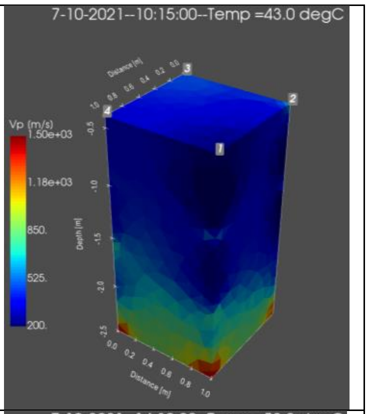

7-10-2021--10:15:00--Temp =43.0 degC

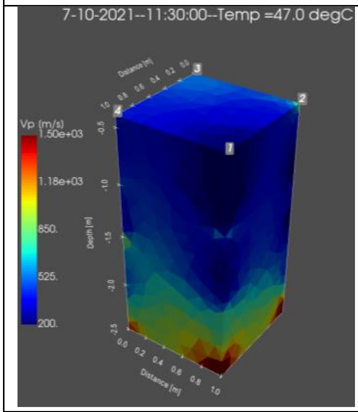

7-10-2021--11:30:00--Temp =47.0 degC

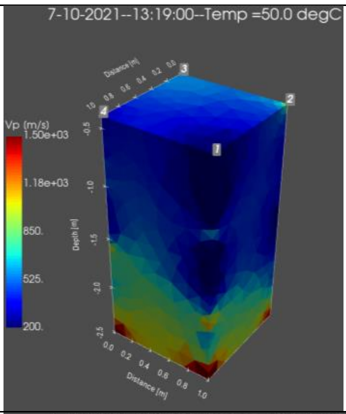

7-10-2021--13:19:00--Temp =50.0 degC

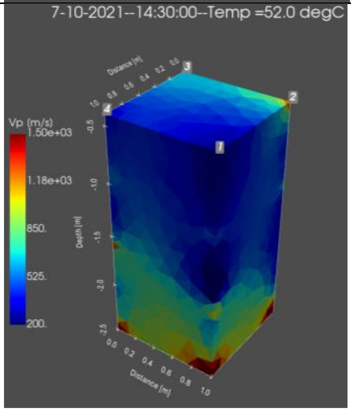

7-10-2021--14:30:00--Temp =52.0 degC

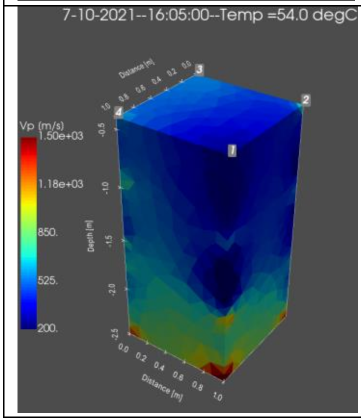

7-10-2021--16:05:00--Temp =54.0 degC

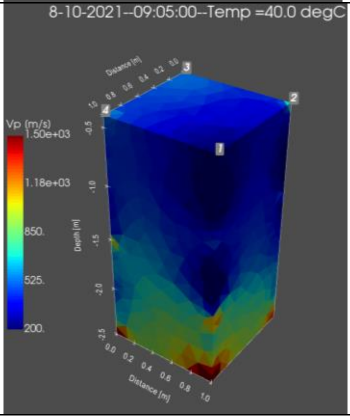

8-10-2021--09:05:00--Temp =40.0 degC

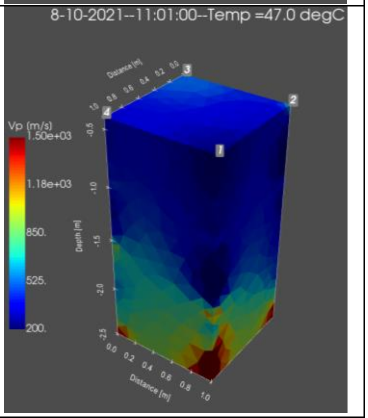

8-10-2021--11:01:00--Temp =47.0 degC

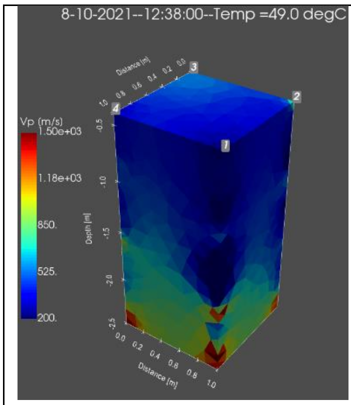

8-10-2021--12:38:00--Temp =49.0 degC

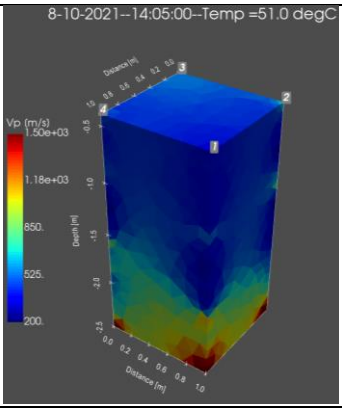

8-10-2021--14:05:00--Temp =51.0 degC

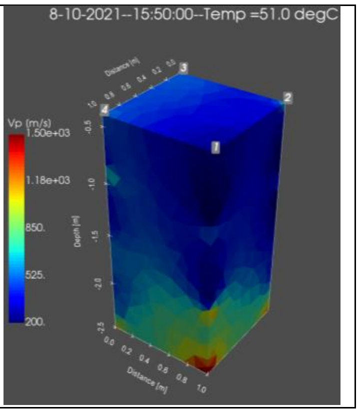

8-10-2021--15:50:00--Temp =51.0 degC

Borehole source depth at – 1.4 m

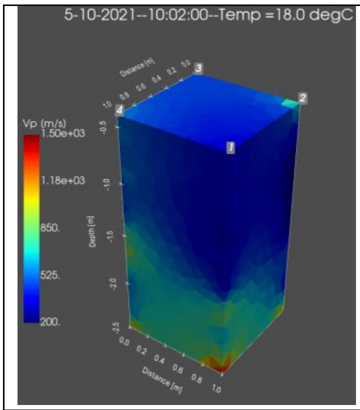

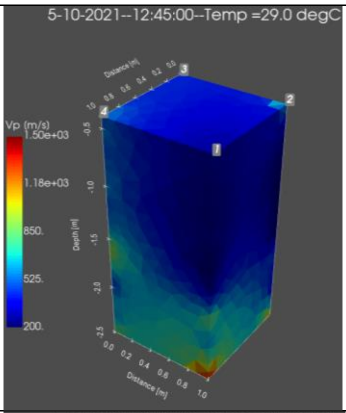

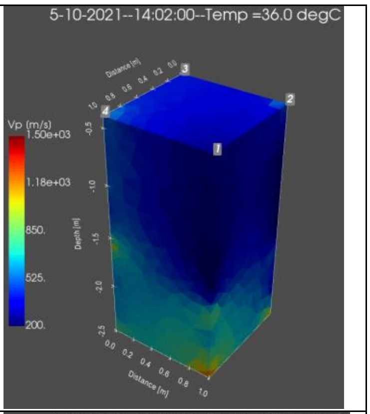

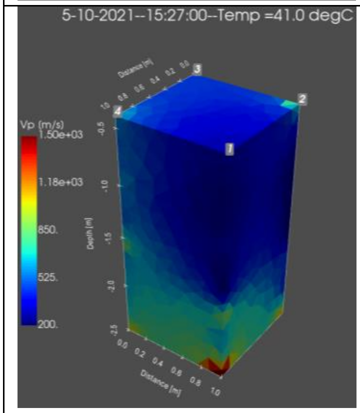

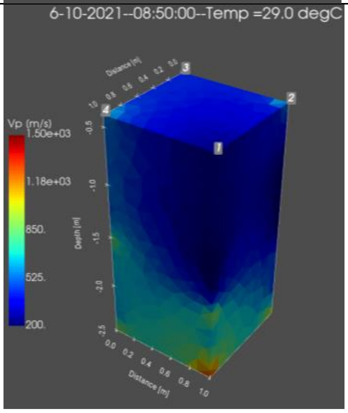

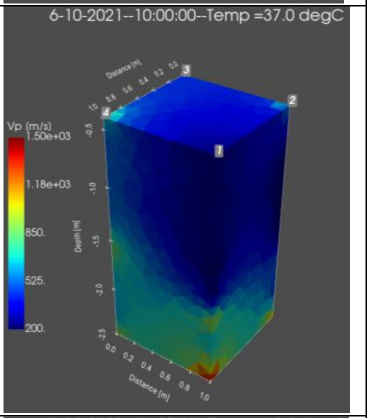

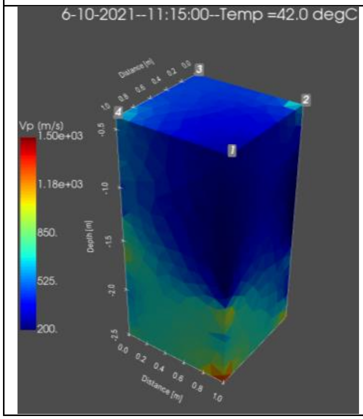

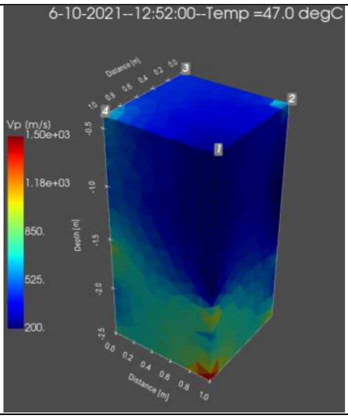

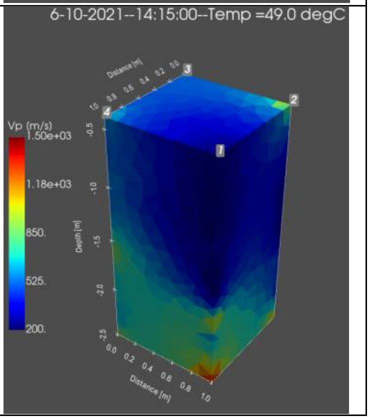

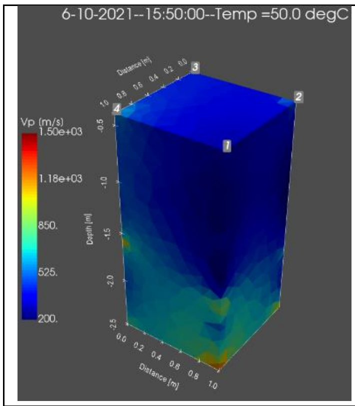
6-10-2021--15:50:00--Temp =50.0 degC
Vp (m/s)
1.50e+03
1.18e+03
850.
525.
200.
Depth [m]
Distance [m]
1
2
3
4

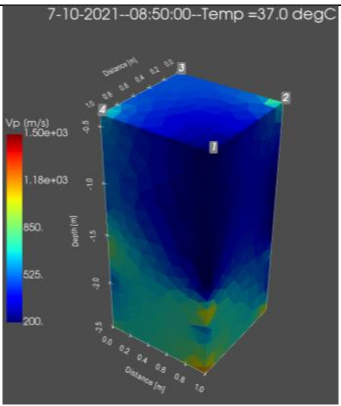
7-10-2021--08:50:00--Temp =37.0 degC
Vp (m/s)
1.50e+03
1.18e+03
850.
525.
200.
Depth [m]
Distance [m]

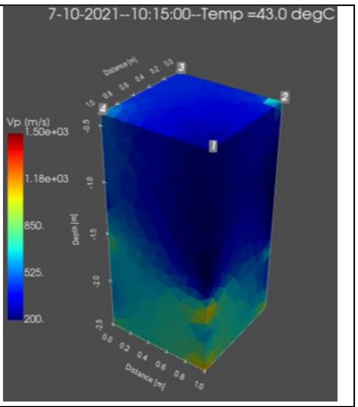
7-10-2021--10:15:00--Temp =43.0 degC
Vp (m/s)
1.50e+03
1.18e+03
850.
525.
200.
Depth [m]
Distance [m]

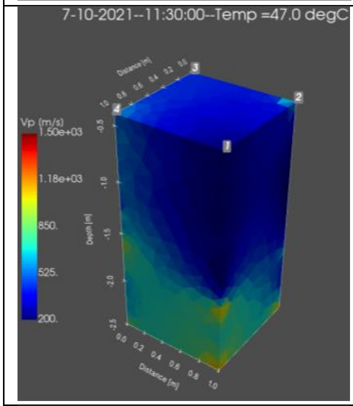
7-10-2021--11:30:00--Temp =47.0 degC
Vp (m/s)
1.50e+03
1.18e+03
850.
525.
200.
Depth [m]
Distance [m]

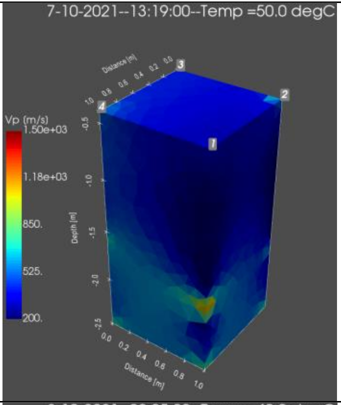
7-10-2021--13:19:00--Temp =50.0 degC
Vp (m/s)
1.50e+03
1.18e+03
850.
525.
200.
Depth [m]
Distance [m]

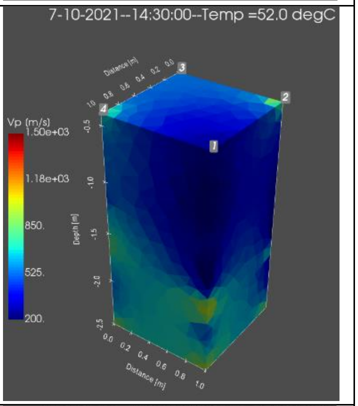
7-10-2021--14:30:00--Temp =52.0 degC
Vp (m/s)
1.50e+03
1.18e+03
850.
525.
200.
Depth [m]
Distance [m]

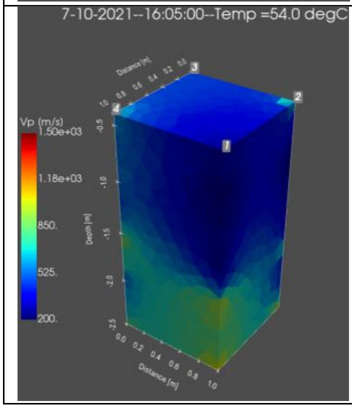
7-10-2021--16:05:00--Temp =54.0 degC
Vp (m/s)
1.50e+03
1.18e+03
850.
525.
200.
Depth [m]
Distance [m]

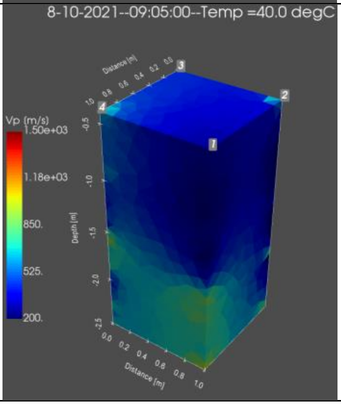
8-10-2021--09:05:00--Temp =40.0 degC
Vp (m/s)
1.50e+03
1.18e+03
850.
525.
200.
Depth [m]
Distance [m]

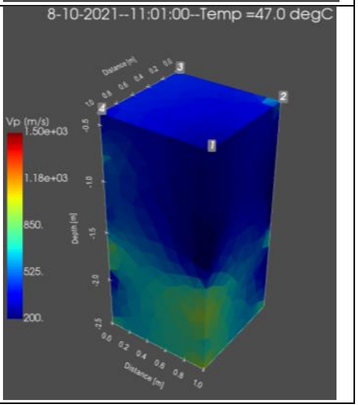
8-10-2021--11:01:00--Temp =47.0 degC
Vp (m/s)
1.50e+03
1.18e+03
850.
525.
200.
Depth [m]
Distance [m]

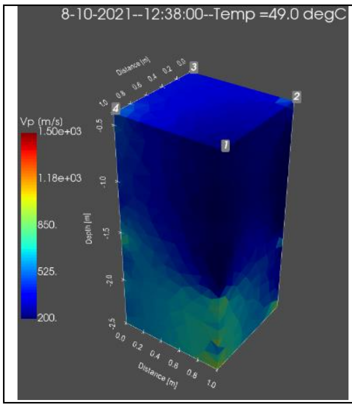
8-10-2021--12:38:00--Temp =49.0 degC
Vp (m/s)
1.50e+03
1.18e+03
850.
525.
200.
Depth [m]
Distance [m]

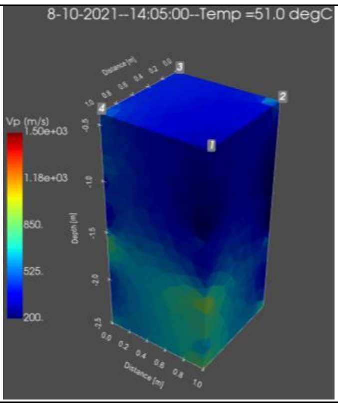
8-10-2021--14:05:00--Temp =51.0 degC
Vp (m/s)
1.50e+03
1.18e+03
850.
525.
200.
Depth [m]
Distance [m]

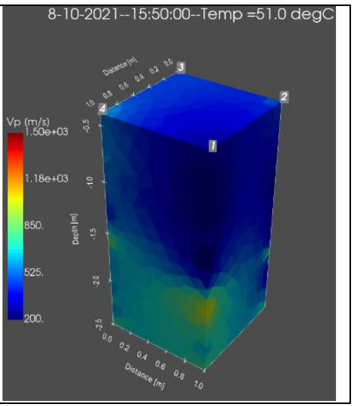
8-10-2021--15:50:00--Temp =51.0 degC
Vp (m/s)
1.50e+03
1.18e+03
850.
525.
200.
Depth [m]
Distance [m]

Borehole source depth at – 1.8 m

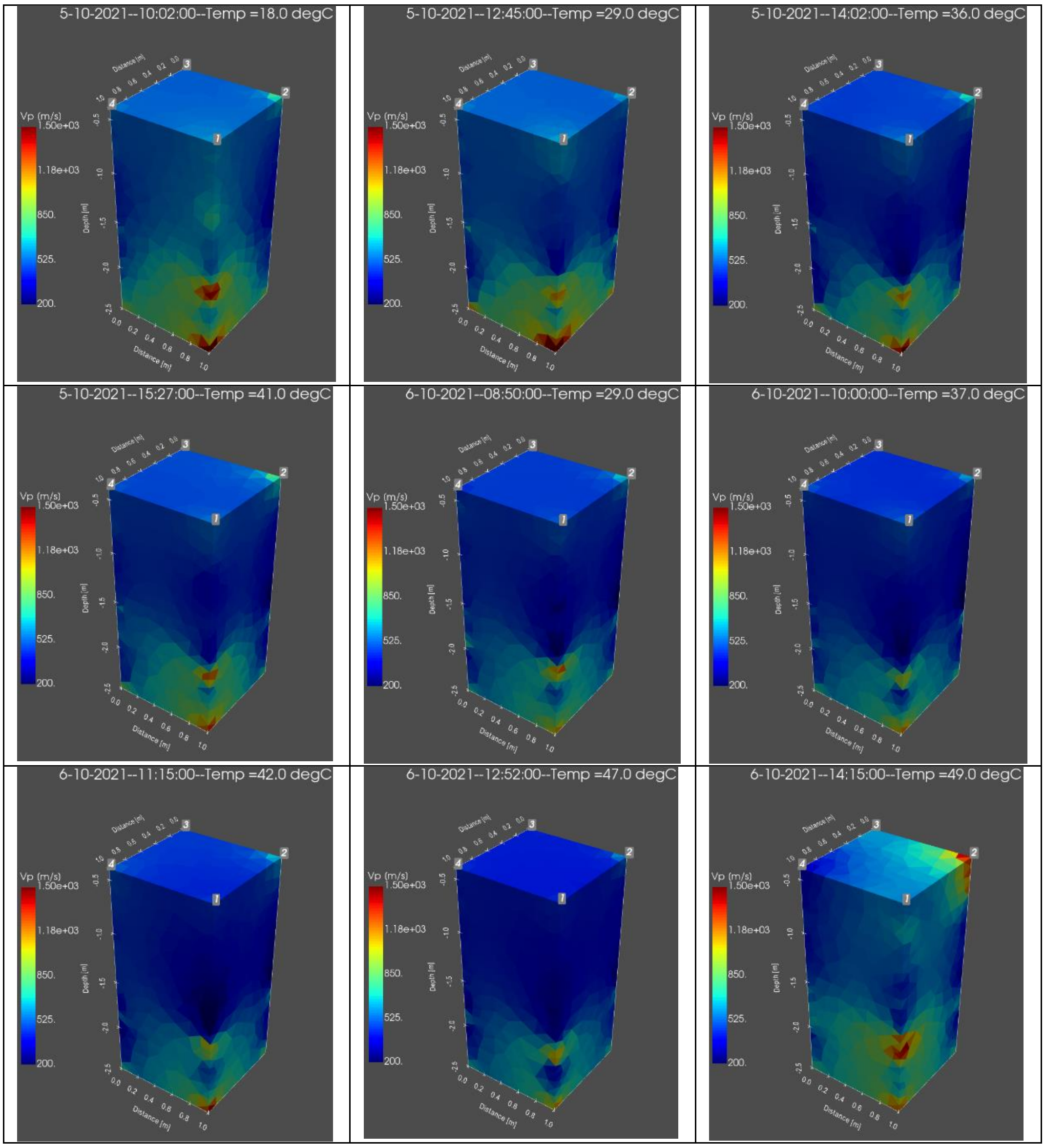

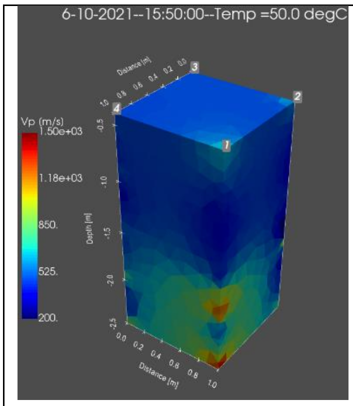
6-10-2021--15:50:00--Temp =50.0 degC
Vp (m/s)
1.50e+03
1.18e+03
850.
525.
200.
Depth [m]
Distance [m]
1
2
3
4

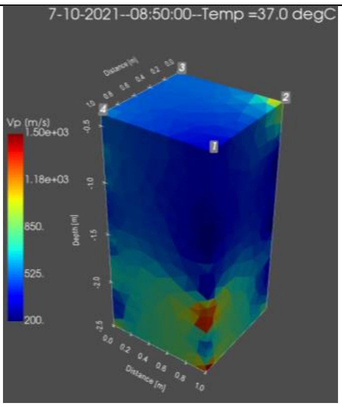
7-10-2021--08:50:00--Temp =37.0 degC
Vp (m/s)
1.50e+03
1.18e+03
850.
525.
200.
Depth [m]
Distance [m]
1
2
3
4

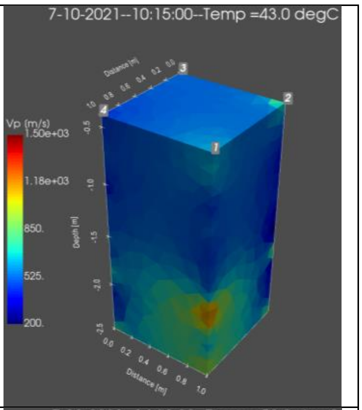
7-10-2021--10:15:00--Temp =43.0 degC
Vp (m/s)
1.50e+03
1.18e+03
850.
525.
200.
Depth [m]
Distance [m]
1
2
3
4

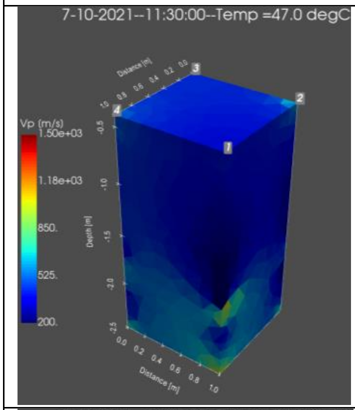
7-10-2021--11:30:00--Temp =47.0 degC
Vp (m/s)
1.50e+03
1.18e+03
850.
525.
200.
Depth [m]
Distance [m]
1
2
3
4

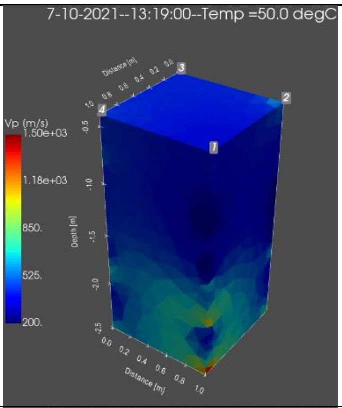
7-10-2021--13:19:00--Temp =50.0 degC
Vp (m/s)
1.50e+03
1.18e+03
850.
525.
200.
Depth [m]
Distance [m]
1
2
3
4

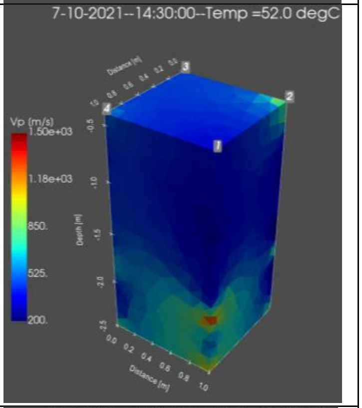
7-10-2021--14:30:00--Temp =52.0 degC
Vp (m/s)
1.50e+03
1.18e+03
850.
525.
200.
Depth [m]
Distance [m]
1
2
3
4

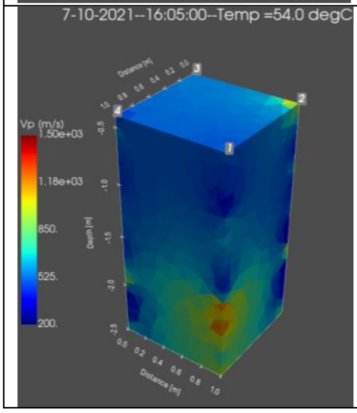
7-10-2021--16:05:00--Temp =54.0 degC
Vp (m/s)
1.50e+03
1.18e+03
850.
525.
200.
Depth [m]
Distance [m]
1
2
3
4

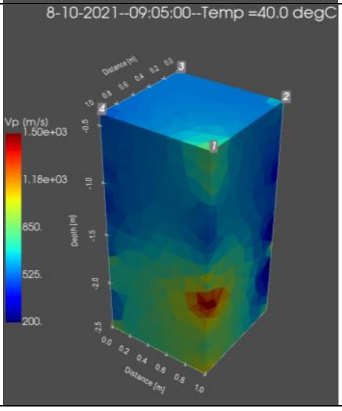
8-10-2021--09:05:00--Temp =40.0 degC
Vp (m/s)
1.50e+03
1.18e+03
850.
525.
200.
Depth [m]
Distance [m]
1
2
3
4

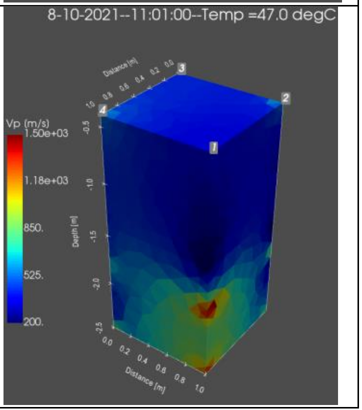
8-10-2021--11:01:00--Temp =47.0 degC
Vp (m/s)
1.50e+03
1.18e+03
850.
525.
200.
Depth [m]
Distance [m]
1
2
3
4

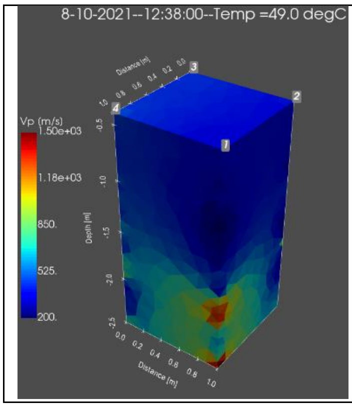
8-10-2021--12:38:00--Temp =49.0 degC
Vp (m/s)
1.50e+03
1.18e+03
850.
525.
200.
Depth [m]
Distance [m]
1
2
3
4

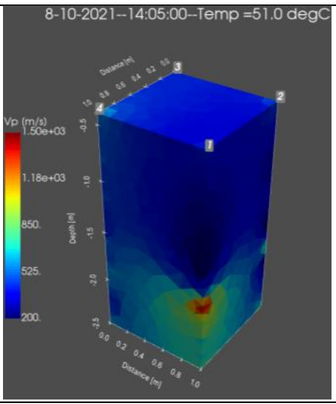
8-10-2021--14:05:00--Temp =51.0 degC
Vp (m/s)
1.50e+03
1.18e+03
850.
525.
200.
Depth [m]
Distance [m]
1
2
3
4

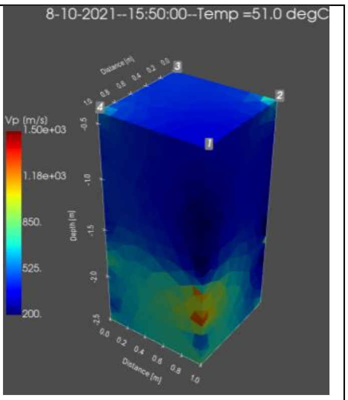
8-10-2021--15:50:00--Temp =51.0 degC
Vp (m/s)
1.50e+03
1.18e+03
850.
525.
200.
Depth [m]
Distance [m]
1
2
3
4

Borehole source depth at – 2.2 m

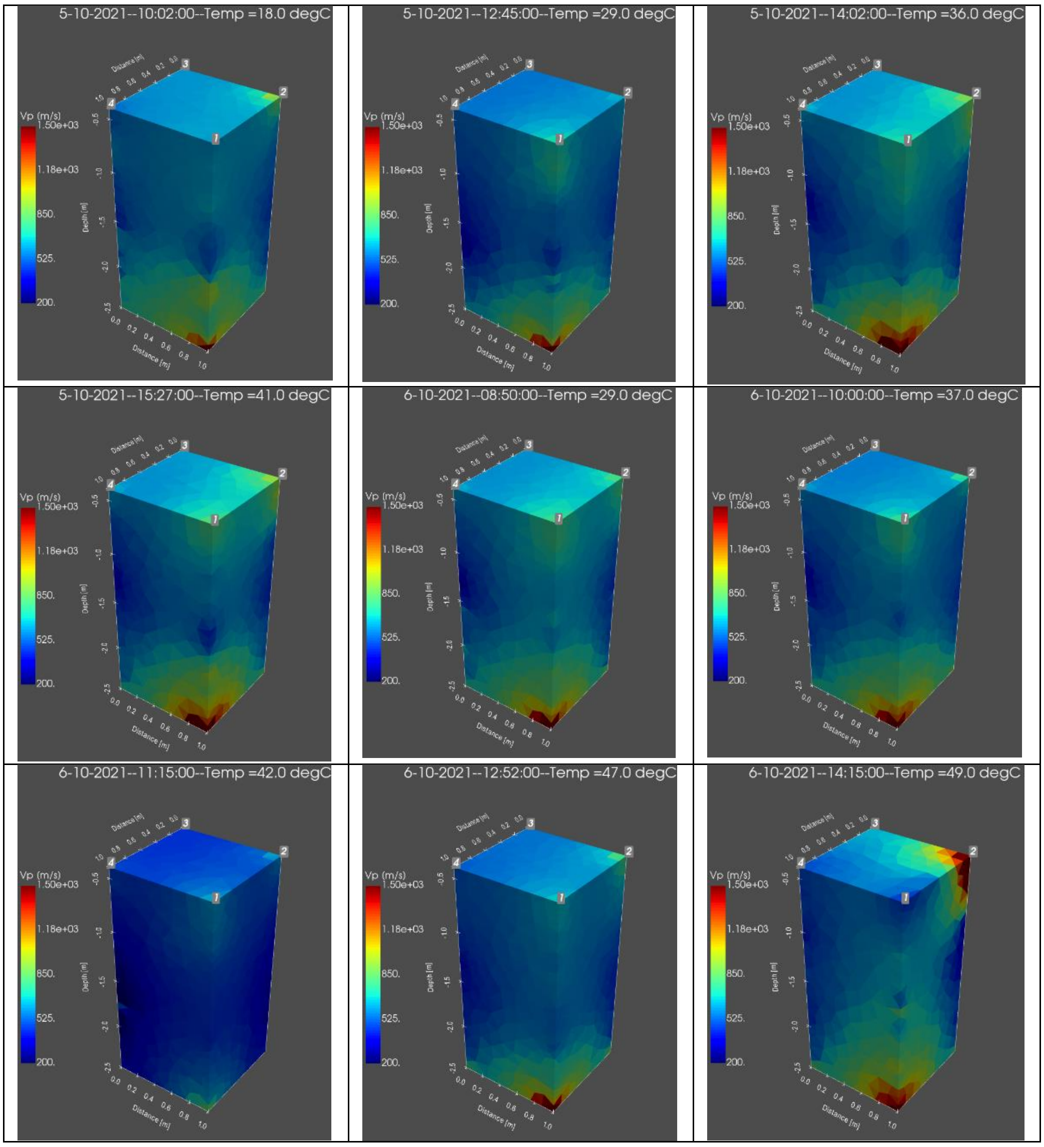

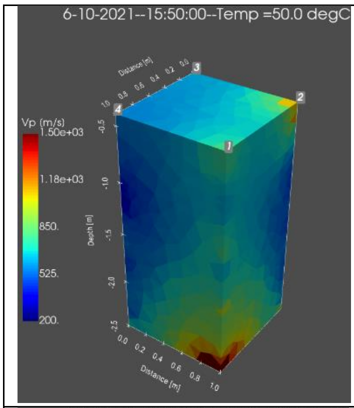
6-10-2021--15:50:00--Temp =50.0 degC
Vp (m/s)
1.50e+03
1.18e+03
850.
525.
200.
Depth [m]
Distance [m]
Distance [m]
1
2
3
4

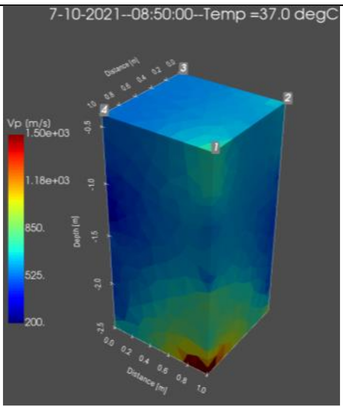
7-10-2021--08:50:00--Temp =37.0 degC
Vp (m/s)
1.50e+03
1.18e+03
850.
525.
200.
Depth [m]
Distance [m]
Distance [m]
1
2
3
4

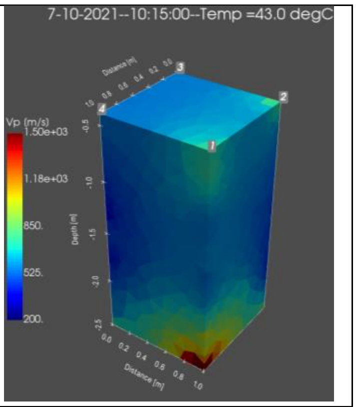
7-10-2021--10:15:00--Temp =43.0 degC
Vp (m/s)
1.50e+03
1.18e+03
850.
525.
200.
Depth [m]
Distance [m]
Distance [m]
1
2
3
4

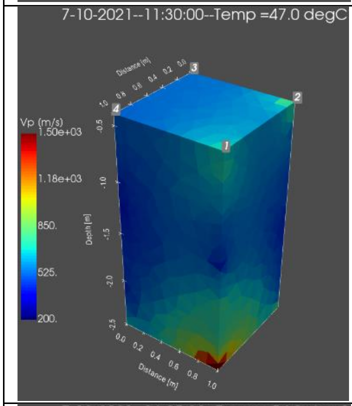
7-10-2021--11:30:00--Temp =47.0 degC
Vp (m/s)
1.50e+03
1.18e+03
850.
525.
200.
Depth [m]
Distance [m]
Distance [m]
1
2
3
4

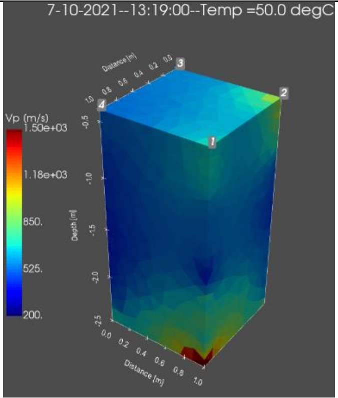
7-10-2021--13:19:00--Temp =50.0 degC
Vp (m/s)
1.50e+03
1.18e+03
850.
525.
200.
Depth [m]
Distance [m]
Distance [m]
1
2
3
4

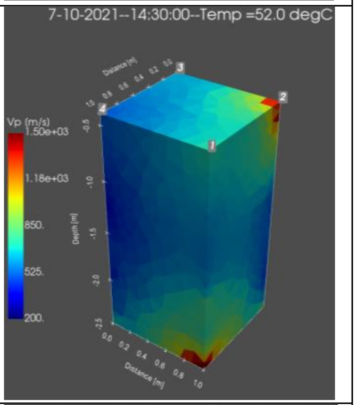
7-10-2021--14:30:00--Temp =52.0 degC
Vp (m/s)
1.50e+03
1.18e+03
850.
525.
200.
Depth [m]
Distance [m]
Distance [m]
1
2
3
4

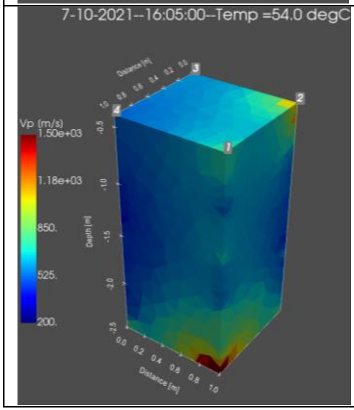
7-10-2021--16:05:00--Temp =54.0 degC
Vp (m/s)
1.50e+03
1.18e+03
850.
525.
200.
Depth [m]
Distance [m]
Distance [m]
1
2
3
4

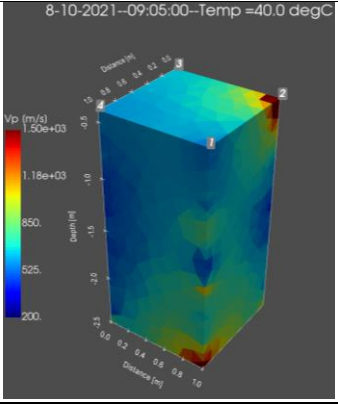
8-10-2021--09:05:00--Temp =40.0 degC
Vp (m/s)
1.50e+03
1.18e+03
850.
525.
200.
Depth [m]
Distance [m]
Distance [m]
1
2
3
4

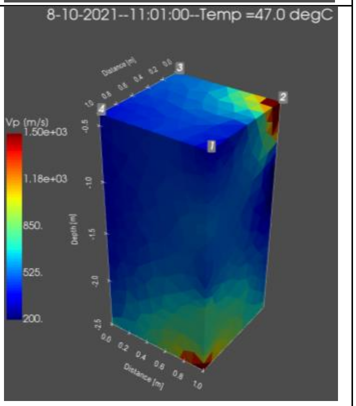
8-10-2021--11:01:00--Temp =47.0 degC
Vp (m/s)
1.50e+03
1.18e+03
850.
525.
200.
Depth [m]
Distance [m]
Distance [m]
1
2
3
4

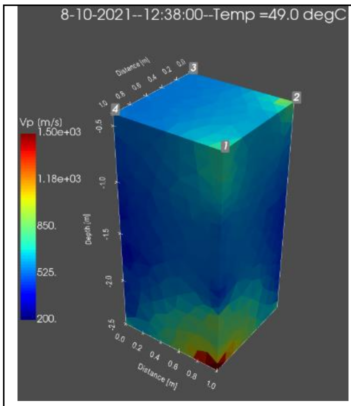
8-10-2021--12:38:00--Temp =49.0 degC
Vp (m/s)
1.50e+03
1.18e+03
850.
525.
200.
Depth [m]
Distance [m]
Distance [m]
1
2
3
4

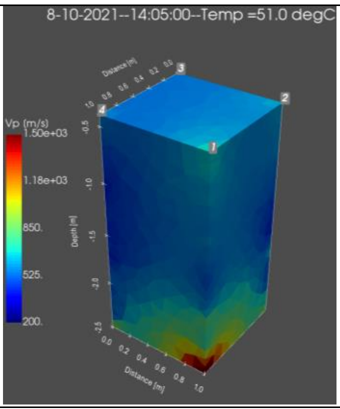
8-10-2021--14:05:00--Temp =51.0 degC
Vp (m/s)
1.50e+03
1.18e+03
850.
525.
200.
Depth [m]
Distance [m]
Distance [m]
1
2
3
4

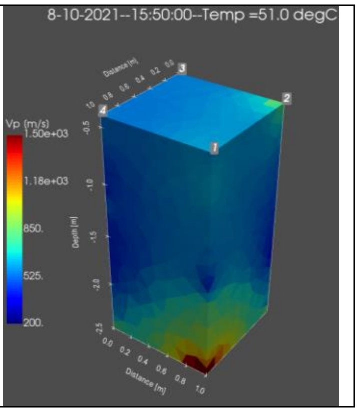
8-10-2021--15:50:00--Temp =51.0 degC
Vp (m/s)
1.50e+03
1.18e+03
850.
525.
200.
Depth [m]
Distance [m]
Distance [m]
1
2
3
4

Appendix B-D Velocity difference respect to T0 of borehole depth at -1.8 m

Vp differences respect to temperature for source depth at -1.8 m.

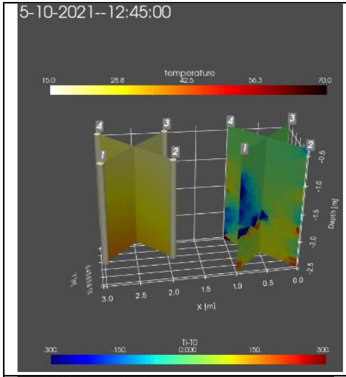

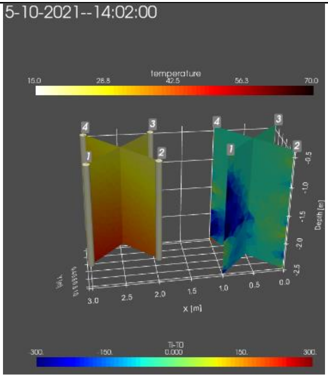

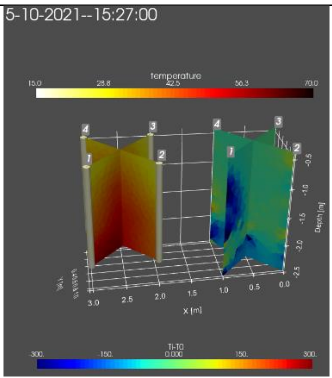

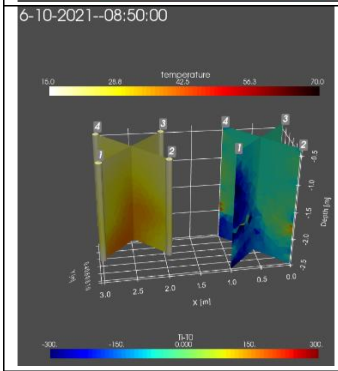

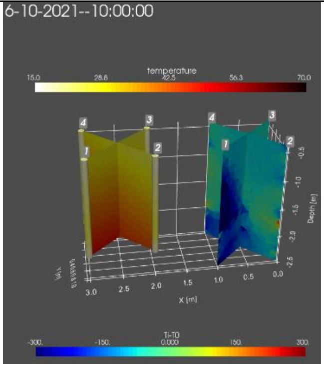

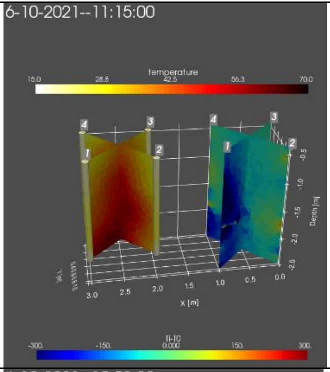

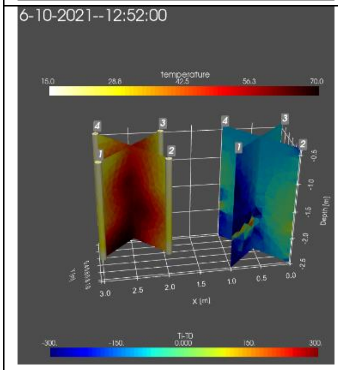

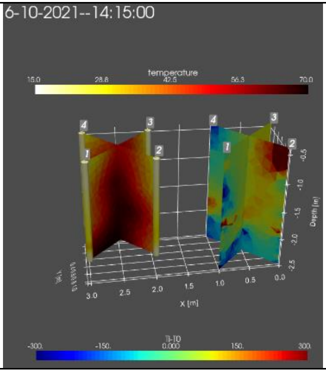

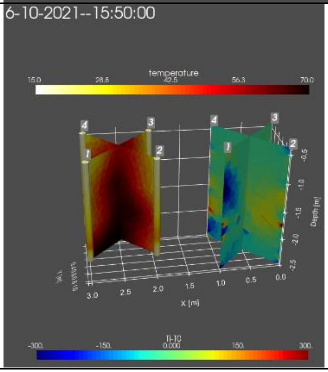

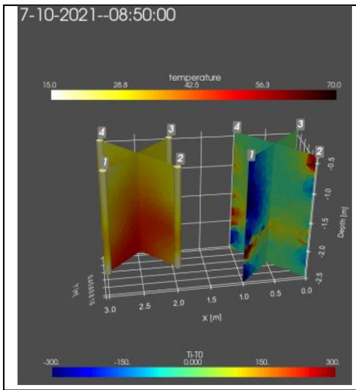
7-10-2021--08:50:00
temperature
15.0 28.8 42.5 56.3 70.0
X [m]
Depth [m]
Ti-T0
-300. -150. 0.000 150. 300.

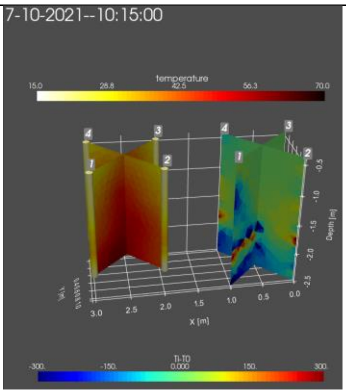
7-10-2021--10:15:00
temperature
15.0 28.8 42.5 56.3 70.0
X [m]
Depth [m]
Ti-T0
-300. -150. 0.000 150. 300.

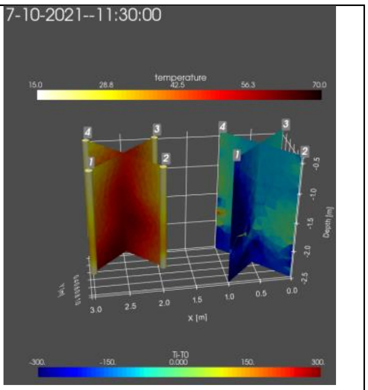
7-10-2021--11:30:00
temperature
15.0 28.8 42.5 56.3 70.0
X [m]
Depth [m]
Ti-T0
-300. -150. 0.000 150. 300.

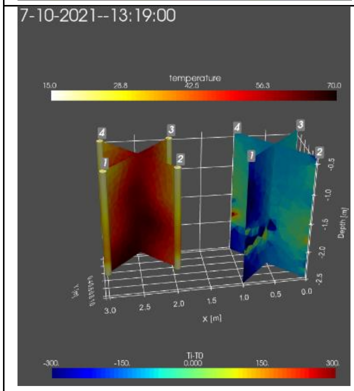
7-10-2021--13:19:00
temperature
15.0 28.8 42.5 56.3 70.0
X [m]
Depth [m]
Ti-T0
-300. -150. 0.000 150. 300.

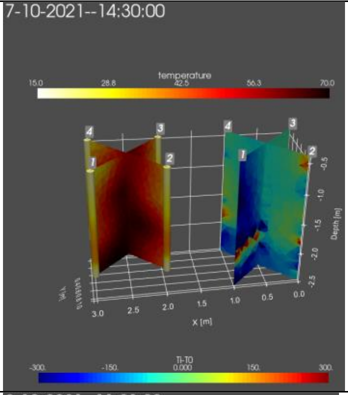
7-10-2021--14:30:00
temperature
15.0 28.8 42.5 56.3 70.0
X [m]
Depth [m]
Ti-T0
-300. -150. 0.000 150. 300.

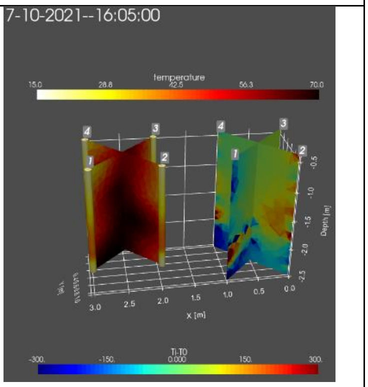
7-10-2021--16:05:00
temperature
15.0 28.8 42.5 56.3 70.0
X [m]
Depth [m]
Ti-T0
-300. -150. 0.000 150. 300.

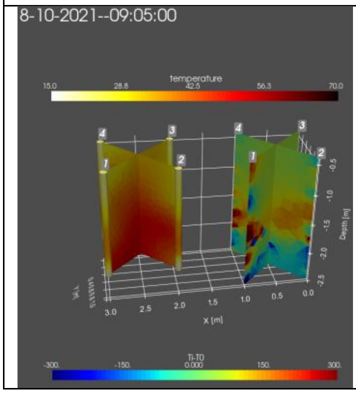
8-10-2021--09:05:00
temperature
15.0 28.8 42.5 56.3 70.0
X [m]
Depth [m]
Ti-T0
-300. -150. 0.000 150. 300.

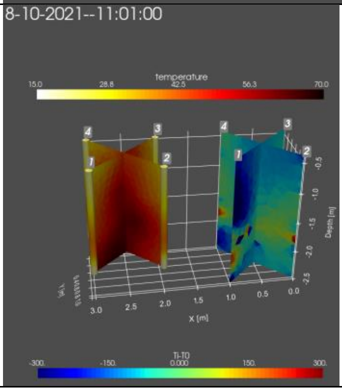
8-10-2021--11:01:00
temperature
15.0 28.8 42.5 56.3 70.0
X [m]
Depth [m]
Ti-T0
-300. -150. 0.000 150. 300.

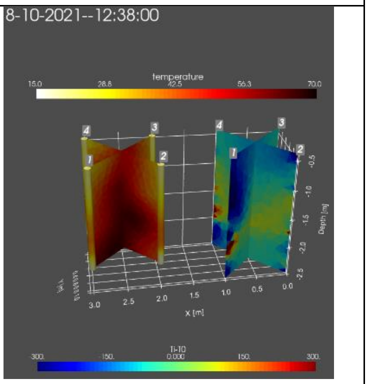
8-10-2021--12:38:00
temperature
15.0 28.8 42.5 56.3 70.0
X [m]
Depth [m]
Ti-T0
-300. -150. 0.000 150. 300.

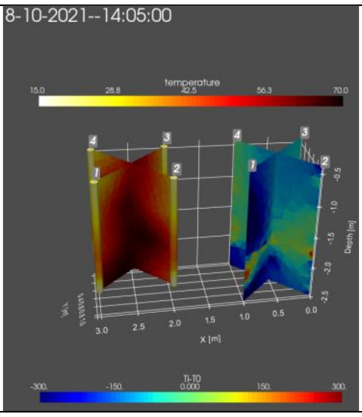
8-10-2021--14:05:00
temperature
15.0 28.8 42.5 56.3 70.0
X [m]
Depth [m]
Ti-T0
-300. -150. 0.000 150. 300.

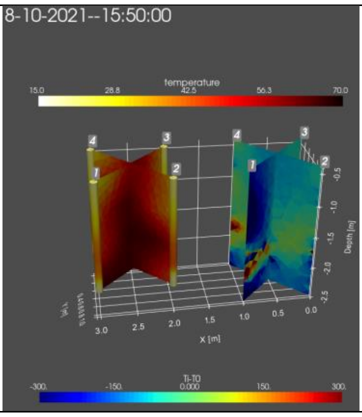
8-10-2021--15:50:00
temperature
15.0 28.8 42.5 56.3 70.0
X [m]
Depth [m]
Ti-T0
-300. -150. 0.000 150. 300.

Appendix B-E Velocity difference respect to T0 of combined sources at depths of -0.6m, -1.0m, -1.4m, and -1.8 m.

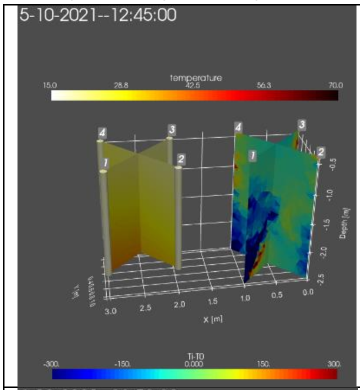

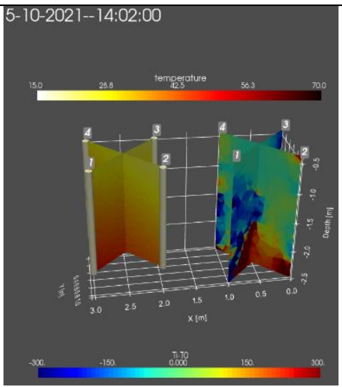

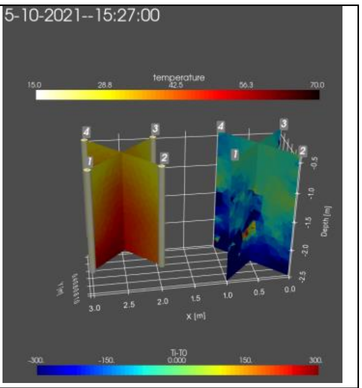

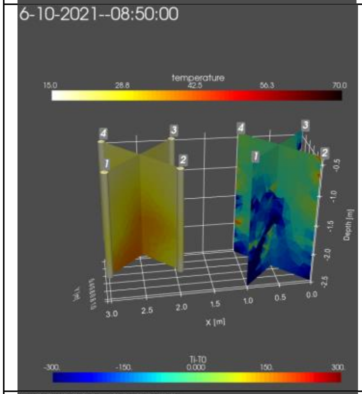

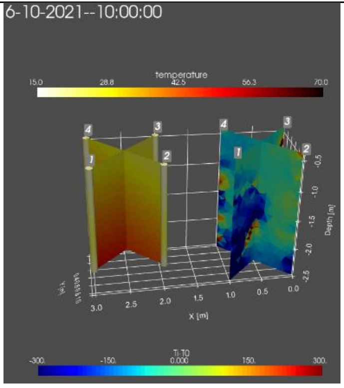

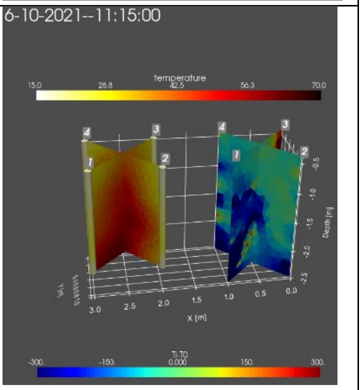

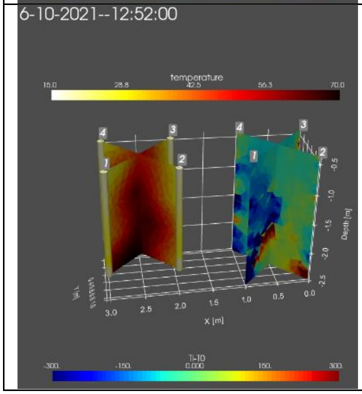

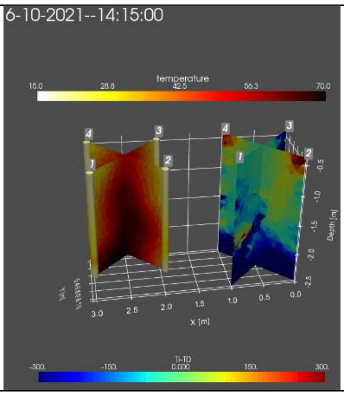

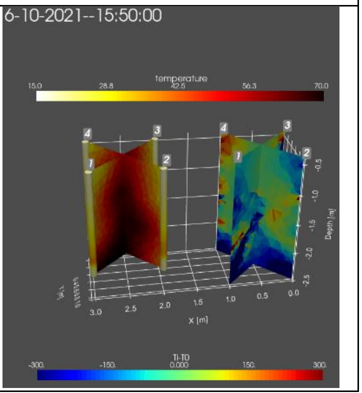

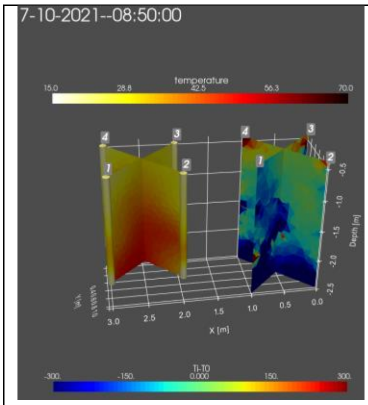
7-10-2021--08:50:00

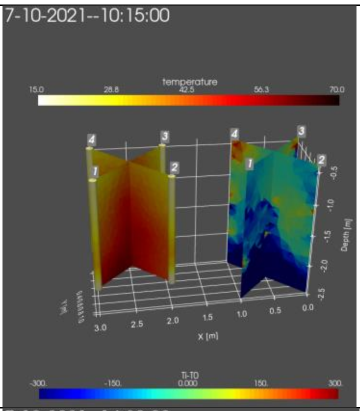
7-10-2021--10:15:00

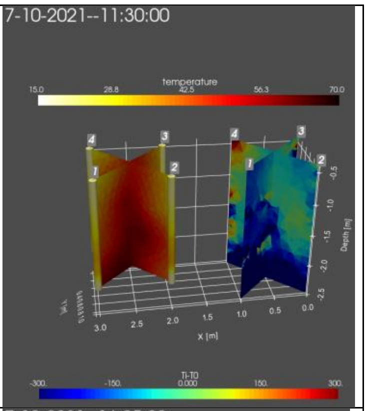
7-10-2021--11:30:00

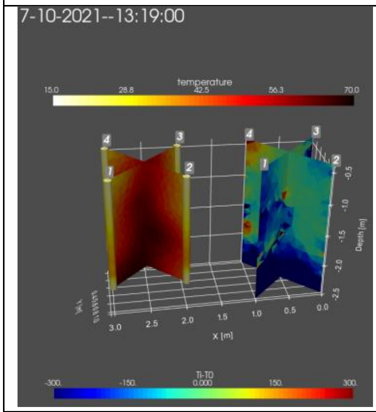
7-10-2021--13:19:00

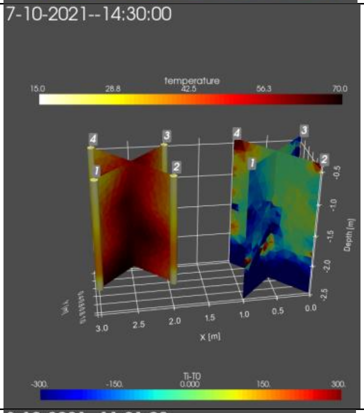
7-10-2021--14:30:00

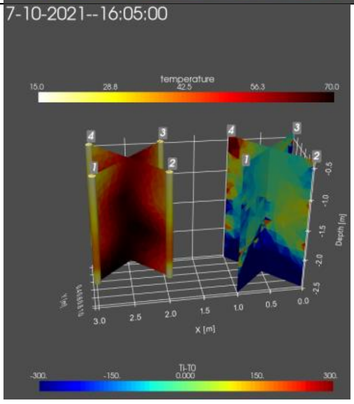
7-10-2021--16:05:00

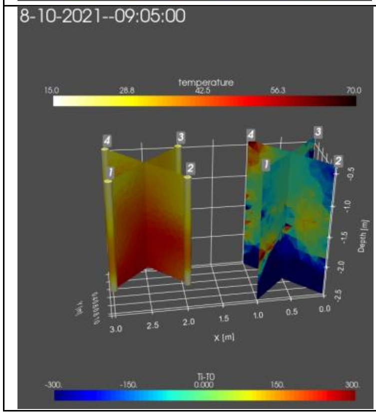
8-10-2021--09:05:00

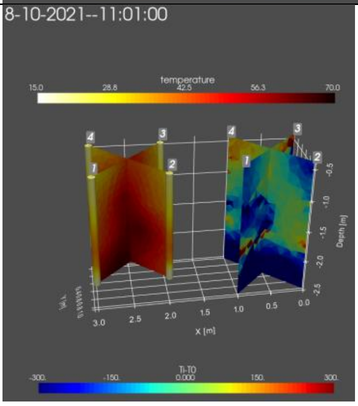
8-10-2021--11:01:00

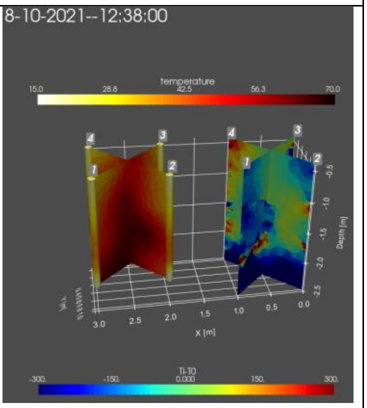
8-10-2021--12:38:00

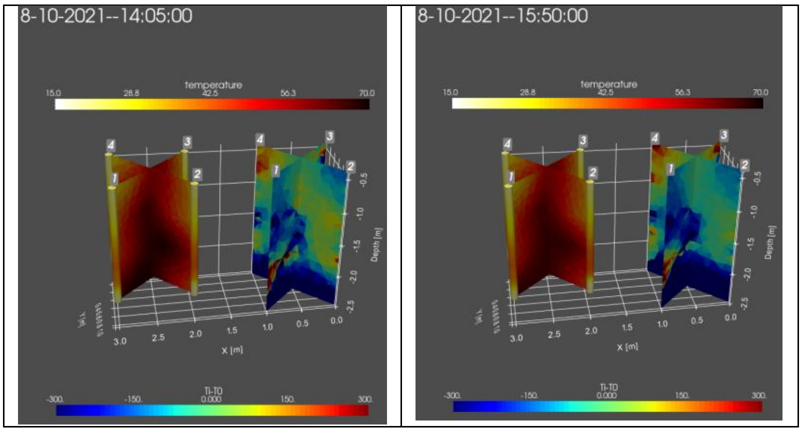

Appendix B-F Recorded shotgathers and picked first arrivals of 10 Hz vertical geophones.

Example of recorded shotgathers per shot position

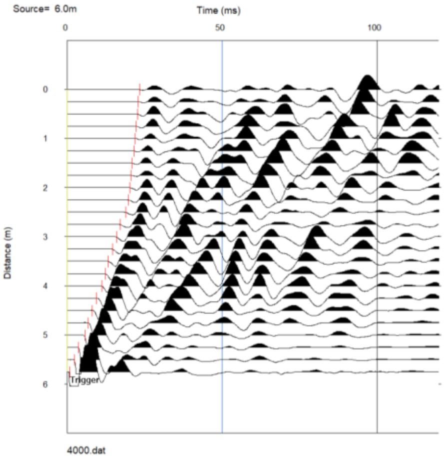

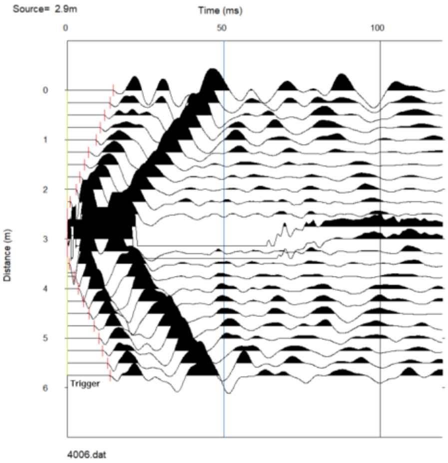

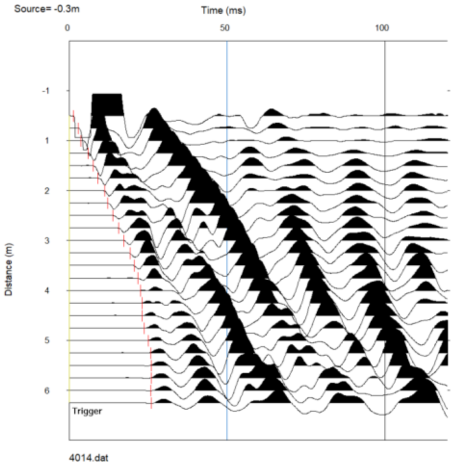

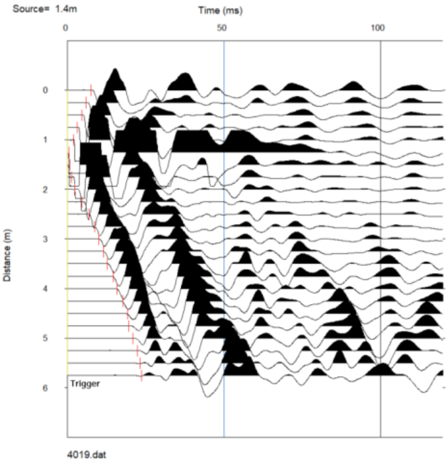

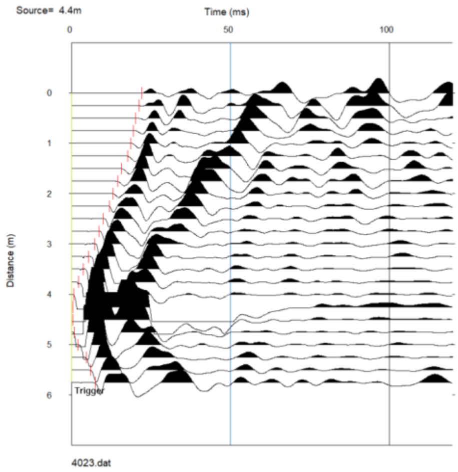

Mean travel times per shot position

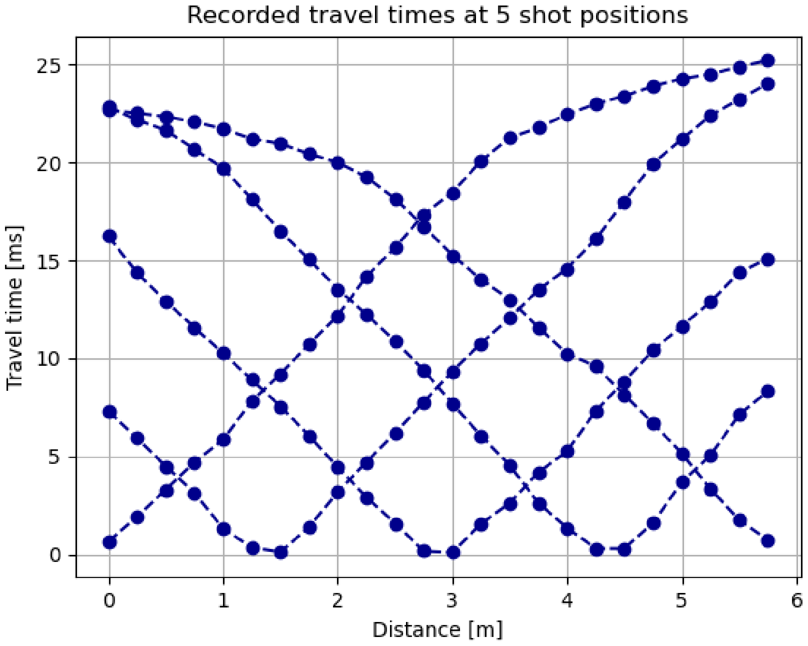

Appendix C: Distributed Temperature Sensing

Mariëlle Koenen[1], Stefan Carpentier[1], Boris Boulenger[1], Dorien Dinkelman[1], Lies Peters[1]
and Wim Bos[2]

[1] TNO, Princetonlaan 6, Utrecht, the Netherlands
[2] ECW energy, Agriport 201, Middenmeer, the netherlands

C1 Introduction

In the Netherlands, more than 2500 low temperature aquifer thermal energy storage systems are operational and because of this, the characteristics and the behaviour of the shallow subsurface to this activity is rather well known. Yet, only a limited number of pilots and field tests on high-temperature aquifer thermal energy storage (HT-ATES) have been successfully developed (Kallesøe et al., 2019). The hydrogeology of the relevant depth interval for HT-ATES (~100-500 m) is poorly known. As a consequence, the thermal properties and hence the thermal evolution during high temperature heat storage needs to be studied. Within the GEOTHERMICA HEATSTORE project, ECW Energy, with support of IF Technology and TNO, has designed and realized the first large scale HT-ATES pilot in the Netherlands. The system was developed within a 23 m thick sand layer of the Maassluis Formation at a depth of ~360-383 m. For research purposes, an extensive monitoring programme was deployed, which provides an exceptional opportunity to evaluate and improve monitoring techniques, and to investigate the impact of cyclic heat storage activities on the subsurface, as well as the technical performance of a full-scale HT-ATES system. In this study we focus on the thermal developments in the subsurface during the first operational year of the HT-ATES system in Middenmeer and distributed temperature sensing as a monitoring technique. Flow measurements and temperature data are evaluated and used for the calibration of a subsurface thermal transport model in ROSIM.

C2 Demonstration case: HT-ATES in Middenmeer

The HT-ATES system in Middenmeer consists of a hot and a cold well at a distance of 220 m, with a monitoring well in between at a distance of 30 m from the hot well (Figure C1). An extensive description of the system can be found in Oerlemans et al. (2022) and Dinkelman et al. (2022). In the summer of 2021 approximately 110,000 m^3 of hot water has been stored at an average temperature of 66.5°C. The injection rate and temperature was highly variable over the total injection period covering 81 days. After a resting phase of 152 days, production started. In the winter of 2022 approximately 80,000 m^3 of water was produced at variable production rates over a period of 52 days, for use in greenhouses. The starting temperature was ~65°C and production was stopped at a temperature of 44°C, resulting in an efficiency in the first year of 27%.

C3 Implementation of DTS cable

Several measuring systems and monitoring technologies have been implemented in the HT-ATES system. Flow meters and temperature gauges at the surface keep track of the amount and temperature of water going in and out of the storage site. A state-of-the-art fibre-optic Distributed Temperature Sensing (DTS) system was installed outside of the well casing of the hot, cold and monitoring wells as shown in Figure C1.

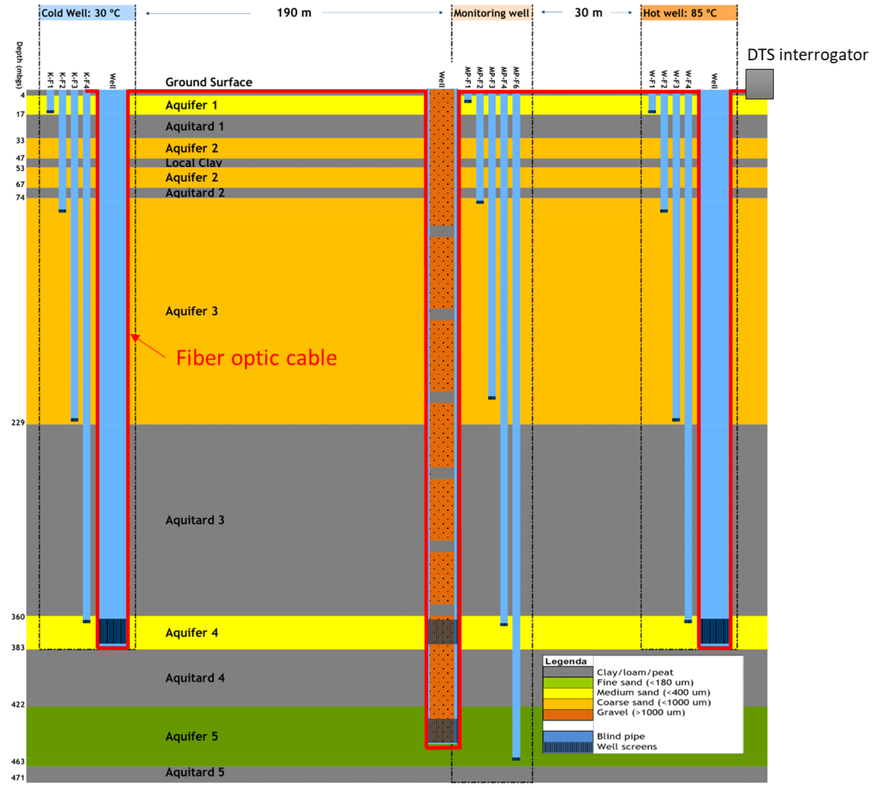

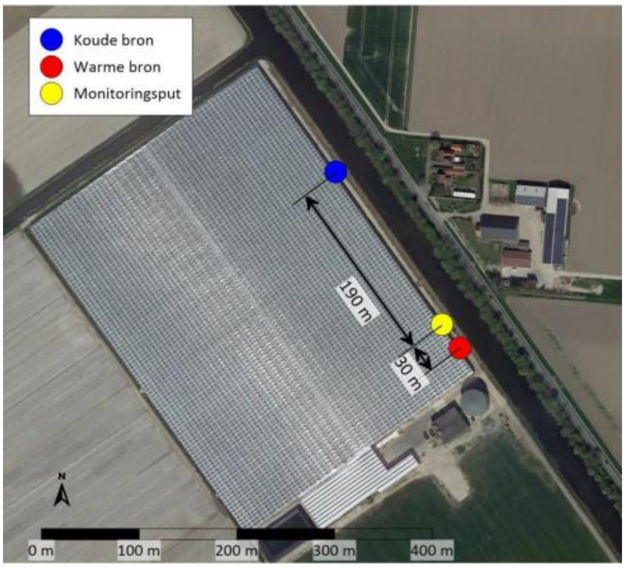

Figure C1 - Upper: Schematic lay-out of DTS cable along the three wells. Modified from Driesner et al. (2021). Lower: Top view of the hot well (red), 'cold' well (blue) and monitoring well (yellow) of the HT-ATES system.

The DTS cable is a single cable spanning all three wells with a total cable length of approximately 2900 m. The cable is connected to a DTS interrogator which takes a temperature measurement every ~2 meters. The DTS cable in the monitoring well reaches a depth of ~450 m, penetrating the aquifer below the storage aquifer (Figure C1). The temperature along the full length of the DTS cable (1450 points) is measured once every ~10 minutes, resulting in approximately 144 measurements per day.

C4 Technical aspects DTS

C4.1 Principle of DTS

DTS is a technique which uses the measuring of backscattered light along a fibre-optic cable to derive temperature profiles. Inventec (Inventec, 2022), who installed the DTS system at ECW Middenmeer, describes the DTS technology as follows: “A reading unit constantly launches a high frequency light pulse of one specific wave length through an optical fiber. The major part of the light exits the fiber at the far end. A small part of the light however is backscattered to the reading unit. This backscattering occurs at every point along the fiber. As a result of photo-acoustic phenomena the backscattered spectrum does not only show the original frequency of the light that is launched into the fiber but contains two additional frequencies: the so-called Brillouin and Raman frequencies. The latter is utilized in DTS: there is a defined relation between the intensity of the Raman frequency and the temperature of the fiber. Measuring the Raman frequency at length intervals of e.g. 1.00 m results in the distributed temperature over the length of the fiber and thus of the object (e.g. a pipe line) to which the fiber is connected or of the medium (e.g. soil) in which the fiber is embedded. The location of each measurement results from measuring the time that has lapsed between launching of the pulse and receipt of the backscattered light (Radar principle – the speed of light is constant).”

Some of the key acquisition parameters for DTS measurements are the gauge length and spatial sampling. The gauge length (for example 10 m) defines the distance along the fiber used in the measurements of the phase differences of the backscattered light. A phase difference measurement provides a single (temperature) point measurement. The spatial sampling (for example 1 m) defines the distance between two consecutives measurements.

C4.2 Depth calibration

The DTS cable is a single cable spanning all three wells from top to bottom and back, and at the surface the cable is buried slightly into the soil or excess cable is winded in the well surface casing. Although the spatial sampling of the measurements is known (~2m) and so are the positions of the point measurements along the fiber, it is not known what are the corresponding depths in the wells. Therefore, to allow depth-based interpretations of the measurement, the downhole DTS data needs a depth calibration which will associate point measurements with depths along the well. This depth calibration is performed by analysing sharp data transitions at the ground surface and at the interface between overburden and aquifer.

At the ground surface, we observe a sharp increase of temperature during winter time when the air temperature can be lower than 0 degrees (Figure 2). More precisely, a significant gap can be observed between two consecutive DTS point measurements. We therefore interpret the second point as the first measurement below ground surface (below 0 m depth).

In fact, as schematically represented in Figure C2, the depth of this first in-well measurement can be between 0 and 2 meters depth due to the 2 m spatial sampling along the fiber. Therefore, this provide depth-calibrated measurements with a depth uncertainty of 2 m. Nevertheless when the first in-well measurement is assumed to be located at 0 m depth, we observe the first hot measurement at 362 m depth during the heat front arrival. This depth highly coincides with the interface between overburden and aquifer as interpretated from well geological data, and tends to confirm the validity of the assumption in achieving a reliable depth calibration.

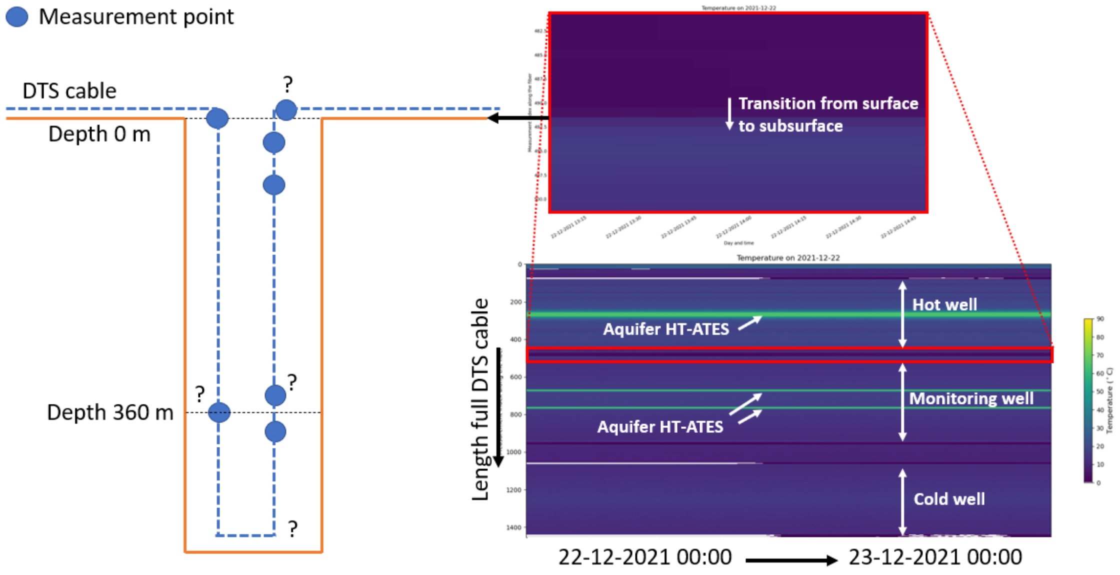

Figure C2 – Left: schematic of the possible depth interpretations. Right: an example of one cold day from which the surface depth can be interpreted by looking at the surface and subsurface temperature transition. Note that the figure on the bottom right shows the full DTS cable along all three wells, going down and up in the hot well (on top), monitoring well (middle) and cold well (bottom).

C4.3 Data processing, visualization and evaluation

The DTS system delivers an enormous amount of time-lapse measurements. Inspection of the data revealed much noise and spikes and detailed evaluation was needed to separate effects which can be explained by physical phenomena from the storage activities and non-physical effects which can only be explained as measurement artefacts. In a first attempt to suppress the artefacts a Savitzky-Golay polynomial filter was applied (Link to Savitzky–Golay filter description). This filtering technique was able to remove the high-frequent outliers. Figure C3 shows the DTS measurements visualized for the monitoring well in time, before and after application of the filtering technique. It can be seen that the sharp time-variant spikes are successfully suppressed, but only by smoothing of the sharp temperature changes. Several features, in the form of value jumps or shifts, remain in the filtered image that are difficult to explain as physical effects. For example, the relatively low temperature interval (second white arrow in Figure C3A) is still present which cannot be related to variations in the injection temperature profile (Figure C4), and the fact that the interval was also observed for the hot and cold well strongly suggests that this was still a sensing artefact. In addition, a low-frequency trend of elevated temperature in the central part of the time series remains.

Therefore, in a second stage, instead of averaging temperature data on a daily basis, we selected manually a single, stable and mostly noise-free temperature profile per day (and only for days for which such profiles can be effectively retrieved). Figure C5 shows that the noise coincides with periods during which flow was zero. Then, the remaining non-physical temperature shifts were quantified by identifying and subtracting a reference noise-free temperature profile. As shown in Figure C6, the DTS data becomes more consistent across time as most of the non-physical features are supressed by subtraction of the estimated artificial temperature shifts. As a result, the DTS temperature history is more reliable for geological interpretation.

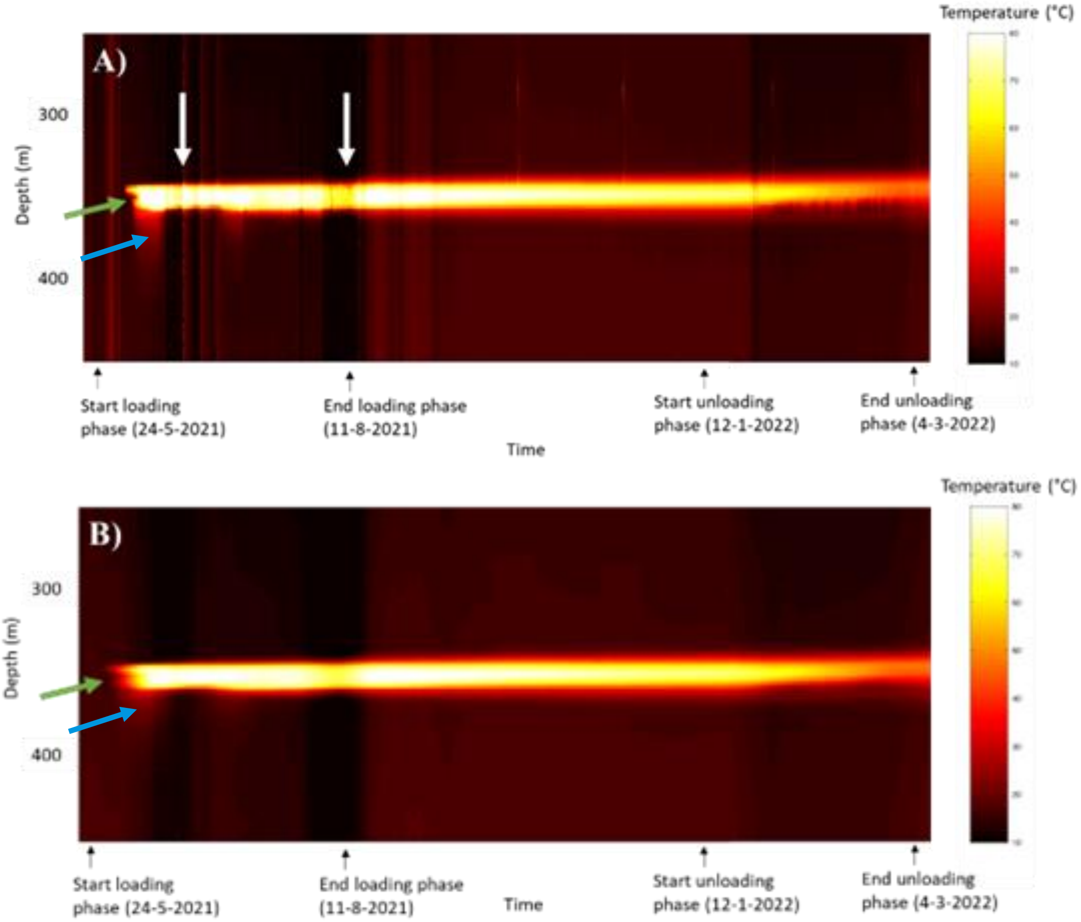

Figure C3 - Timeseries of DTS cable measurements in monitoring well. Y-axis represents the depth interval of 250 – 450 m, X-axis spans the time series from the 19th of May 2021 to the 14th of March 2022. The colour bar ranges from 10°C (black) to 80°C (light yellow). A) The unfiltered time series, with white arrows indicating large temperature spikes B) the Savitzky-Golay filtered time series.

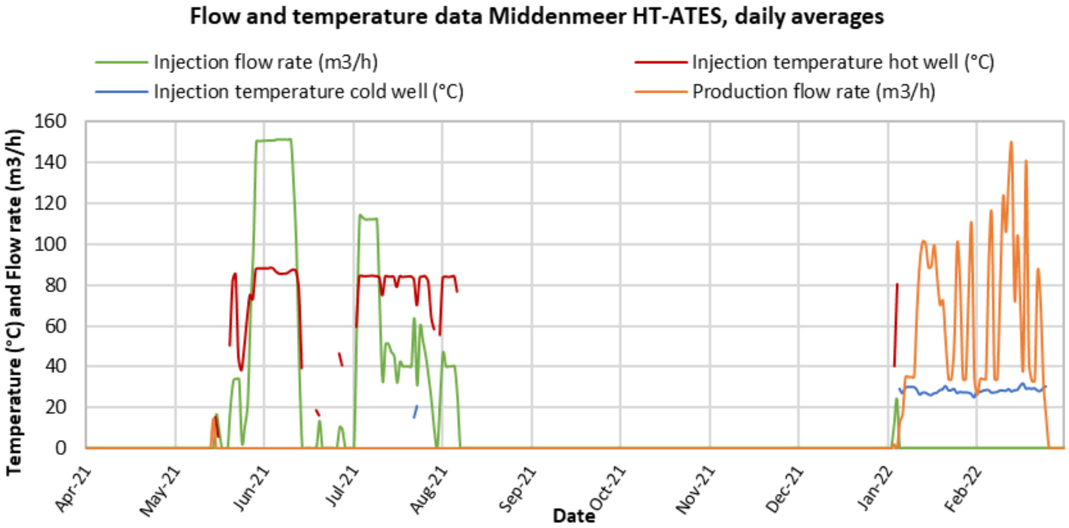

Figure C4 - Daily averages of flow rate and temperature injection data of the hot and cold well at the Middenmeer HT-ATES site.

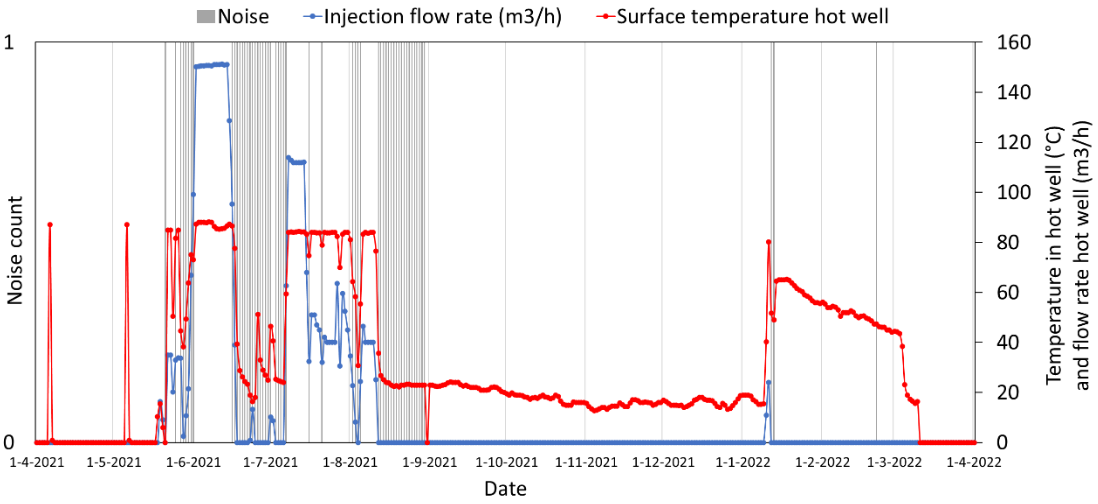

Figure C5 - Manually counted noise as seen in the monitoring well DTS data. Together with the flowrates in the hot well and the temperatures in the hot well. The noise seems to coincide with periods of no flow/shut down of the hot well.

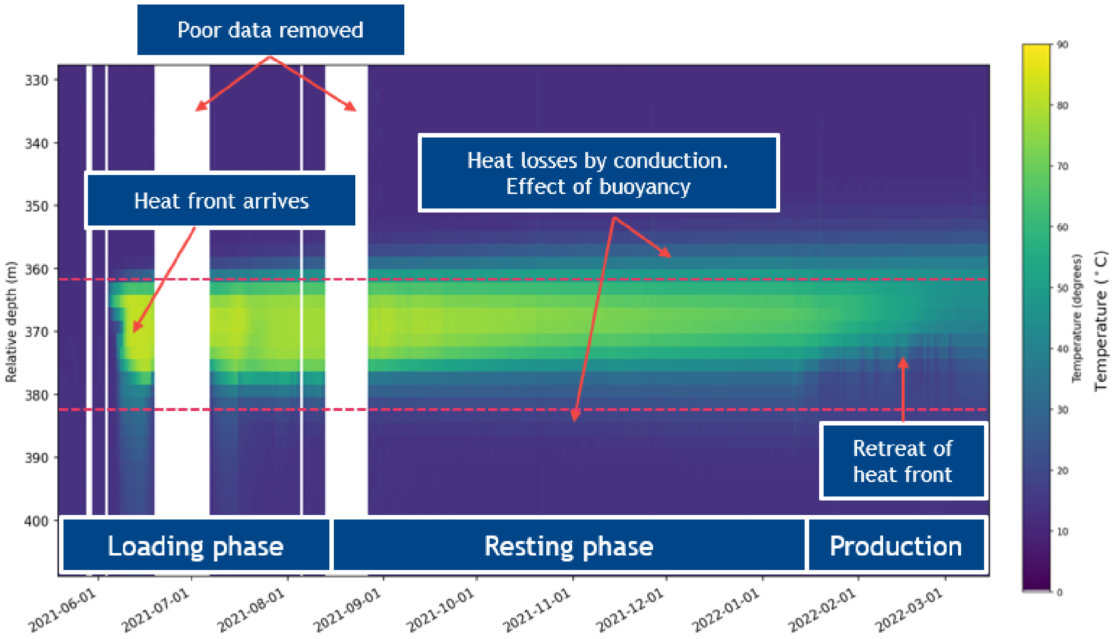

Figure C6. Filtered DTS data with relevant effects during loading, resting and production phases. The dotted lines represent more or less top and bottom of the reservoir, the actual boundaries are not sharp and transition zones between sand and clay cover a few meters.

C5 Thermal evolution

C5.1 Results DTS data

The following physical effects can be observed in the DTS data.

Arrival of the heat front

The thermal front can be seen to arrive at the monitoring well about 10 days after the start of the loading phase (24-5-2021), on 4 June 2021 (the arrival was probably on 3 June 2021 but the data is not available). The front clearly moves faster in the upper part of the aquifer than in the lower part (Figure C6 and Figure C7) which can probably be explained by a combination of higher inflow in the more permeable top of the aquifer and the buoyancy effect. In the middle of the aquifer, at a depth of ~370 m, a thin vertical interval is observed for which the thermal front lags behind (green arrow in Figure C3). This is well visible in the vertical profiles in Figure C7 (red circle). On 10 June, this feature has disappeared (Figure C7). Initially, it was suggested that this could be related to a low permeable layer through which the hot water was flowing more slowly. However, since a similar feature was not observed during the unloading phase at this interval, e.g. a slower cooling, this theory was rejected. Instead, it is thought that the presence of filter cake around the tubing might cause a delay in heating of the fibre optic cable locally. Hence, this delay would not reflect any thermal effect in the reservoir.

Explanations of lag of arrival thermal front:

- (Local) variation in aquifer permeability; flow and conduction through a low permeable layer would be slower. However, a low permeable layer has not be observed on logs and well description. In addition, the effect would be visible in the production period, which is not the case.
- The presence of filter cake or clay pack around the tubing might cause a local delay in heating of the fibre optic cable.

The vertical profiles in Figure C7 show an initial increase in temperature in the bottom part of the reservoir followed by a temperature decrease. This behaviour cannot be explained by a variation in injection temperature. Also, this strong decrease is not observed in the upper part of the reservoir. The time profiles per measurement point along the DTS cable in Figure C8 shows this feature more clearly. The initial temperature increase, suggesting the arrival of the heat front, is only temporary before the temperature goes back to initial values (red circles in Figure C8). One explanation might be vertical flow through the high permeable grout material around and/or within the filter after arrival of the heat front in the upper part of the reservoir, (Figure C7). Injection was temporarily stopped at 18 June, which coincides with the start of the poor DTS data which was removed using the second filtering technique (Figure C6). It seems possible that after injection stopped, the buoyancy reversed the flow direction through the grout material causing cold water to enter the bottom of the grout, thereby representing the actual temperature at this level of the reservoir. Hence, the DTS measurements seem to be compromised temporarily by downward flow through the grout.

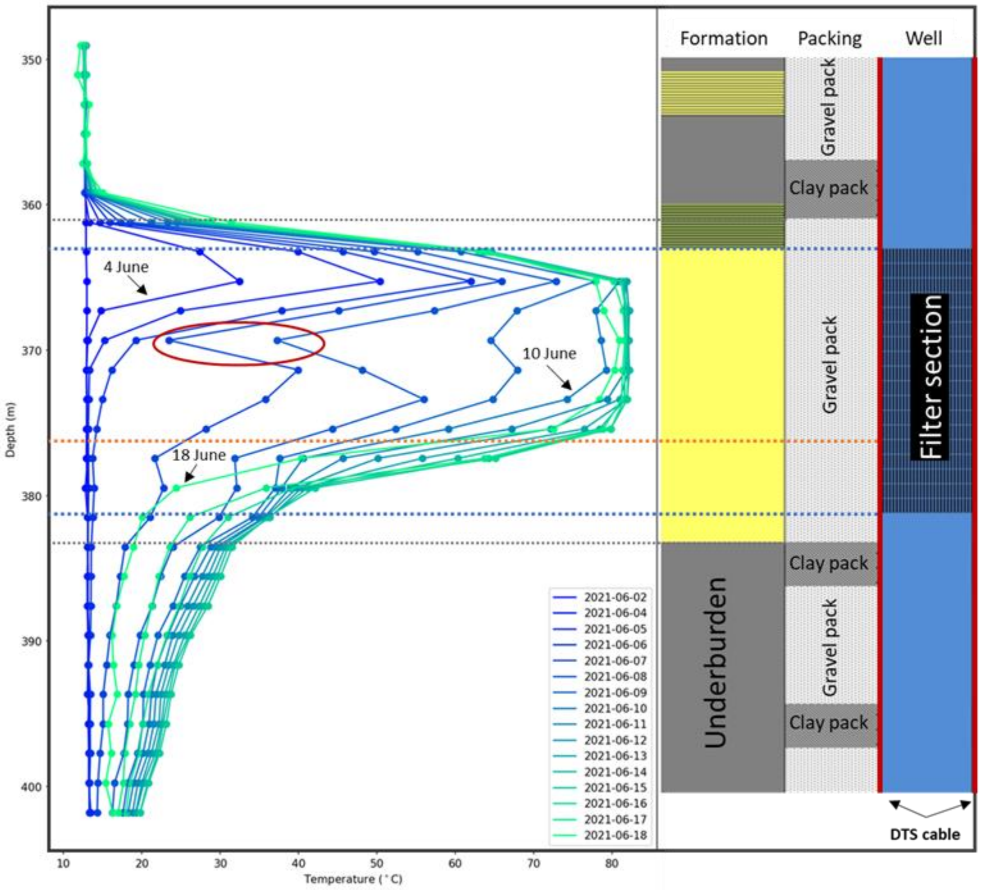

Figure C7. Vertical profiles of the filtered DTS measurements in the monitoring well during the arrival of the heat front and schematic well layout. The grout material (‘omstorting’) consists of highly permeable gravel (light gray) and clay packs (dark grey).

The significant, but temporary, temperature increase *in the underburden* right after arrival of the heat front suggest that something is happening here (blue arrow in Figure C3 and vertical profiles below the lower grey dotted line in Figure C7. Since the effect is temporary, inflow of hot water in the underburden is not obvious. It is suggested that clay swelling takes place, increasing the pressure and therefore the temperature.

Heat dissipation

During the resting phase (11-8-2021 till 12-1-2022) a significant drop in temperature can be observed, primarily in the bottom part of the aquifer. Due to buoyancy the hot water flows upwards and is collected under the overburden. A horizontal component of the heat loss probably the result of both convection and conduction causes spreading of the heat. Heat is lost by conduction to the overburden and to a lesser extent to the underburden.

Retreat of the heat front

During unloading/production (12-1-2022 till 4-3-2022) the thermal front retreats gradually with maximum production temperatures of ~44°C at the end of production. In the bottom part of the aquifer the temperature decreases much faster than in the top, reflecting the buoyancy effect.

Buoyancy

The impact of buoyancy is clearly visible throughout the loading, resting and production phases. The thermal model will demonstrate this further.

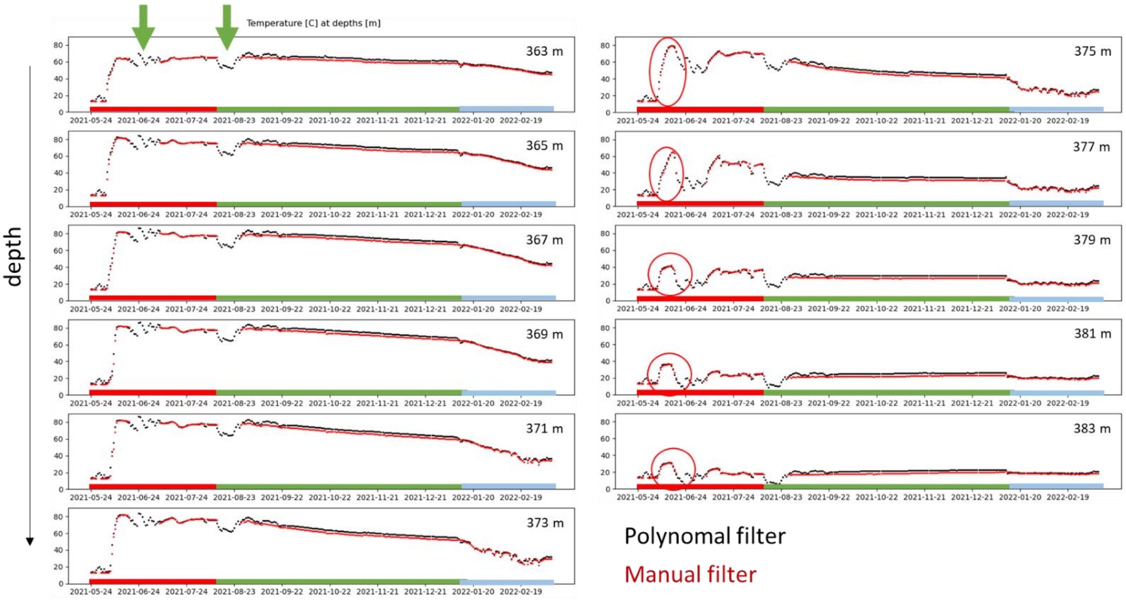

Figure C8. DTS temperature profiles in time for each measurement point along the cable within the reservoir. Black dots: first filtering technique. Red dots: second filtering technique. The red, green and blue timeline intervals represent the loading, resting and production phase respectively. Red circles show high temperatures potentially compromised by downward flow of hot water through the grout material.

C5.2 Model calibration

To analyse the thermal development of the injected and produced heat by the HT-ATES system, thermal flow simulations were performed with ROSIM v0.2[1]. ROSIM v0.2 is a public Microsoft Windows application developed by TNO, containing a workflow for 3D simulation of geothermal production and high-temperature aquifer thermal energy storage. With ROSIM, a static 3D subsurface simulation grid (including grid definition, layer properties and well data) and flow input deck (flow constraints) can be created. The dynamic flow simulation is performed with DoubletCalc3D, an in-house software code developed by TNO, which is a 3-dimensional extension of existing tools for 1D and 2D simulation[2]. It is a dedicated single phase simulator which enables the numerical simulation of temperature and pressure development using temperature dependent density and viscosity. It is based on a staggered coupling of a steady state solution for the pressure and flow field, coupled to a transient solution of the thermal field. The flow and thermal field are solved with a finite volume finite difference formulation (cf. Pluymaekers et al., 2016; Lipsey et al., 2016). For the flow and thermal solution the model has been benchmarked with Eclipse for 2D flow problems (Pluymaekers et al., 2016), for density driven flow the model has been benchmarked for reproducing Rayleigh instability correctly (Lipsey et al., 2016).
The geological model input for ROSIM/DC3D is based on the system design as shown in Figure C1 and well data from the hot, ‘cold’ and monitoring wells. A baseline model was created consisting of a layer cake set-up with homogeneous layers (Table C1). Permeability values were derived from flow tests temperature values were obtained from baseline DTS measurements. The salinity of the aquifer was measured from baseline groundwater analysis. Remaining rock properties were estimated using estimated rock properties.
For the injection profile daily averages of measured flow rate and temperature were used, for the production profile daily averages of the flow rate. The temperature output of the model at the location of the monitoring well has been compared with the DTS data from the monitoring well. The data from the hot and cold wells are not used, as the DTS measurements are influenced by the water flowing through the well pipes. To ‘fit’ the thermal model to the DTS data from the

monitoring well, several subsurface parameters from the baseline model were adapted. Model calibration was first done manually by changing parameters based on expert opinion and using the DTS data from the first filtering technique. Subsequently a history match was performed using the DTS data processed by the second filtering technique.

The results of the baseline geological model simulations are shown in Figure C9. The buoyancy effect is clearly visible in the cone shape of the hot plume. Also the heat dissipation during the resting phase is clear by the lower temperatures at the end of the rest phase.

Table C1 Geological input parameters baseline model. Based on: Driesner et al. (2021); Diaz-Maurin & Saaltink eds. (2021).

Layer name	Base depth	Thickness	Perm x y	Perm z	Temperature	Salinity	Porosity	Rock matrix conductivity
	mbgl	m	mD	mD	°C	ppm	-	W/mK
aquitard	360	12	13	1	16.0	17478	0.45	4.43
aquifer	383	23	16847	5611	16.3	18569	0.37	5.35
aquitard	395	12	13	1	16.6	20894	0.43	4.11

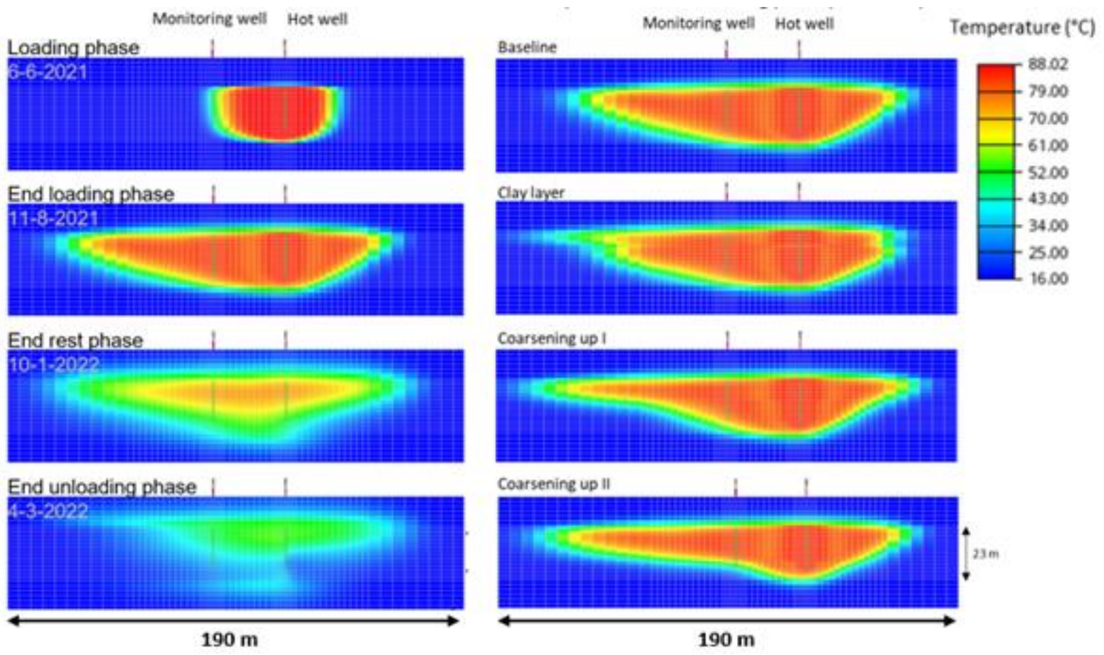

Figure C9 – Left: Vertical profiles of the baseline scenario model results over time. Right: Vertical profiles at the end of the loading phase for the four scenarios.

Comparison of the vertical temperature profiles between model and DTS data (Figure C8) shows that the arrival of the heat front as well as the buoyancy effect are highly underestimated in the baseline model. Also, the delayed arrival of the heat front at a depth of ~370 m was not simulated.

Aiming to calibrate the thermal transport model manually, the following simulations have been performed with adaptations to the baseline scenario parameters:

- *Baseline*: this scenario used the homogenous model input as shown in Table C1.
- *Clay layer*: A 'clay layer' at 369 m depth with a horizontal hydraulic conductivity of 0.1 m/d (corresponding to ~0.13 Darcy permeability) is implemented in the baseline model. The upper part, above the clay layer, is given a higher horizontal hydraulic conductivity of 20 m/d (~27 Darcy) relative to the baseline value of 12.7 m/d (~17 Darcy).

- *Coarsening up I*: The upper part, from 361-370 m depth is given a higher horizontal hydraulic conductivity of 20 m/d (~27 Darcy), while the lower part remains 12.7 m/d (~17 Darcy).
- *Coarsening up II*: The lower 8 m of the aquifer is given a lower hydraulic conductivity value of 3 m/d (~4 Darcy) whereas the upper part keeps its 'original' value of 12.7 m/d.

Comparison of the vertical temperature profiles in Figure C10 shows that the scenario with the clay layer is able to simulate the delayed arrival of the heat front. Yet, the feature remains much longer visible than in the DTS data (see Figure C10 at 12-6-2022 and 20-6-2022). Also, the model creates a similar feature during the production phase which was not observed in the DTS data (see Figure C10 at 4-3-2022). The coarsening up I scenario is able to simulate the vertical difference in arrival of the heat front much better than the baseline scenario, whereas the coarsening up II scenario is able to simulate the retreat of the heat front much better. Figure C9 shows the differences in shape of the thermal plume for the four scenarios which is an important factor for the efficiency of the system, signifying the importance of understanding the subsurface characteristics and the thermal evolution.

None of the scenarios can simulate the DTS data with satisfactory similarity. In order to improve the match between model results and DTS data, and improve the knowledge of the subsurface properties and corresponding behaviour during heat storage at Middenmeer specifically and for the relevant depth interval in general, a history matching workflow was developed and applied in an additional project. For this purpose, the TNO history match software ERT was coupled to ROSIM. The workflow involves the creation of an initial model ensemble with 100 geological realizations based on the baseline layer cake model, using a range for rock properties per layer in the model. In other words, 100 models are created with for each reservoir and over- and underburden layer, a random selection of rock properties is taken within the ranges defined based on literature and expert opinion. The history matching calculates in several iterations the models which match the DTS data best. Details on the methodology and results will be published in the coming year.

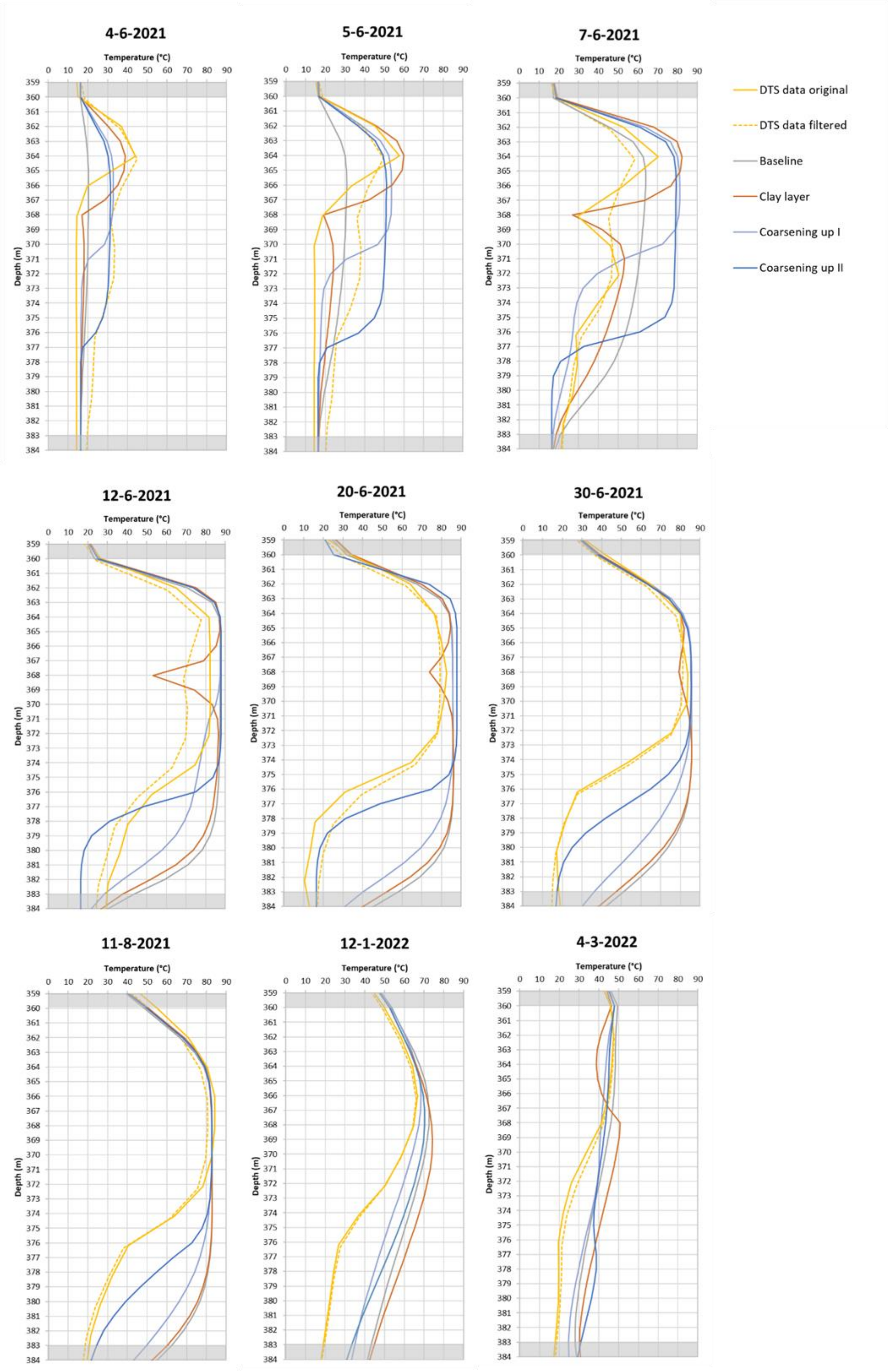

Figure C10 - Comparison of the DTS data (original and filtered) temperature profiles over depth with four different model scenario results: baseline, coarsening up I & II and clay layer.

C6 Evaluation of DTS as monitoring technique

DTS is an existing, proven technology to perform temperature measurements in the subsurface and can deliver continuous, high frequent temperature measurements which are essential for obtaining insight in subsurface processes during high temperature heat storage. By visualization of the DTS measurements in the monitoring well in Middenmeer the relevant processes of the thermal evolution, such as the passing of the thermal front during injection and production, the upward flow of hot water due to buoyancy, and the heating of over- and underlying clay layers could be observed. However, the DTS monitoring data by itself cannot be used to monitor the spreading of the heat within the storage aquifer in a detailed 2D view, unless several monitoring wells with DTS cables are installed in a strategic set-up to follow the thermal front in time. Such an approach was applied to the heat storage site in Koppert-Cress, the Netherlands, where four monitoring wells are present at increasing distance from the hot wells (Diaz-Maurin and Saaltink, 2021). Their system was at a much smaller scale and at a shallower depth. For high-temperature storage at greater depth, such an approach would be too expensive. The combination of DTS measurements in a single monitoring well with thermal model calibration, as reported here, presents a powerful tool to evaluate the thermal evolution within the storage aquifer as well as the heat loss to over- and underburden. Model calibration by means of history matching is even more powerful.

Yet, several challenges have been found in the Middenmeer case study. The installation of the cable should be done with care to prevent the formation of a technical flaw (kink) in the cable, as occurred during installation in Middenmeer. A lot of noise, spikes, and periods with poor measurements could be observed in the data, (part of) which could be the result of this kink in the cable. Post-processing of the data was required to obtain a more reliable data set. In addition to the artefacts in the measurements, unexpected observations interpreted as physical effects complicate the evaluation of the thermal evolution. The fast and temporary temperature increase in the bottom part of the reservoir is interpreted as vertical flow of hot water through the gravel pack outside and within the tubing rather than representing the actual progress of the thermal front. The DTS measurements would represent the progress of the thermal front most accurately when embedded in material which is highly similar to the actual sediment in the subsurface. Currently, a monitoring well for a HT-ATES system is developed as a test drilling, requiring high permeable gravel pack to perform flow tests. For future HT-ATES systems, it would be good to think about a more dedicated monitoring well with DTS cable embedded in less permeable material. Some thermal simulators, such as Eclipse, are capable of simulating cross flow along the well. The DoubletCalc3D simulator that was used in this study, is currently not capable of simulating this effect. For the history match, a work around was created by increasing the uncertainty at the specific depth interval during the injection phase.
Temperature increases in the underburden might be caused by clay swelling in the underburden layer or in the clay pack around the tubing. This effect cannot be included in thermal simulations. Additional studies are needed to confirm that clay swelling is the actual cause of temperature increases in the underburden.

C7 Practical aspects DTS

The following general practical aspects of DTS can be mentioned:

1. Installation of a DTS system is a precarious matter and needs careful thinking and execution. Once damage is done to a DTS system, mostly the fibre optic cable, then repairing the damage is extremely difficult, if not impossible. Proven installation

procedures are required by certified fibre-optical engineers to prevent occurrences of for example a kink in the fibre-optic cable.

2. The costs for different types of cables vary significantly. There are state-of-the-art, cream-of-the-crop cables with enhanced fibre-optic properties that deliver superior signal-to-noise ratio of fibre-optic measurements which come at a higher price. But in practice for DTS measurements more simple and cost-effective cables are sufficient as DTS constitutes a relatively simple measurement at low-frequency sampling rate.
3. The vertical resolution of DTS ranges from several meters to several centimeters, depending on the sample rate in time, the amount of available data storage, the required detection threshold etc.

C8 References

Diaz-Maurin F., and Saaltink M.W. (2021). Model validation for subsurface dynamics. GEOTHERMICA – ERA NET Cofund Geothermal. HEATSTORE deliverable D5.3, 110 p.

Dinkelman D., Carpentier S., Koenen M., Oerlemans P., Godschalk B., Peters E., Bos W., Vrijlandt M. and van Wees J-D. (2022). High temperature aquifer thermal energy storage performance in Middenmeer, the Netherlands: thermal monitoring and model calibration. European Geothermal Congress 2022.

Driesner, T. et al.: Final report on tools and workflows for simulating subsurface dynamic of different types of High Temperature Underground Thermal Energy Storage. GEOTHERMICA – ERA NET Cofund Geothermal. HEATSTORE deliverable D2.1 (2021), 335p.

Hazen, A. (1892) Some Physical Properties of Sands and Gravels, with Special Reference to Their Use in Filtration. 24th Annual Report, Massachusetts State Board of Health, 539-556.

Inventec, 2022. https://www.inventec.nl/Portals/0/ProductsheetsUK/DTS%20engels.pdf

Kallesøe, A.J. et al.: Underground Thermal Energy Storage (UTES) – state-of-the-art, example cases and lessons learned. GEOTHERMICA – ERA NET Cofund Geothermal. HEATSTORE deliverable D1.1 (2019), 208p.

Oerlemans P., Drijver B., Koenen M., Koornneef J., Dinkelman D., Bos W. and Godschalk B. (2022). First field results on the technical risks and effectiveness of mitigation measures for the full scale HT-ATES demonstration project in Middenmeer. European Geothermal Congress 2022.

Appendix D – Pulse testing

Peter A. Fokker[1], Dario Viberti[2], Eloisa Salina Borello[2], Francesca Verga[2], Jan-Diederik van Wees[1], Arjan Konijn[3], Wim Bos[3], Mariëlle Koenen[1]

[1] TNO, Princetonlaan 6, Utrecht, the Netherlands
[2] University of Turin, Giuseppe Verdi, 8, 10124 Torino TO, Italië
[3] ECW energy, Agriport 201, Middenmeer, the netherlands

D1 Introduction

Pulse testing has recently been demonstrated in a theoretical model study to have potential for the identification of temperature and thermal radius of cooled or heated zones (Fokker et al, 2021). This potential is related to the large contrast in mobility between water of different temperature, and the development of zones of altered temperature around an injector well.

This report shows the results of pulse testing in the High-Temperature Aquifer Thermal Energy Storage (HT-ATES) system in Middenmeer. The application was in a shallow high-temperature heat storage system, where a baseline test was run prior to storing the heat, a monitoring test after 5 days of injection and a post-loading monitoring test after 6 months of injection.

After a brief description of the system and the test setup we will present the test results. Two particular features of the post-loading monitoring test are the non-constant injection temperature and the interference with the producer which was subject to the same pulse. For the interference, a first approach of handling it in the analysis is proposed. For the temperature, a periodical temperature variation had been present in the test with the same periodicity as the injection rate pulses. In a separate document we have outlined how the disturbance due to these variations can be calculated and corrected for, and possibly be used as additional information. The new knowledge was thus applied here to this field test.

We close this report with a summary of the findings obtained and their implications, and the possibilities, impossibilities and challenges of pulse testing for thermal front monitoring.

D2 Demonstration case: HT-ATES in Middenmeer

D2.1 Pulse test set-up

The injection well consists of a 400 mm ID casing down to 180 m depth, below that a 300 mm ID casing to the injection depth of 370 m. In the upper part of the casing a 170 mm tubing reaches down to about 130 m. Inside the tubing, four injection tubings reach to depths of 29, 29, 35 and 47 m. Injection took place in one of the two shortest tubings; pressures were recorded in all four, of which we only used the ones without flow. This had the advantage that frictional losses in the injection tubing were excluded. Still, corrections due to the hydraulic head in the complete well and friction in the part below the bottom of the monitoring tubes still needed to be calculated and corrected for.

The pulse tests were designed such that high and low rate alternated in a cyclical fashion. Switching from high to low rate and back was automated and took place during a short time of 10 seconds.

Injection was through one of the two short tubings, allowing the fluid to enter the wellbore. Pressure monitoring was performed in the 3 remaining tubings.

Injection and production were always balanced. As a result, the production from the “cold well”, 200 m away from the injection well, was also alternated. This has effect on the pressure response in the injector well, as will be demonstrated later.

The baseline investigation in May 2021 comprised two pulse tests, with 6 pulses of 2x10-minute duration and 7 pulses of 2x1-hour. After 5 days, when approximately 3600 m^3 of hot water had been injected, a test with 5 pulses of 2x2-hours was performed. Some propagation of the heat front was expected for this third test. After heat loading, one test with 6 four-hour pulses of 93 minutes higher and 147 minutes lower injection rates was performed in January 2022. With the uneven time distribution between higher and lower rates more Fourier components in the frequency spectrum were expected. The rates and pressures versus time are represented in Figure D1.

A peculiar and unexpected feature of the pressure development for the post-loading test is that some time after the moment of switching the growth (for increased rate) and decline (for decreased rate) change into decline and growth, respectively. We found that this behaviour correlated to temperature variations, which appeared to also have happened during this test. A representation of the temperature at the wellbore and at the position of the pump at 135 m depth is provided in Figure D2. The travel time and the cooling of the water during its travel downward causes the delay and the temperature difference between the signal at the wellbore and at the pumps.

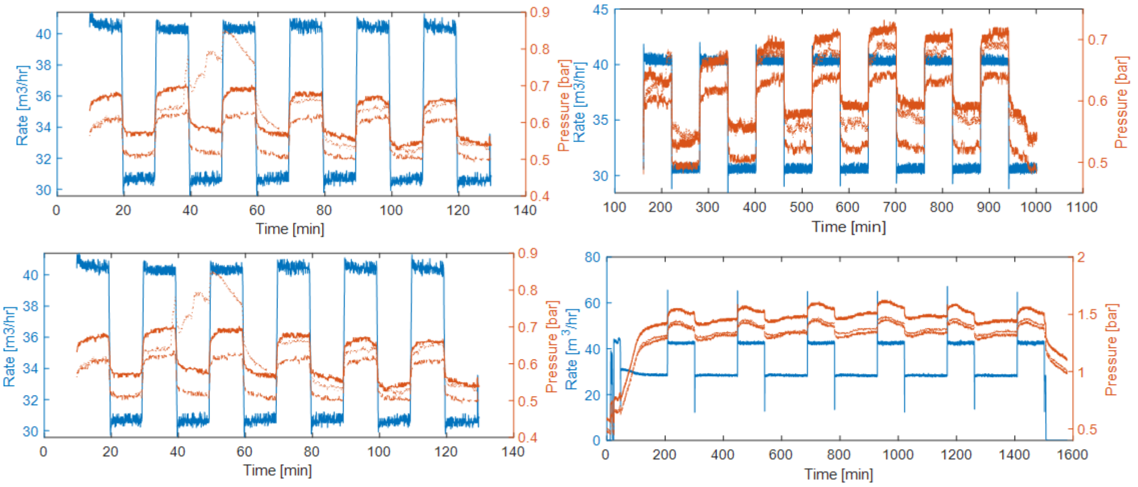

Figure D1 – Injection rates and resulting pressures for the baseline pulse tests in the heat storage system: (a) baseline with six pulses of 2x10 min, (b) baseline with 7 pulses of 2x1-hour (c) test after 5 days of loading with 5 pulses of 2x2-hours. (d) post-loading test with 6 pulses of 93+147 minutes. For each test, pressure traces P1, P2 and P3 are compared.

D2.2 Pressure and Temperature Corrections

D2.2.1 Synchronisation

When zooming in on the rate and pressure traces, we observe a synchronization issue. Upon switching the rate, the pressure starts to react about 6 sec before the rate change. While small with respect to the total pulse time, the effect on the phase delay and the amplitude derivative is sizeable for the larger frequencies. We have therefore corrected for this phase delay.

D2.2.2 Along-well pressure corrections

We need to have representative values for the injection pressure at the entrance point of the reservoir, i.e. at the perforations. This requires adaptation of the measured pressures though addition of the hydraulic head and subtraction of frictional pressure losses.

The frictional pressure losses must be calculated between the bottom of the monitoring tubes and the depth of injection. The largest contribution originates from the 75 m flow length through the 170 mm tubing – for the injection rates employed in these tests the friction is less than a few kPa. The friction in the lower parts of the well is even smaller and we conclude that friction can be neglected. If we had had to use the pressure measurements in the injection tubing this would not have been the case: the much smaller diameter of that tubing results in several bars of frictional pressure losses.

The hydraulic head that acts between the top of the well and the depth of injection depends directly on the weight of the water column. The compressibility of water is low, about $5*10^{-10}$ Pa^{-1}. With the pressure variations of the order of 0.1 – 0.2 bar the associated change in hydraulic head is therefore in the order of 10^{-5} of the total of around 40 bar, or 40 Pa. This is also negligible.

The remaining correction is the dependence of hydraulic head on the temperature. Indeed, the temperature dependence of the water density is considerable; we have put the measured properties in Table D2. Therefore, we need to know the temperature in the well as a function of depth and time.

Table D2 – Temperature-dependent properties of injected brine (salinity 11000 mg/l)

Temperature [°C]	Density [kg/m^3]	Viscosity [mPa.s]
30	1008	0.817
50	1002	0.568
85	985	0.354

For the baseline pulse test and the test after 5 days of injection the injection temperatures were constant. Therefore no time-dependent hydraulic head needed to be calculated. This was different for the post-loading test, where considerable variations in injection water temperatures appeared. The following correction has therefore been performed for the post-loading test only.

The time-dependent temperature distribution along the wellbore is controlled by the movement downward of the injected water and the thermal losses to the well surroundings. The thermal losses to the surroundings can be estimated through the temperature development at a fixed point when the fluid is stagnant. This is the case, for instance, after completion of the test: after shut-in, later than 1500 minutes after starting the test, the temperature at the pump at 135 m depth is well approximated by using an exponential decay toward the ambient temperature:

$$\frac{dT}{dt} = -v_c \cdot \left(T - T_{eq}\right) \tag{1}$$

with $T_{eq} = 20°\text{C}$ and $v_c = 0.0015/\text{min}$.

To obtain the temperature profile at all times we follow every volume element of fluid on its way into the well. The linear velocity is calculated using the volumetric flow rate and the inner diameter of the tubing or casing through which it flows, at every position. For the thermal leakage, we assume the same functional relationship as in Eq. (1). This profile can then be used at every time to calculate the density profile. Integrating the density profile and multiplying with the gravitational acceleration constant yield the hydraulic head.

Figure 12 (left) presents the measured temperatures in the system and the calculated temperatures at the perforations and at the wellhead. It also provides a comparison with the temperature measured with the Distributed Temperature Sensor (see the previous Chapter)[3] and at the wellhead. The agreement at the perforations is good (the DTS data had not sufficient temporal resolution to be used for the present analysis though). At the wellhead, it is not good. Apparently the complicated tubing scheme with the four tubings and the stagnant fluid in the tubings where the measurements are taken break down the applicability of the simple correlation stated above (Eq. (1)). The temperature above the pump had been assumed to follow the same behaviour as below it; this is not correct for the stagnant water columns in the measurement tubings: they are not in thermal equilibrium with the injection tubing.

The pressures in tubing P3, along with the corrections for the hydraulic head variations and the friction, and the corrected pressures in P3, are given in Figure D2 (right). We observe that the anomalous behaviour of the pressure has not been removed. This is presumably also related to the erroneous correction for hydraulic head above the temperature measurement point of 135 m. Pressure measurements bottomhole would have precluded these complications; pressure measurements at the pump location in the flowing part of the well would possibly have alleviated it.

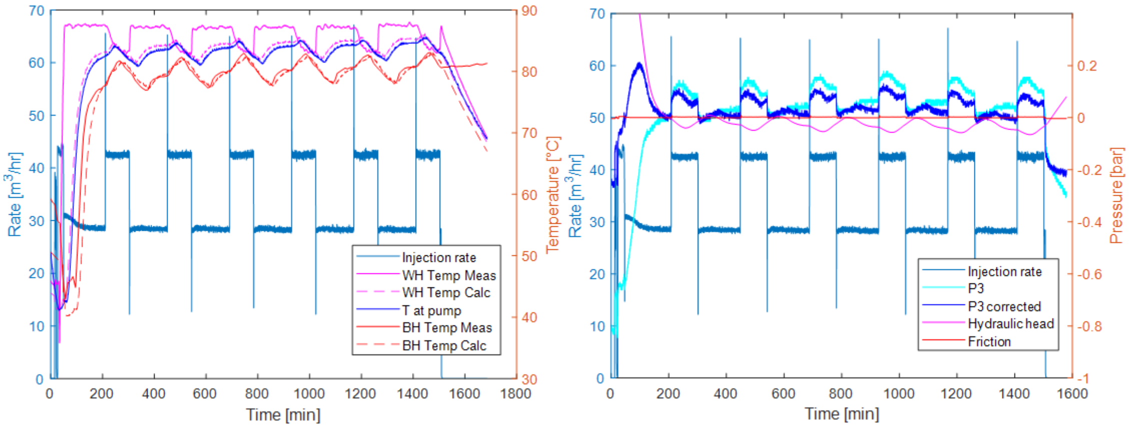

Figure D2 – Original and corrected data for the post-loading test. Left: Injection rates and temperatures vs time. Temperatures are given as measured and calculated at the wellhead, measured at the pumps at 135 m depth, as calculated bottomhole and as measured bottomhole with the distributed temperature sensor. Right: Injection rates, pressures in tubing 3; corrections due to temperature and rate, and corrected pressures in tubing 3 vs time. Pressures are given with respect to their value 200 min after the start.

D2.2.3 Interference with the cold well

The HTO system in Middenmeer consists of a hot well, a cold well, and a monitoring well (Figure D3). The monitoring well is used for measurements only, no fluids are injected or produced. The cold well and the hot well are 220 m apart. During loading, cold fluid is produced from the cold well, heated, and re-injected into the hot well. Upon unloading, hot fluid is produced from the hot

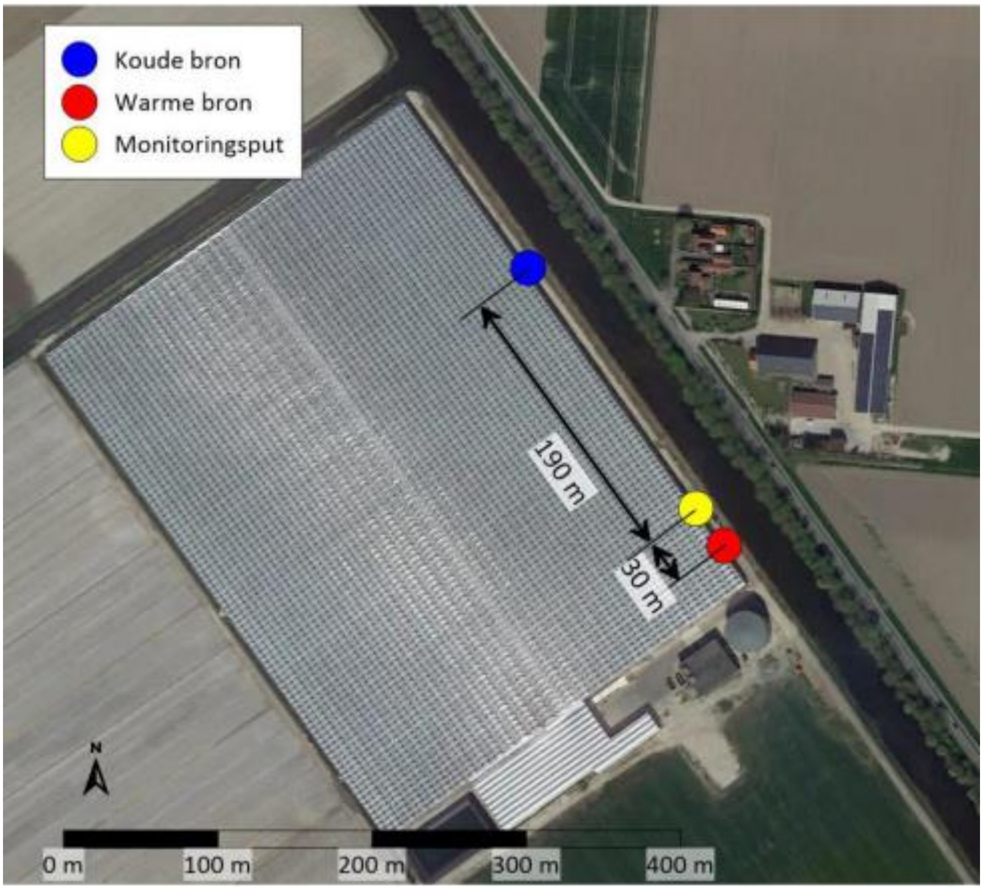

Figure D3 – Surface locations of the hot well, the cold well and the monitoring well.

well, cooled, and re-injected into the cold well. The injection rate is equal to the production rate: no surface storage is employed. This setup introduces interference between the two wells. As a first estimate, the reservoir pressure distortion after changing the well rate moves into the reservoir at an areal speed $\frac{dA}{dt} = 2.25 \cdot \pi \kappa t$ with $\kappa = \frac{k}{\phi \mu c}$, or $r = 1.5 \cdot \sqrt{\kappa t}$. With the very high permeability (order 5 darcy) and the cold-water viscosity of 1 cp, this means the hot well starts to see pressure distortions induced by changes in the cold well production rates after 5 minutes. The rate changes in the cold well cannot be discarded in the analysis of the hot well pulse tests.

To underline this qualitative assessment we ran a numerical simulation in Eclipse with both the injector and producer well, considering thermal effects and using a fine grid around the wells. A homogeneous reservoir of 5 Darcy permeability was considered, and a prelaminar injection history of 8 months, corresponding to a 60 m thermal radius, was imposed. We employed an injection scheme for the post-loading test of 7 cycles of high and low rates, and calculated the pressure response. Two scenarios were run to underline the interference effect: one with equally pulsed injection and production rate, and one with pulsed injection rate but a constant average production rate. Figure D4 makes clear that indeed a considerable amount of interference occurs.

Figure D5 shows the frequency response of the two synthetic tests. It is clear that application of the theory as derived for a radially symmetric reservoir around an injector, discarding the influence of the pulses in the producer, is incorrect. Still, for the frequency analysis, the two responses are very similar up to periods of 25 minutes. This is unexpected in view of the vastly different time traces, and it gives hope for a sensible frequency analysis with the shorter pulses.

An alternative approach is to create an approximate correction to the theoretical response. As an interference term we added to the response in the hot well the response of a pulsed producer in a homogeneous (cold) aquifer at the position of the injector. The intuition behind this choice is that from the viewpoint of the cold well the hot-fluid bell is a distortion of the further homogeneous aquifer. Figure D5 demonstrates that this approach gives very acceptable agreement between the output of the synthetic test and the theory. The thermal radius of 60 m is indeed the radius that gives the best match.

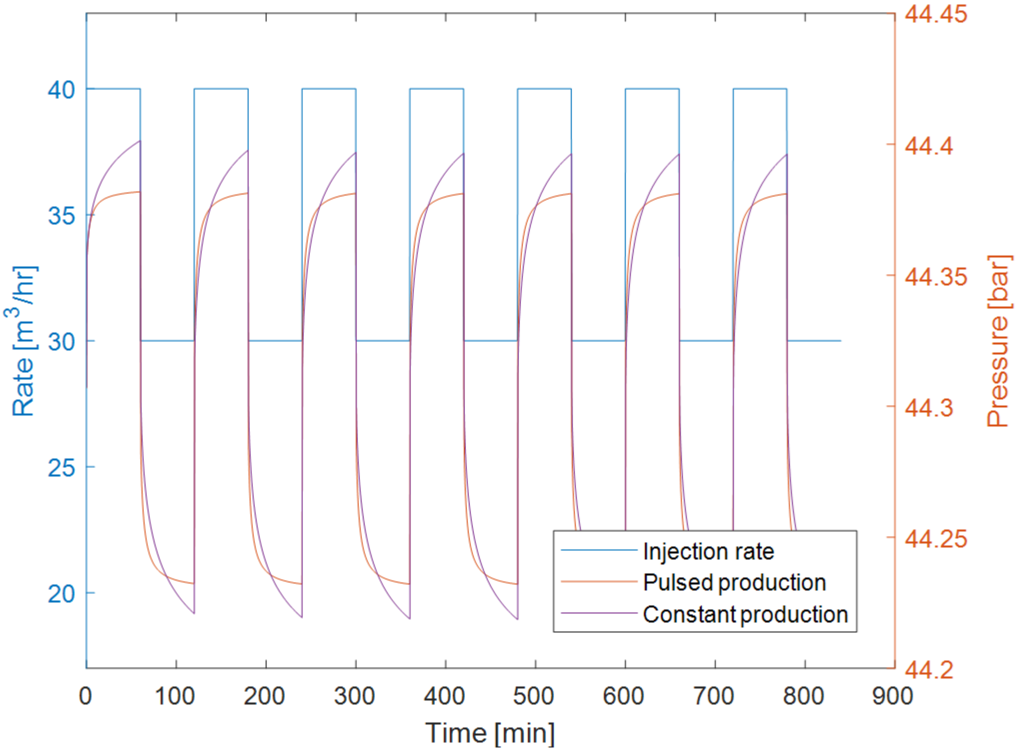

Figure D4 – Pressure response to pulsed injection in the hot well. Comparison of the response when the producer is also pulsed and when it is on a constant rate.

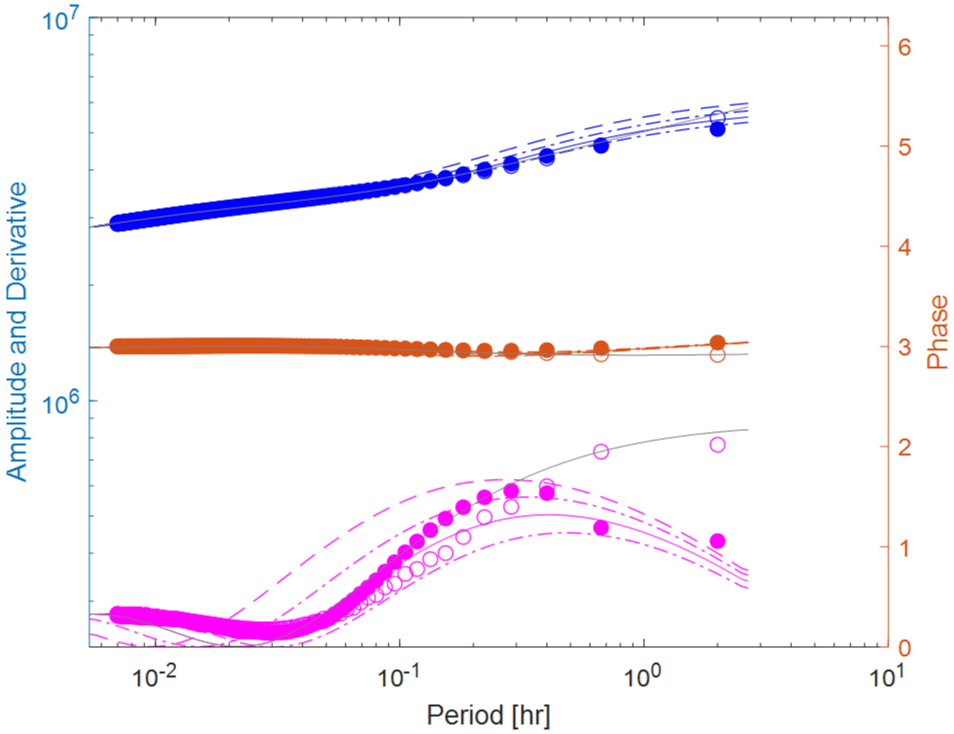

Figure D5 – Response and derivative of the synthetic test for interference. Blue: Response amplitude. Magenta: Response derivative amplitude. Brown: Response phase. Open symbols: from the analysis of the Eclipse pressure outputs with constant production rate. Filled symbols: from the analysis of the Eclipse pressure outputs with pulsed production rate. Gray lines: theory with pulses in injector only. Colored lines: theory with pulses both in injector and producer. Lines from top to bottom: with thermal radius at 40, 50, 60 (solid lines) and 70 m.

D2.2.4 Frequency analysis

For the frequency analysis of the field trials, we first performed a Fourier analysis on the rate and pressure data and selected the peaks associated with the imposed pulses. For clarity, we plot the responses of tubing P3 only. The other pressure traces give comparable results. Figure D6 and Figure D7 give the rate and pressure spectra of the baseline tests, Figure D8 and Figure D9 give the spectra of the test after 5 days and the post-loading test. We see that the test with 20 minutes pulses only gives few peaks and therefore is less well interpretable. The tests with 2 hours and 4 hours pulses give many more data points. In the following we will therefore include the baseline 20-minute pulse test results as support for the analysis of the 2-hr baseline test. The post-loading test, with the uneven division of the 4-h pulse in 93 and 147 minutes, indeed results in more frequency peaks. Especially the peaks with even multiples of the base frequencies could be valuable.

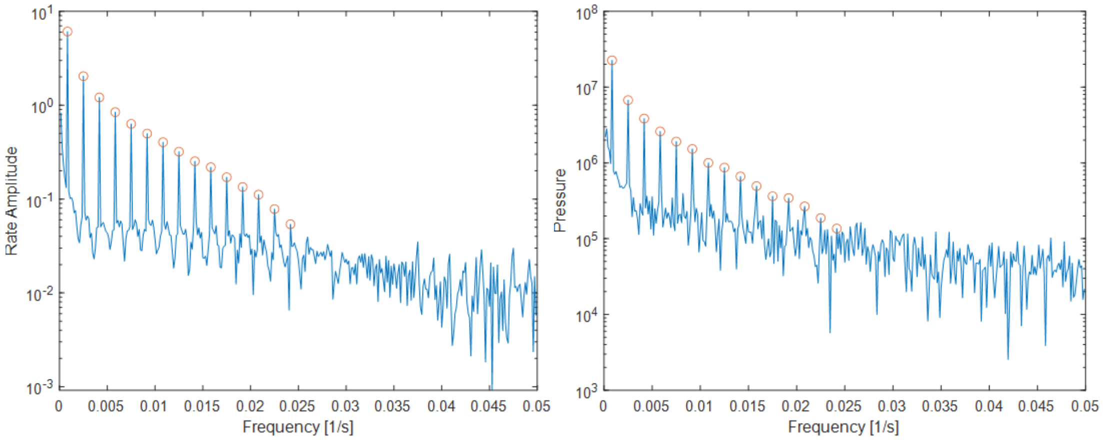

Figure D6 - Rate and pressure spectrum for the 20-minute-pulse baseline test.

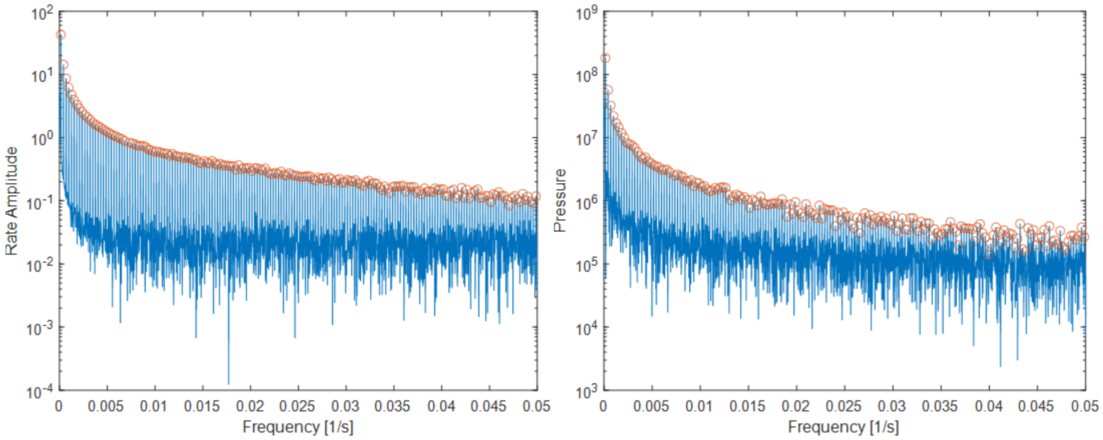

Figure D7 -- Rate and pressure spectrum for the 2-hour-pulse baseline test. Blue lines: full FFT spectrum. Symbols: Selected peak frequencies.

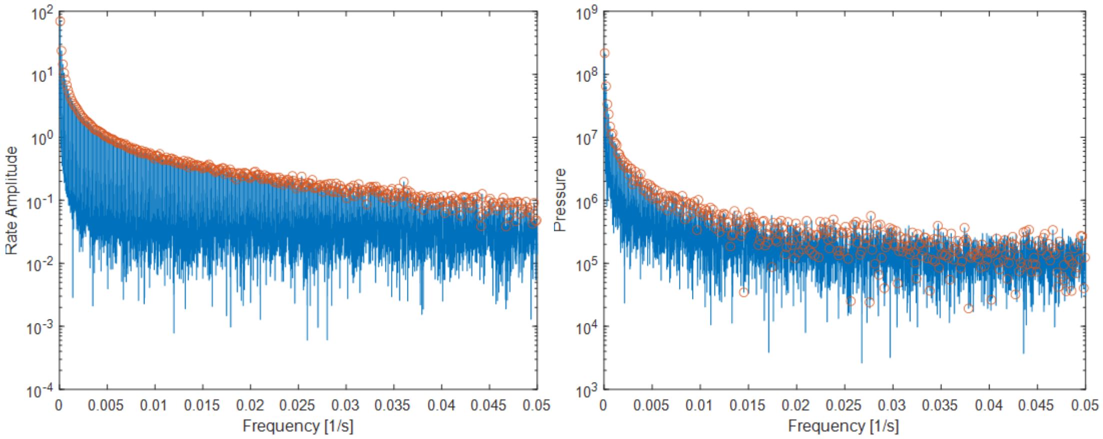

Figure D8 – Rate and pressure spectrum for the 4-hour-pulse test after 5 days of loading.

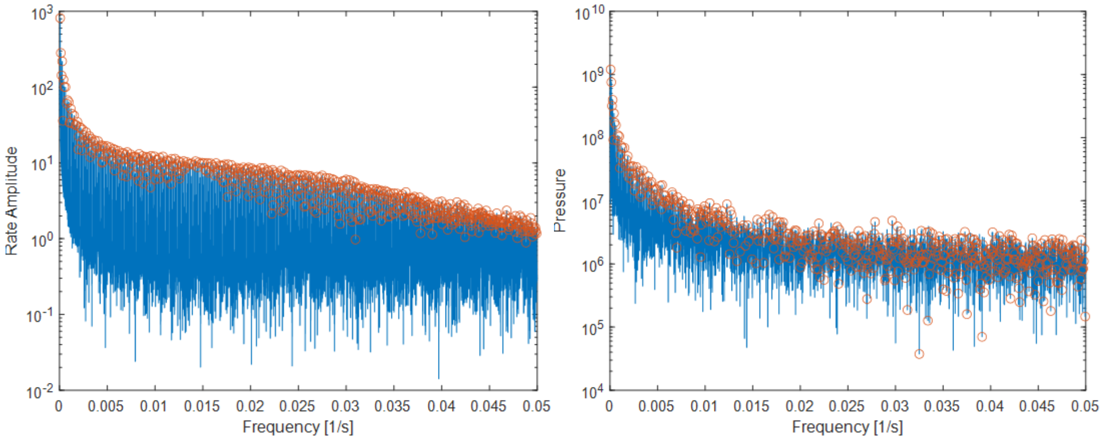

Figure D9 – Rate and pressure spectrum for the 4-hour-pulse post-lading test.

The responses are calculated by dividing the pressure signal in the selected peaks by the corresponding rate signal. This gives an amplitude and a phase for every selected frequency. In addition, we calculate the derivative of the signal. The calculation of the derivative employs a smoothing factor of 1. The responses are plotted in Figure D10, Figure D11 and Figure D12.

A fit to the data was attempted by adjusting the unknown parameters in the theoretical response functions. First, the baseline was handled. Known data are the wellbore radius (0.2 m); the injection layer height (20 m); viscosity of the water at injection temperature (0.35 cP) and at reservoir temperature (1.13 cP); total compressibility ($\sim 10^{-9}$ Pa^{-1}), and virtually negligible wellbore storage ($2*10^{-8}$ m^3/Pa). For the baseline, we fitted the data with a single-zone infinitely acting radial flow model, as heating of the reservoir has not yet started (or, equivalently, with a 2-zone model with the cooled radius equalling the wellbore radius). A reasonable fit could be obtained with a permeability of 15000 mD ($15*10^{-12}$ m^2).

With the value of 15000 mD, fits were attempted of the responses after 5 days of loading and at the end of loading. The fit after 5 days was reasonable with a thermal radius of 10 m (Figure D11).

The interpretation of the post-loading test was more complicated. In fact, the second peak (the second from the right in the right plot of Figure D12) appears to be larger than the base period (the first peak far right). This complicates the use of a derivative: it is always positive in our model but negative in these data[4].

For the small frequencies/large periods, however, the most important issue is the interference with the production well. We have demonstrated in the previous that amplitudes and derivatives for periods larger than 25 minutes must be corrected for the influence of the pulses in the producer.

Still, we do observe a transition to larger derivative values when increasing the period to values larger than 0.7 hr. Figure D12 also shows theoretical responses calculated without and with the interference term introduced in the previous section. Reasonable curves could only be obtained by lowering the permeability to 4000 mD while simultaneously decreasing the response amplitude by applying a considerable negative skin (S = -4). The introduction of the interference term produced a qualitatively right decrease of the derivative for larger periods. Still, a thermal front can not be unequivocally determined.

We conclude that the analysis is not straightforward and the model cannot be faithfully used in the analysis. The largest distortion stems from the interference with the pulses applied in the producer well (the cold well), but there may also be effects of the dispersed thermal front, the thermal instabilities and the associated hydraulic head variations, or reservoir effects due to the injection of large amounts of fluid during the loading period.

A problem with all the test is formed by the small response amplitudes for the larger frequencies and the associated larger derivatives. For the post-loading test, the effect of the relatively smooth fluctuations in temperature and hydraulic head are not expected to play a role at these frequencies. For frequencies below 0.014 s^{-1} (periods larger than 0.02 hr) the signal is larger than the noise. The trend of the data between frequencies of 0.003 and 0.014 s^{-1} (periods between 0.02 and 0.1 hr) is not represented by the curves obtained with the model. The smaller-than-expected amplitudes may be related to the flow pattern in the reservoir. As was observed in the parallel study with temperature sensing through optical fibres, the temperature front does not advance with the same speed across the full reservoir height. High-temperature streaks take up the largest part of the fluid and hence the thermal penetration there is larger than in the lower-permeability parts. An analysis of the pulse tests in such circumstances requires either a numerical approach or an extension of the current single-layer radial composite model to more layers. Another possible explanation is in the physical behaviour of the pumps. A difference between pulse testing and conventional well testing is that the pulse tests are performed while pumping continues. If there is a mismatch between the imposed rate and the actual rate this might result in a dampening of the signal in the same way as a large wellbore storage would do.

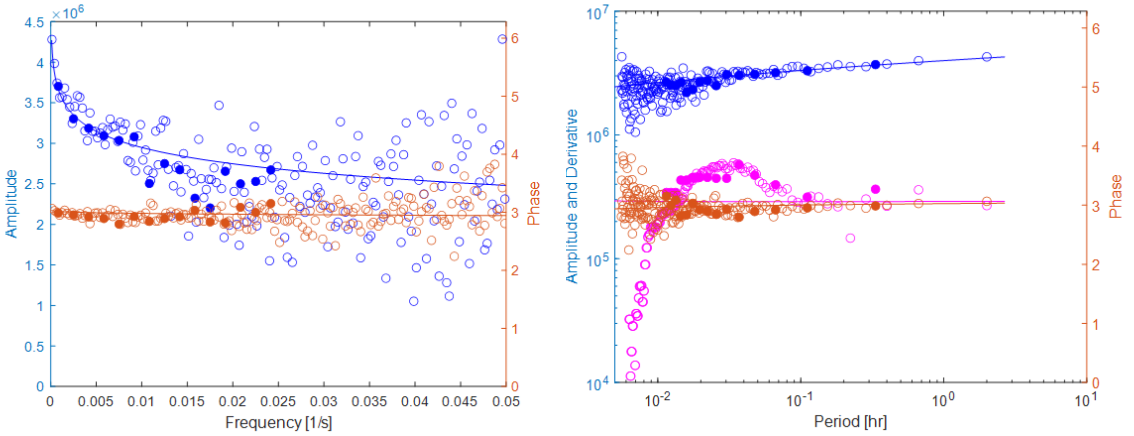

Figure D10 – Response of the baseline tests. Closed symbols: 20-minute pulses. Open symbols: 2-hour pulses. Lines; Response function. Left: Amplitude and phase vs frequency. Right: Amplitude, Derivative of Amplitude and phase vs period.

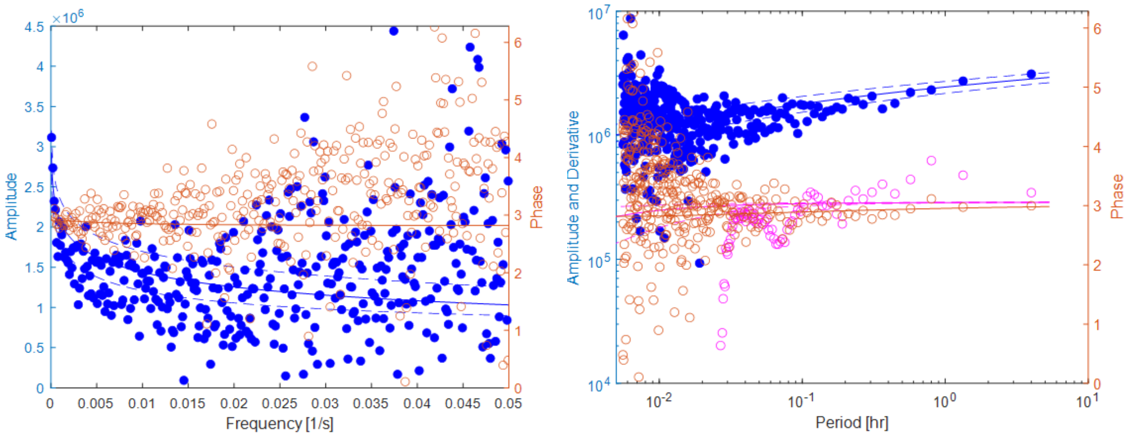

Figure D11 – Response of the test after 5 days. Curves: model with 2 temperature zones. Thermal radius for curves (top to bottom) 5 m, 10 m (solid curves), and 20 m.

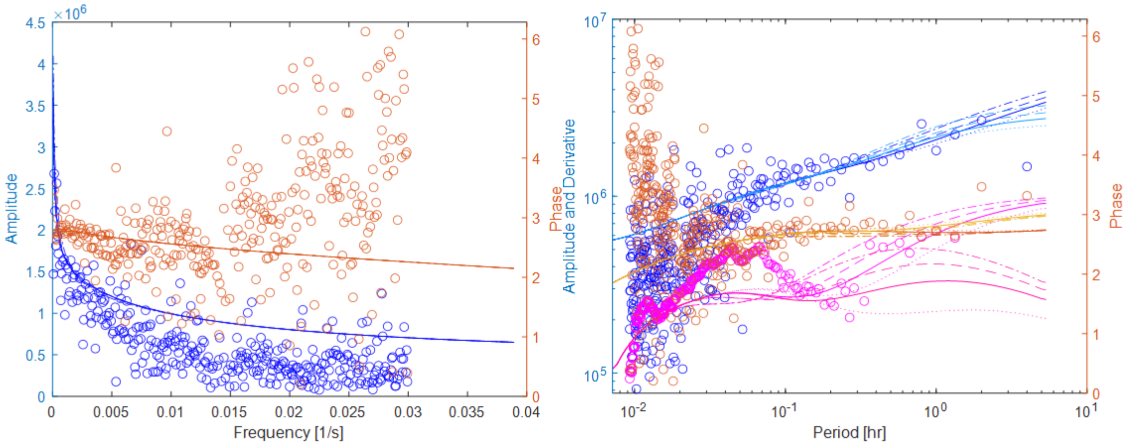

Figure D12 – Response of the post-loading test. Curves: model with 2 temperature zone. Top to bottom(thermal radius at 80 m, 100 m, 120 m (solid curve), 150 m. Right picture: amplitude and derivative curves dipping down, and phase curves dipping up result from adding the response from the pulsed production.

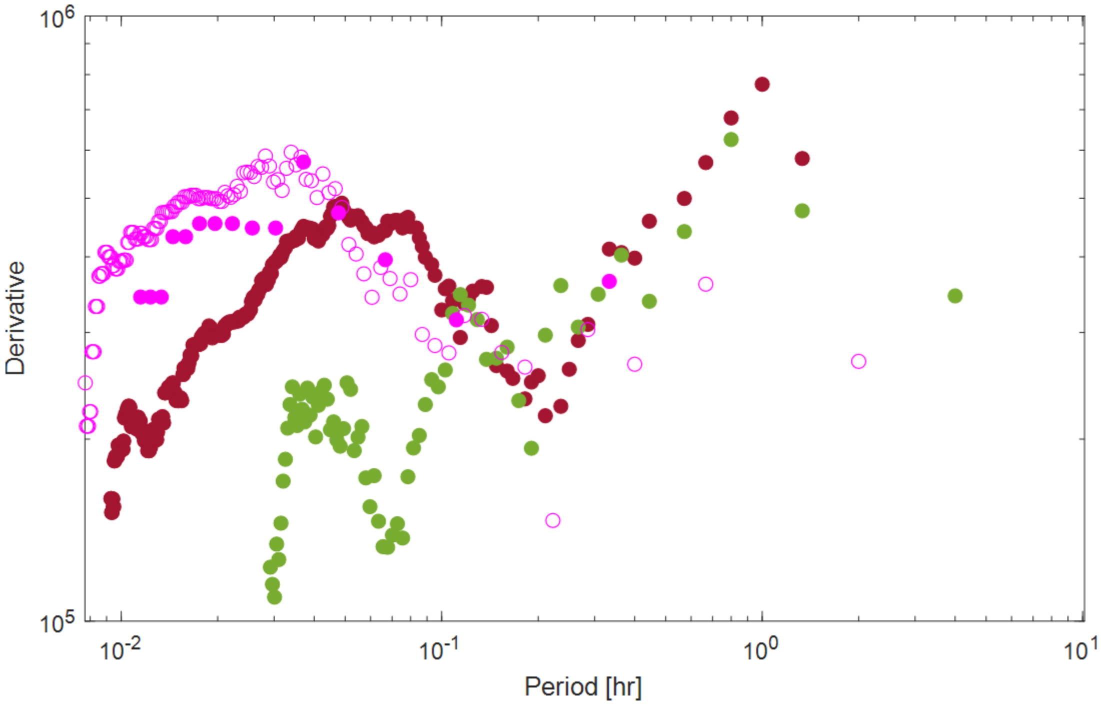

Figure D13 – Comparison of measured derivatives. Magenta: Baseline. Green: After 5 days of loading. Brown: Post-loading.

The background of the anomalous frequency responses for small frequencies is, besides the interference, related to the temperature fluctuations and the suboptimal corrections for the hydraulic head. However, temperature fluctuations are not by definition a loss of quality: in a separate study into the effects of temperature variations of the injected fluid [Fokker and Van Wees, 2022] we demonstrated how the pressure is affected by temperature fluctuations and how this response can be used to obtain knowledge about the near-well area. The key thought behind this is that the injected fluid is quickly in thermal equilibrium with the surrounding reservoir rock; temporal temperature fluctuations of the injection fluid thus cause a spatial temperature profile propagating into the reservoir. On its turn this causes fluctuations in the injectivity, with the main effect coming from the area in the near vicinity of the well. We thus applied the temperatures as determined at the bottom of the well, the other parameters, like those obtained for the baseline and the test after 5 days, and the temperature dependence of the viscosity to estimate the size of the effect for the current test. However, we found that the effect would be much smaller than the anomalous pressure behaviour that we observed. This is in line with the observation above that the hydraulic head corrections have not been correctly estimated.

D2.3 Concluding remarks on the demonstration case

The thermal front calculation after 5 days of injection yielded a value of about 10 m. This is in line with the expected value based on the amount of fluid injected and the height of the injection zone.

The thermal front after loading could not be estimated well, because the analysis was complicated by a number of issues. The most important one is the interference with the response of the producer well, which was pulsed in the same way as the injector well. Further, there was the disturbance of the pressure response by the variable hydraulic head because of the variable temperature. Then, there was the behavior of high-frequency responses. These responses were smaller than expected. This may be related to heterogeneity of the permeability and the related, distribution of the thermal front. In addition the outline of the thermal front is affected by gravitational upwelling of high temperature brine. In fact, a preliminary history match on the DTS temperature data confirms a more intricate picture: the temperature front could not be approximated by a single value and indicates that both permeability stratification and thermal upwelling affect the heat front (Dinkelman et al., 2022). An extension of the theory analysis in which the theory would allow for such complications was beyond the scope of the present study.

D3 Evaluation of pulse testing as monitoring technique

The pulse tests described here show that it is possible to deploy them to obtain knowledge about the reservoir properties, including the position of the thermal front. There are, however, some conditions that need to be improved in comparison with the current tests, and some uncertainties may remain.

In the first place, when pulse tests in a doublet are not performed independently, i.e. when production and injection in the two wells are coupled and pulsed in the same way, interference will show up. The pulse period at which this happens depends on the distance between the wells and the reservoir properties. In the tests described here, interference was clear and needed to accounted for. We created a basic method to account for the interference; this should be further validated and developed. Simultaneous evaluation of the signal in the producer well could possibly be helpful in such analyses.

We further note that bottomhole pressures are instrumental in collecting high-quality data. Bottomhole pressures are not influenced by friction and by fluctuations in hydraulic head. The latter were present in our last test due to the varying injection water temperature and the associated density variations. A reliable calculation of the hydraulic head would involve more than what we have been able to do here: in particular the temperature development of the stagnant measurement tubing could not be faithfully determined.

Temperature variations, however, can bear additional information: they inflict pressure fluctuations at the point of injection because the temperature in the reservoir also fluctuates and through the water viscosity causes fluctuations of the viscous pressure drop in the reservoir. Still, for an unambiguous analysis it is beneficial to not change injection rate and temperature simultaneously. We advocate pulses of either temperature or injection rate.

The interpretation of pulse tests relies on the calculation of a pressure derivative vs harmonic period. This is easier to obtain when many frequencies can be used. It is therefore important to have fast switching procedures of the injection rate – fast switching results in many more observable high-frequency signals. For the longer times, it is beneficial to complement a pulse test with a traditional well test with pressure transient analysis during shut-in.

The heat front around the injector cannot be expected to be radially symmetric and independent of depth, especially further away from the injection well. This is due to gravitational upwelling of the hot brine as well as permeability subject to more or less heterogeneity. Furthermore it cannot be excluded that viscous fingering can occur as a consequence of the low viscosity ratio of injected and reservoir brine. Finally, the production from the other well will cause preferential flow in that direction.

It is important to build more confidence in pulse testing technology by applying it to storage operations. The technique has potential of a powerful monitoring technique but needs to be designed with care and operated with dedicated monitoring equipment. Interference with the producer well requires a dedicated theoretical treatment.

Adres
Princetonlaan 6
3584 CB Utrecht

Postadres
Postbus 80015
3508 TA Utrecht

Telefoon
088 866 42 56

E-mail
contact@warmingup.info

Website
www.warmingup.info